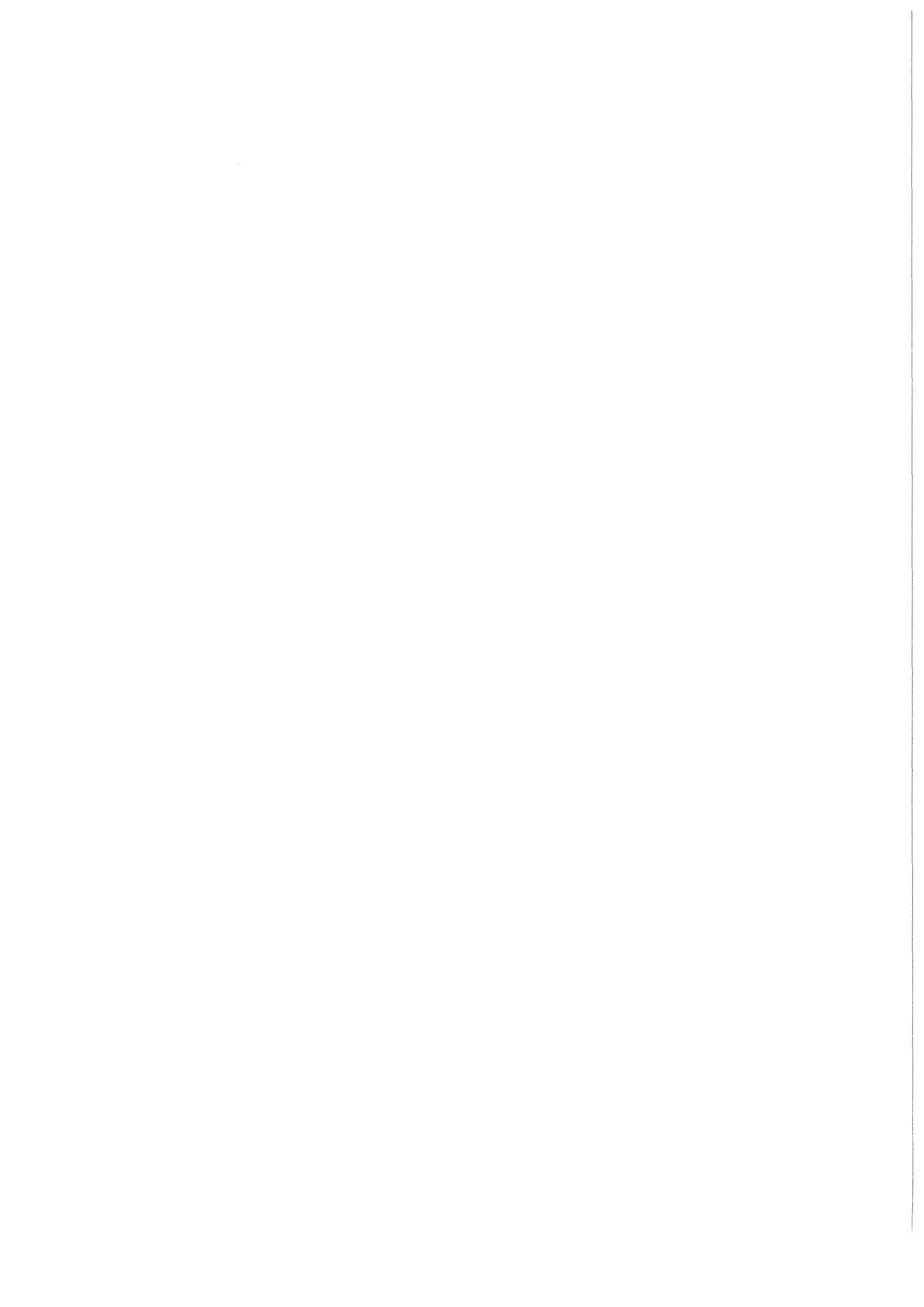# Influence of Point Defects on the Lattice Site Occupation of Soluble and Non Soluble Atoms in Vanadium

A. Azzam

Institut für Nukleare Festkörperphysik

KERNFORSCHUNGSZENTRUM KARLSRUHE

Institut für Nukleare Festkörperphysik

KfK 4066

INFLUENCE OF POINT DEFECTS ON THE LATTICE SITE OCCUPATION OF SOLUBLE AND NON SOLUBLE ATOMS IN VANADIUM*

A. Azzam

Kernforschungszentrum Karlsruhe GmbH, Karlsruhe

ABSTRACT

Lattice location studies for implanted impurities in vanadium single crystals are performed using the Rutherford backscattering and channeling techniques. The implanted species are selected to be soluble, nearly soluble and non-soluble in vanadium in the thermal equilibrium. The implanted impurity concentrations are in the range between 0.1 and 0.2 at.% where impurity interactions can be negleted.

In order to study the influence of collisional effects on the lattice site occupation of the implanted impurity, the implantation and in situ-analysis are carried out at 5 K. The influence of mobile point defects is studied by correlating the lattice temperature during the implantation and in situ-measurements (5, 77 and 300 K) to the annealing stages of the point defects. Postirradiation and annealing experiments are also performed to study the influence of mobile point defects at different annealing stages.

The substitutional fraction measured for soluble and nearly soluble elements (Cu, As, Se, Sn, Te, I, Au, Pb and Bi) at 300 K is equal to 1.0. For the nearly soluble element Bi a substitutional fraction equal to 1.0 independent of the lattice temperature between 5 and 300 K is obtained although the calculated replacement collision probability is 0.3. The non-soluble elements (Xe, Ce, La, Ba and Cs) have only a small or zero substitutional component after implantation at 300 K while they reveal a high substitutional fraction after implantation at 5 or 77 K.

It is concluded that empirical criteria based on thermal equilibrium cannot predict the substitutionality results for ion implantation in metals especially at low temperatures where the point defects are not mobile. The replacement collisions obviously are not the main mechanism leading to lattice site occupation for the implanted ions. The main mechanism is the spontaneous recombination of the impurity with a lattice vacancy within the

cascade regime. Non-solube oversized elements have a certain probabi-
lity to trap further vacancies in the cascade as well as in
the delayed regime, and form impurity-vacancy complexes. The bindina
energy of these complexes is related to the heat of solu-
tion of the system. Postirradiation and annealing experiments sup-
port the proposed mechanisms.

Plastic deformation and polygonization of the implanted
region as well as coherent or incoherent precipitation of the
impurities are observed at high impurity concentrations.

Einfluß der Punktdefekte auf die Gitterplatzbesetzung der in Vanadium löslichen und nicht-löslichen Fremdatome

Zusammenfassung

In dieser Arbeit wurde die Gitterplatzbesetzung von verschiedenen in Vanadium implantierten Elementen (Cu , As , Se, Kr, Sn, Te, I, Xe, Cs, Ba, La, Ce, Au, Pb und Bi) mit Hilfe der Rutherford-Ruckstreuung und der Channelling-Methode untersucht.Die ausgewählten Fremdatome sind in Vanadium im thermischen Gleichgewicht löslich (Cu, Sn und Au) oder nicht löslich (Se, Kr, Te, I, Xe, Cs, Ba, La, Ce, Pb, und Bi). Die Konzentration der Fremdatome lag im Bereich zwischen 0.1 und 0.2 at.%, so daß eine Wechselwirkung untereinander vernachlässigt werden kann.

Um den Einfluß der stoßkinetischen Prozesse auf die Gitterplatzbesetzung zu untersuchen, sind die Implantationen und nachfolgenden Messungen in situ bei 5 K durchgeführt worden. Der Einfluß beweglicher Punktdefekte auf die Gitterplatzbesetzung wurde durch eine geeignete Wahl der Implantations- und der Probentemperatur während der Messungen (5,77, 300 K) studiert. Die Rolle zusätzlicher Punktdefekte und deren Beweglichkeit wurde in Nachbestrahlung und Anlaßexperimenten unter Berücksichtigung der verschiedenen Ausheilstufen im Vanadium untersucht.

Die substitutionelle Komponente der im thermischen Gleichgewicht löslichen oder fast löslichen Fremdatome (Cu, As, Se, Sn, Te, I, Au, Pb und Bi) ist bei 300 K gleich 1.0. Für Bi ist die substitutionelle Komponente gleich 1.0, unabhängig von der Implantations- und Meßtemperatur zwischen 5 K und 300 K, obwohl die nach der Ersetzungs-Stoßtheorie bestehende Wahrscheinlichkeit für die Gitterplatzbesetzungen 0.30 ist. Die nichtlöslichen Elemente (Xe, Ce, La, Ba und Cs) haben bei 300 K nur eine geringe substitutionelle Komponente. Bei 5 K und 77 K dagegen ist diese Komponente höher und beträgt etwa 0.5 bis 0.70.

Die experimentellen Ergebnisse zeigen, daß die üblichen Gleichgewichtsregeln für die Löslichkeit von Fremdatomen die substitutionelle Komponente in implantierten Systemen, insbesondere bei Implantationen bei tiefen Temperaturen, bei denen Punktdefekte nicht beweglich sind, nicht voraussagen können. Auch die Ersetzungsstoßtheorie allein kann die gefundenen Gitterplatzbesetzungen nicht erklären. Es wird angenommen, daß die spontane Rekombination der Fremdatome mit Gitterleerstellen innerhalb der Kaskade der Hauptmechanismus ist, der die Gitterplatzbesetzung bestimmt. Die nichtlöslichen übergroßen Atome haben eine hohe Wahrscheinlichkeit, während der Abkühlzeit der Kaskade und danach mehrere Leerstellen einzufangen und Fremdatom-Leerstellen-Assoziate zu bilden. Die Bindungsenergie solcher Assoziate ist mit der Lösungswärme verknüpft. Die Ergebnisse von Nachbestrahlungs- und Temperexperimenten bestätigen den vorgeschlagenen Mechanismus.

Eine plastische Verformung bzw. Polygonisierung der implantierten Bereiche und kohärente oder nicht kohärente Ausscheidungen sind bei hohen implantierten Dosen(3 at.% bis 20 at.%) beobachtet worden.

LIST OF CONTENTS   Page

1. INTRODUCTION

Ion implanation is a well established technique for the introduction of impurities into the near surface region of materials. It is currently used to inject dopants for the manifacture of simiconductor devices and is finding application in the area of metals and alloys as well /1/. One major advantage of this technique is its ability to provide an alloy between constituents without regard to their chemical or metallurgical compatibility. Thus obstacles to thermal diffusion for alloying in the melt such as solubility limits or chemical reactivity can be avoided. For this reason, alloys created by ion implantation will be mestatable, in general, and little guidance can be expected from the equilibrium binary phase diagram with regard to the physical state of such a system. It is already known that at relatively high impurity concentrations one might obtain metastable or intermetallic, amorphous or disordered structures or intermetallic compounds for example /2/.

From a fundamental viewpoint and, to the extent that concentrated alloy properties are related to those of the dilute case, also from a practical viewpoint, it could be desirable to develop an understanding of the factors which determine the isolated impurity-host configuration achieved by ion implantation. Basic processes may be of collisional nature due to cascade effects or may be caused by thermodynamical or mechanical driving forces due to local fluctuations in the chemical potential of the foreign atoms in the host. Further the interaction of point defects especially with vacancies is a very important process as lattice vacancies are always potential minima for the implanted atoms. Many attempts were made to construct some criteria for predicting the most important parameters which determine the lattice position of the impurity atoms.

Darken and Gurry /3/ constructed a map containing the atomic radius and the electronegativity introduced by Pauling /4/, to describe the Hume Rothery rules /5/ for the solid solubility of equilibrium alloys. An ellipse which is centered on the solvent and has one axis of ± 15% of the solvent's atomic radius and another axis of ± 0.4 of the electronegativity unit would encompass most of the solutes which show significant solubility in the solvent. Selective use /6/ of the Hume R thery method for the cases where the crystal structure of the solute and solvent are similar slightly improved the reliability of the Darken Gurry predictions.

Sood et.al. /7/ compared the substitutionality results of 63 implanted metastable systems with the Hume Rothery rules /5/. They found that a relaxation of the criterion gives a good separation between the substitutional and the non substitutional elements in a metal host. The relaxed criterion are: The atomic size difference between the impurity and host must be in the range between -15% and + 40% of the host atomic size. The electronegativity difference must be less than 0.7.

The fundamental parameters in a successful semiemperical theory of the heat of alloy formation developed by Miedema and coworkers /8-10/ are also used /11-13/ to propose an empirical rule for the substitutionality of metastable alloys produced by ion implantation. Good separation has been achieved between the substitutional and the non substitutional elements, for example for Be as a host /13/.

In pure collisional considerations, the implanted atom has a certain probability to replace an lattice atom during the slowing down process. Brice /14/ solved numerically the integral equation constructed by Dederichs et.al. /15/, using the Thomas-Fermi elastic scattering cross

section to caluclate the replacement collision proba-
bility. This probability should in principle be iden-
tical with the substitutional fraction as measured by
the channeling technique., if the substrate tempera-
ture is low enough, so that no diffusion of point de-
fects takes place.

In this work lattice location studies are perfor-
med, using vanadium single crystals as a host. The im-
planted elements are selected to be soluble and non
soluble in the thermal equilibrium. The implantations
and in situ measurements are carried out at 5 K where
neither the interstitials nor the vacancies are mobile,
at 77 K where only the interstitials are mobile and at
300 K where both the interstitial and the vacancies are
mobile /16-19/. Postirradiation and annealig experiments
are carried out for some systems to study the interaction
between the impurities and the point defects. Comparison
of the results with the suggested models have been per-
formed in order to give an answer to the question concerning
the parameters which determine the substitutionality of the
implanted systems.

2. THEORETICAL BACKGROUND

2.1 Rutherford Backscattering Spectrometry

If a beam of accelerated charged particles (in the energy range between 200 and 3000 KeV) impinges on a thin target, almost all of the incident particles penetrate the target with some slightly reduced energy and only slightly altered direction. The few incident particles that are lost undergo large changes in energy and direction. This changes are due to close encounters of the incident particles with the nucleus of a single target atom. If the target is thick, only the particles scattered backward by angles of more than 90 degrees from the incident direction can be detected. These particles are called elastic backscattered particles.

2.1.1 Kinematic Factor and Scattering Cross Section

Incident particles (projectiles) with atomic mass M_1 and energy E_0 are backscattered with energy E_1 from the target atoms of mass M_2 in a certain direction making an angle Θ with the incident direction. The ratio of the projectile energy after the elastic collision to that before is called the kinematic factor K defined by

$$K = E_1 / E_0 \tag{1}$$

which can be calculated in the laboratory system as follows:

$$K = \left\{ \frac{(M_2^2 - M_1^2 \sin^2\Theta)^{1/2} + M_1\cos\Theta}{M_2 + M_1} \right\}^2 \tag{2}$$

The kinematic factor depends only on the mass ratio of the projectile to target atom (M_1/M_2) and on the scattering angle.

Equations (1) and (2) contain the essence of how backscattering spectrometry acquires its ability to determine the mass of an atom. If the energy E is measured at a known angle, the mass M_2 of the target can be determined from eq. (2).

It is noticed that the mass resolution is inherently better for light target atoms than for heavy ones. The mass resolution can be improved by increasing the projectile mass and making the scattering angle as large as possible.

The differential scattering cross-section, well known as Rutherford scattering cross-section, in a given direction is given by /20/

$$\frac{d\sigma}{d\Omega} = \left(\frac{Z_1 Z_2 e^2}{2E \sin^2\theta}\right)^2 \frac{\left\{[1-(\frac{M_1}{M_2}\sin\theta)^2]^{1/2} + \cos\theta\right\}^2}{\{1-[\frac{M_1}{M_2}\sin\theta]^2\}^{1/2}} \tag{3}$$

where

$(\frac{d\sigma}{d\Omega})$ is the differential scattering cross section

Z_1 and Z_2 are the atomic numbers of the projectile and target atoms, respectively.

e is the electronic charge.

From eq. (3) it is clear that

i. $(\frac{d\sigma}{d\Omega})$ is porportional to Z_1^2, indicating that the backscattering yield obtained from a given atom is greater for heavier projectile

ii. $(\frac{d\sigma}{d\Omega})$ is porportional to z_2^2, indicating that heavy
atoms are very much more efficient scatterers
for any given projectile than light ones

iii. $(d\sigma/d\Omega)$ is approximateley inversely porportional
to the fourth power of sin $(\theta/2)$ if $M_1 << M_2$,
i.e., the scattering yield increases rapidly as
the scattering angle decreases.

iv. $(\frac{d\sigma}{d\Omega})$ is proportional to E^{-2}, i.e. the scattering
yield rises rapidly with decreasing the bombarding
energy.

2.1.2 Energy Loss and Stopping Cross Section

An energetic particle that impinges on a target
will penetrate into it. This is so because the Ruther-
ford backscattering collision is highly unlikely. As
the particle slows down its kinetic energy decreases.
The slowing down process of the energetic particles is
a result of its elastic and inelastic interaction (see
chapter 2.3.1.1 and 2,3,1,2). The energy loss due to the
elastic interaction is small for high energetic low mass
particles in the MeV region /21/. The amount of energy loss
(dE) per traversed distance (dX) depends on the density and
composition of the target as well as the atomic mass and
the energy of the projectile. If a beam of monoenergetic
ions with energy (E_o) impinges on a given target Fig. (1),
then a fraction of the incident ions will be backscattered
from the surface and detected with energy $(K.E_o)$. Most of
the ions will penetrate the target and some of them
will be backscattered at distance X from the target
surface.
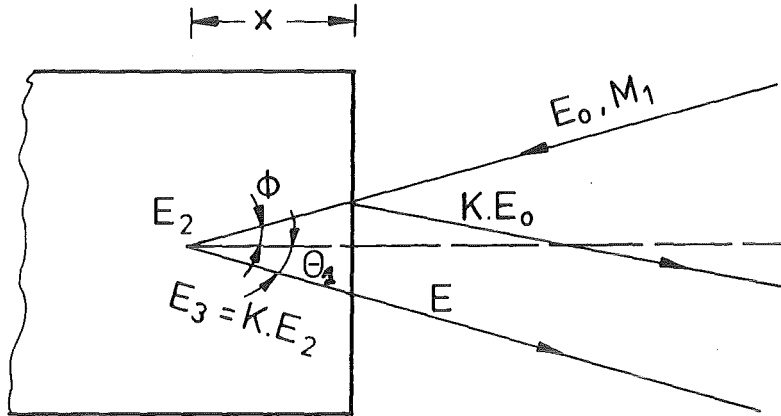
Fig. 1 Schematic drawing for backscattering of ions
        with energy E_0 and atomic mass M_1 from a
        target of atomic mass M_2

The energies of these ions just before, and
after backscattering at X are E_2 and E_3, respectively.
The measured energy of the ions leaving the target
will be E. As an approximation the dependence of the
energy loss on the projectile energy in the near sur-
face region can be negleted. Then

$$E_2 = E_0 - \frac{X}{\cos\phi} \left.\frac{dE}{dX}\right|_{E_0}$$

$$E_3 = KE_2 = K(E_0 - \frac{X}{\cos\phi} \left.\frac{dE}{dX}\right|_{E_0}) \qquad (4)$$

$$E = E_3 - \frac{X}{\cos\Theta_1} \left.\frac{dE}{dX}\right|_{E_3}$$

·If the value of the energy loss $(\frac{dE}{dX})_{E_3}$ will be repla-
ced by $(\frac{dE}{dX})_{KE_0}$, then equation (4) can be written as

$$E = K(E_0 - \frac{X}{\cos\phi} \left.\frac{dE}{dX}\right|_{E_0}) - \frac{X}{\cos\Theta_1} \left.\frac{dE}{dX}\right|_{K \cdot E_0}$$

i.e.

$$KE_O - E = \Delta E = [\frac{K}{\cos \phi} \frac{dE}{dX}\Big|_{E_O} + \frac{1}{\cos\Theta_1} \frac{dE}{dX}\Big|_{K \cdot E_O}] \cdot X \qquad (5)$$

The value between the brackets in equation (5) is defined as the backscattering energy loss parameter [S]. Then equation (5) can be written as

$$\Delta E = [S] \cdot X \qquad (6)$$

For normal incidence, the angle ϕ will be 0, $\Theta_1 = 180^O - \Theta$ and the backscattering energy loss parameter [S] can be written as

$$[S] = K\frac{dE}{dX}\Big|_{E_O} + \frac{1}{|\cos\Theta|} \frac{dE}{dX}\Big|_{KE_O} \qquad (7)$$

The value of [S] can be calculated using the values of the stopping cross section per atom (ϵ), tabulated by Ziegler and Chu /21/, and defined by

$$\epsilon = \frac{1}{N} (\frac{dE}{dX}) \qquad (8)$$

where N is the atomic density of the respective monoatomic target. Using eq. (6) one can transform the energy scale in the backscattering energy spectrum to a depth scale. The depth scale can be used, for example, to calculate the thickness of thin films or to determine the diffussion and damge profiles in a single crystal.

In the case of a compound target, for example, composed of A and B atoms, the backscattering energy loss parameter for the scattering from the element A or B in the compound will be defined as $[S_A^{AB}]$ or $[S_B^{AB}]$, respectively by

$$[S_A^{AB}] = K_A \frac{dE}{dX}\bigg|_{E_O} + \frac{1}{|\cos\Theta|} \frac{dE}{dX}\bigg|_{K_A \cdot E_O}$$

$$[S_B^{AB}] = K_B \frac{dE}{dX}\bigg|_{E_O} + \frac{1}{|\cos\Theta|} \frac{dE}{dX}\bigg|_{K_B \cdot E_O}$$

For caluclating the backscattering energy loss para - meter, the linear additive Bragg's rule can be used, i.e.

$$\varepsilon^{AB} = N_A \varepsilon^A + N_B \varepsilon^B$$

where N_A and N_B are the atomic concentration of the ele- ments A and B in the compound, respectively.

2.1.3 Backscattering Yield

The spectrum height (H) in a backscattering spectrum that is the number of counts in a channel evaluated at the surface for normal incidence, can be written as

$$H = \sigma(E_O) \cdot \Omega \cdot Q \cdot N \cdot \delta X \qquad (9)$$

where $\sigma(E_O)$ is the average scattering cross section at energy E_O.

Ω = is the solid angle of the detector

Q = is the number of the incident particles

N = is the atomic density of the target

δX is the depth corresponding to one channel in the spectrum

Inserting Eq. (6) in Eq. (9) one gets

$$H = \sigma(E_O) \cdot \Omega \cdot Q \cdot N \cdot \frac{\delta E}{[S]} \qquad (10)$$

where δE is the energy width per channel. δE is determined experimentally, for example, using the backscattering spectrum from a calibration target consisting of very thin Al and Au films evaporated on a carbon substrate. For thin targets the peak height (H) does not change strongly with the depth. The total number of counts in the peak area (A) is then given by

$$A = H \cdot (\frac{\Delta E}{\delta E})$$

using equ. (6) and (10) one gets

$$A = \sigma(E_O) \cdot \Omega \cdot N \cdot X \qquad (11)$$

where X is the target thickness.

2.1.4 Quantitative Analysis

2.1.4.a Compound Thin Film

For a given compound thin film, with two different mass components A and B, the backscattering yield from each component is given by

$$H_A = \sigma_A \cdot \Omega \cdot Q \cdot N_A \cdot \frac{\delta E}{[S^{AB}_A]}$$

$$H_B = \sigma_B \cdot \Omega \cdot Q \cdot N_B \cdot \frac{\delta E}{[S^{AB}_B]}$$

The concentration ratio then is given by

$$\frac{N_A}{N_B} = \frac{H_A}{H_B} \cdot \frac{[S_A^{AB}]}{[S_B^{AB}]} \frac{\sigma_B}{\sigma_A} \qquad (12)$$

The ratio $[S_A^{AB}/S_B^{AB}]$ can be taken as unity, especially for not too different masses, in a zeroth-order approximation. This ratio actually approaches unity within 10% in most cases for the He ion energies of 1 to 2 MeV /20/. For small impurity concentrations of element A in a given target B, the target can be considered as a pure target and one has to calculate $[S_A^B]$ and $[S_B^B]$ instead of $[S_A^{AB}]$ and $[S_B^{AB}]$, respectively.

2.1.4.b Surface Impurity

For a heavy impurity of mass M_i on a light substrate of mass M, the total area A_i of the impurity signal is given by eq. (11). The number of the impurity atoms per unit area can be given by

$$(N \cdot X)_i = A_i/(\Omega \cdot Q \cdot \sigma_i)$$

where the subscript i stands for impurity. Substituting the value of $(\Omega \cdot Q)$ from eq. (10) one gets

$$(N \cdot X)_i = \frac{A_i}{A_M} \frac{\sigma_M}{\sigma_i} \cdot H_M \cdot \frac{\delta E}{[S_M^M]} \qquad (13)$$

where H_M is the height of the signals due to scattering from the surface of the substrate.

Eqs. (12) and (13) can be used to calculate, for example, the relative concentrations of implanted atoms in a given target or the absolute number of the implanted atoms per cm^2.

2.2 Channeling Effect

2.2.1 General Description

A great variety of physical phenomena can occur when an energetic beam of charged particles is incident upon a solid target, e.g., Rutherford scattering, energy-loss processes, nuclear reaction and X-ray production.

All of these processes have cross sections which depend on the target atoms. If the target material is amorphous, the impact parameter distribution is independent of the relative orientations of the beam direction and the target. Therefore the observed yields of interaction processes between beam and target are also orientation-independent.

When the target material is monocrystalline, the situation becomes quite different. The distribution of impact parameters and yields of physical processes are found to be very strongly dependent on the relative orientations of the beam and the target. This orientation dependence is commonly called the channeling effect.

Before the discovery of the channeling effect, Davies and coworkers /22/ reported anomalously long ranges for heavy ions stopping in polycrystalline aluminium and tungsten. After this Robinson and Oen /23/ performed a computer calculations on the slowing down of 1-10 keV Cu atoms in various crytsals, they found abnormally large penetrations for those ions with initial velocities lying close to principal axial directions. These computations indicated that the long ranges observed by Davies and coworkers could be attributed to ion channeling in the polycrytsalline targets. The dependence of low energy heavy ions

ranges in monocrystalline targets on the incidence direction was measured by many authors /24 -26/. The channeling effect was also observed /26/ for accelerated protons transmitted or backscattered from a single crystal of gold.

The fact that the trajectories of particles with energies of several MeV can be so strongly influenced by atomic potentials of the order of a few eV is a consequence of the collective nature of the channeling process. Nelson and Thompson /28/ showed that channeling could result from a series of glancing collisions with lattice atoms, and they derived an effective transverse potential governing the oscillatory trajectories of the particles. For an ion with kinetic energy E incident on a monocrystalline target in a direction making a small angle ψ with the crystal rows, the total transverse energy $E_\perp$ can be given by

$$U(\bar{r}) + E \psi^2(\bar{r}) = E_\perp \qquad (14)$$

where $U(\bar{r})$ is an effective potential which describes the interaction of the incident particles with the atoms of the rows. $\bar{r}$ is the incident vector of the particle in a plane perpendicular to the row. $\psi(\bar{r})$ is the angle between the crystal direction and the tangent to the particle trajectory at the point $\bar{r}$.

For an ideal crystal (Fig. 2a) the particle has an almost constant transverse energy $E_\perp$, and will be kept in the channel. However already for perfect crystals (Fig. 2b) without defects but with thermal vibrations, the transverse energy $E_\perp$ will increase with increasing penetration depth. At a certain range the particle will have enough transverse energy to make a collision with

large angle and escapes from the channel. This is the
so called dechanneling effect. The interaction with the
target electrons and also with crystal defectes (Fig. 2c)
for example dislocations or distortions around the dis-
locations will enhance the dechanneling process.
The channeling effect can be used for example to

determine the thermal vibration amplitude of the lattice

atoms, the lattice defects and the lattice location of the
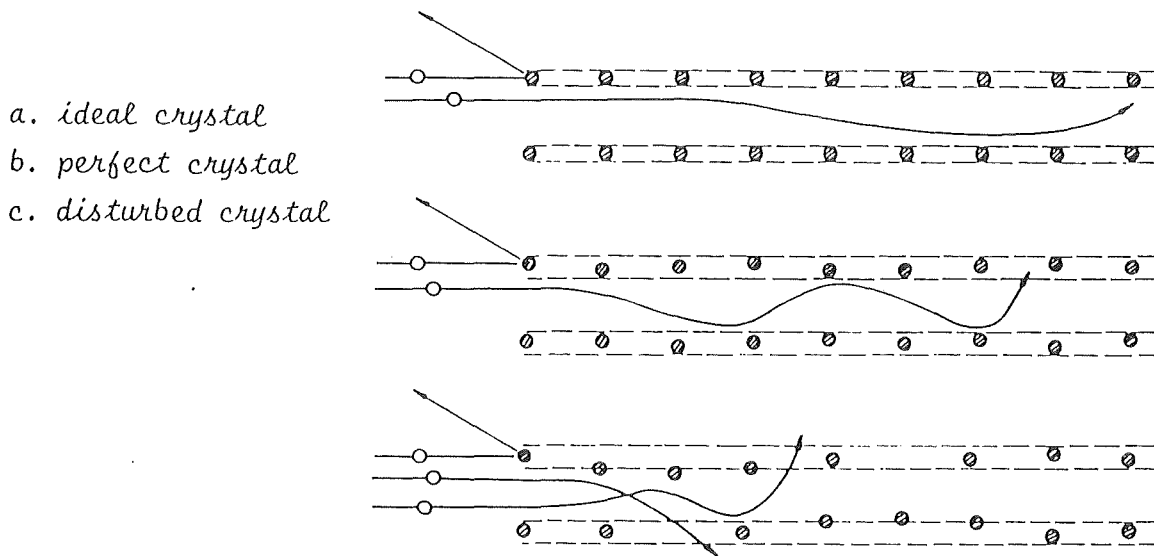
impurity atoms in a crystal /27, 28/.

a. *ideal crystal*
b. *perfect crystal*
c. *disturbed crystal*

Fig. 2   Principle of channeling effects in ideal,
         perfect and disturbed crystals.

2.2.2 Classical Theory of Channeling: Continuum Model

From a classical viewpoint, a positively charged
particle can be considered to be channelled with respect
to a row of atoms if it is incident upon the row at some
angle (ψ) small enough that it is reflected from the row
by a correlated series of many consecutive glancing colli-
sions with atoms in the row. As the incidence angle becomes
greater than some critical angle (ψ_c), the particle begins
to approach the row so closely that the trajectory no lon-
ger can remain channeled. Instead, the particle begins
to feel individual atoms and will rapidly be scattered
away from the row by single (or at most a few) collisions.
For $\psi \gg \psi_c$, the particle can be considered to be travel-
ling randomly with respect to the row. Similar considera-
tions apply to a plane of atoms.

Lindhard /29/ demonstrated that classical mechanics
can in fact be applied to the channeling case. Thus, it is
central to the classical idea of channeling that the en-
counters of channeled particles with row or planes of atoms
be determined by many small-angle scatterings. Under these
conditions, the continuum model /30, 32/ asserts that to a
good approximation the motion of channeled particles is de-
termined by a continuum potential, i.e., a potential ob-
tained by averaging over a direction parallel to the row or
plane. Fig. 3 illustrates the collisions of a channeled
particle. The crystal is pictured, for the moment, as an
idealized simple static array of identical atoms. The
continuum interaction potential at a distance (ρ) from the
row is

$$V_{RS}(\rho) = \frac{1}{d} \int_{-\infty}^{+\infty} V[(\rho^2+x^2)^{1/2}]dx \qquad (15)$$
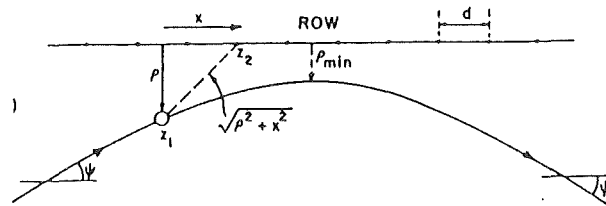
Fig. 3 Collision of channeled particles with an idealized static linear array of atoms

The subscripts R and S denote row and static.
V is the static ion-atom interaction potential which is given by the Thomas-Fermi formula

$$V(r) = (Z_1 Z_2 e^2 / r) \, \phi(\rho/a) \qquad (16)$$

where $\phi(\rho/a)$ is the Thomas-Fermi screening function tabulated by Gombas /33/, $\phi(\rho/a)$ can also be given by the analytical approximation due to Moliere /34/:

$$\phi(\rho/a) = \sum_{i=1}^{3} \alpha_i \exp(-\beta_i \cdot \rho/a) \qquad (17a)$$

where $\{\alpha_i\} = \{0.1, \ 0.55, \ 0.35\}$ and $\{\beta_i\} = \{6.0, \ 1.2, \ 0.3\}$
and a is the Thomas-Fermi screening radius given by

$$a = 0.8853 \, a_o \, (Z_1^{1/2} + Z_2^{1/2})^{-2/3}$$

a_o is the Bohr radius.

Following Lindhard's /29/ approximation, the Thomas-Fermi screening function can also be given by

$$\phi(\rho/a) = 1 + [1+(c \cdot (\rho/a))^2]^{-1/2}, \quad c = 3$$

Equation (15) may then be written as

$$V_{RS}(\rho) = (2\ z_1 z_2 e^2/d)\ f_{RS}(\rho/a) \qquad (18)$$

$$= E\ \Psi_1^2\ f_{RS}(\rho/a)$$

where

$$\Psi_1 = (2\ z_1\ z_2\ e^2/E \cdot d)^{1/2} \qquad (19)$$

E is the projectil energy.

A graph of the function $F_{RS} = [f_{RS}(\rho/a)]^{1/2}$ is given by Gemmel /28/ . For Lindhard's approximation $f_{RS}(\rho/a)$ is given by

$$f_{RS}(\rho/a) = \ln(1+c^2 \cdot a/\rho)^{1/2}$$

Inside a crystal lattice, the continuum potential experienced by an axially channeled particle will be the sum of the potentials due to all of rows of atoms in the crystal. Thus, for the static case the total potential measured at a position $\vec{r}$ in the plane normal to the axial direction is given by

$$U_{RS}(\vec{r}) = \sum_i V_{RS}\ (|\bar{r}-\bar{r}_i|) - U_{RS}^{min} \qquad (20)$$

where $\bar{r}_i$ are the positions of the atomic rows measured in the normal plane. U_{RS}^{min} is a constant substracted in order to make the minimum value of $U_{RS}(\bar{r})$ equal to zero. For a channeled particle travelling at small angles with respect to atomic rows or planes, the longitudinal component of the velocity may be treated as constant, if

energy loss processes are neglected. Then, in the
continuum model, the trajectory of the particle can
be completely described in terms of the motion in the
transverse direction. For small angle (Ψ_o) between
the particle trajectory and the row of atoms, the trans-
verse energy is equal to ($E \, \Psi_o^2$). The distance of
closest approach to the row (ρ_{min}) is given by the so-
lution of the equation of motion

$$E \, \psi_o^2 - V_{RS}(\rho) - E \, \Psi_o^2 (b/\rho_{min})^2 = 0 \qquad (21)$$

where b is the impact parameter of the collision when
projected onto the normal plane. In the special case
where the trajectory and the atomic row are coplanar,
e.g. (21) reduces to

$$E \, \Psi_o^2 = V_{RS}(\rho_{min}) \qquad (22)$$

The critical angle of incidence, beyond which the
distance of closest approach becames less than the criti-
cal distance (ρ_c), for sustaining a stable channeling
trajectory is given by

$$\Psi_c = [V_{RS}(\rho_c) \, / \, E]^{1/2} \qquad (23)$$

$$= F_{RS}(\rho_c/a) \, \Psi_1 \qquad (24)$$

where Ψ_1 and $F_{RS}(\rho/a)$ are defined in eqs. (18) and (19).
As a rough estimate of (ρ_c) in eq. (24) Lindhard /31/
suggested $\rho_c \cong a$. Inserting this value in eq. (24) yields
$\Psi_c \cong 0.83 \, \Psi_1$.

If thermal vibrations are taken into account, both the continuum potential and the critical distance of closest approach (ρ_c) will be affected. The continuum potential experienced by the particles is that obtained by averaging over the thermal displacements of the atoms.

An expression for the continuum potential in this case was derived by Appleton et.al. /35/ and also by Barrett /36/, assuming that the individual atoms vibrate independently. The closest approach (ρ_c^t) at temperature (t) will be

$$\rho_c^t = (\rho_c^2 + u_\perp^2) 1/2 \tag{25}$$

where $u_\perp$ is the rms value of the thermal vibration amplitude normal to the axis, which may be estimated from the Debye approximation, [e.g. /37/].

The minimum yields χ_{min} predicted by continuum model are in essence the geometrically determined fractional areas for which channeling trajectories are not possible when a beam is aligned with an axis or a plane. Within these areas, the initial transverse energy is above the critical value. Thus the value for an axis, in the case of static crystal, is

$$\chi_{min} = Nd \ \pi \ \rho_c^2 \tag{26}$$

where N is the number of atoms per unit volume in the crystal, taking into account the thermal vibration, the minimum yield χ_{min} will be

$$\chi_{min} = Nd \ \pi(\rho_c^2 + u_\perp^2) \tag{27}$$

The continuum model has been discussed here in some detail because in general it fairly successfully predicts such important features as angular width and minimum yields and their dependences on several fundamental parameters (e.g. Z_1, Z_2 and E). Thus far, the slowing down of the particles inside the crystal and the orientation dependence of the stopping power are neglected. Also multiple scattering, which leads to changes in the transverse energy and to dechanneling effects, have been ignored.

2.2.3 Distribution of Particle Flux

The flux of beam particles in the region below the surface is far from uniform both in the depth (X) and in position (r for axial case, z for planar case) on the transverse plane. This is indicated by the existance of a peak in the calculated normalized nuclear encounter probability (P_{NE}) at $X = 1/2 \lambda_{ch}$ where λ_{ch} is the classical wave length of the oscillating channeled trajectories /36/. Thus a peak in the particle flux should exist at $X = 1/4 \lambda_{ch}$, $z = o$, i.e., for zero incidence angle most of the beam particles will cross the center of the channel at about $X = 1/4 \lambda_{ch}$. From statistical arguments, it is shown that, as the beam progresses more deeply into the crystal there is a trend towards equilibrium on the transverse energy shell /29/. That is, at sufficiently large depths, particles of a given transverse energy are distributed uniformly over the area, which is energetically accessible to them in the transverse plane. Typically, depths of a few microns are needed to reach the equilibrium although this depth varies markedly with factors such as the incident energy and the crystal orientation.

For depths where equilibrium has been attained, the flux distribution can be calculated analytically as described in Ref./28/:

$$F(r,X) = \int_{U_{RS}(r)}^{\infty} \frac{g(E_\perp,X)}{A(E_\perp)} \, dE_\perp \tag{28a}$$

where

$g(E_\perp,X)$ is the normalized distribution function for the transverse energy.

$A(E_\perp)$ is the area in the transverse plane accessible to a particle with transverse energy $E_\perp$.

$U_{RS}(r)$ is the static continuum potential defined by Eq. (20).

The normalization in Eq. (28a) is such that $F(r,X) = 1$ corresponds to the flux just before the beam enters the crystal. As $g(E_\perp, X)$ is peaked toward low transverse energies /38/, the flux distribution will be sharply peaked near the center of the channel and can attain values many times the random value.

If the transverse energy distribution is assumed to be unaltered from its form at $X = 0$, and if A_i represents the area inside a special potential contour (i) then Eq. (28a) reduces to

$$F_i = \int_{A_i}^{A_o} dA \, / \, A = \ln(A_o/A_i) \tag{28b}$$

where

F_i is the flux at the ith contour

A_o is the cross-sectional area of the channel.

It is noted that Eq. (28b) gives a flux distribution which sharply peaks towards zero transverse energy.

The particle flux distribution is very sensitive to effects, such as beam energy, beam divergence, incident angle, amorphous layers, crystal defects, impurities and temperature. The midchannel flux shows a very rapid falloff with increasing the tilt angle Ψ and reaches the random value at about 0.2 to 0.3 degree.

2.2.4 Applications

A variety of practical uses have been found for channeling effects such as location of dopant and impurity atoms, studies of lattice disorder, and studies of surfaces and epitaxial layers. The use of the channeling effect for lattice location studies will be discussed here in some detail because it will be used in this work to identify the occupied lattice position of different implanted atoms in single crystals. The principle of the method (illustrated in Fig. 4) is that interstitial impurity atoms experience a particle flux that depends, often very strongly, on the channeling orientation, whereas subatitutional impurity atoms experience approximately the same flux as that experienced by the atoms of the host crystal for all crystal orientations. The method can make use of any close encounter process that shows a strong channeling effect. The choise is usually determined by the relative masses of the host and impurity atoms. Thus, for impurity atoms much heavier than the host atoms, Rutherford backscattering is normally the most attractive possibility since the energy differences due to kinematical effects permit one to distinguish between scattering from host and impurity atoms; sometimes a heavy ion beam is necessary in order to make this distinction.

If the impurity atoms have a mass lower than that of
the host atoms, nuclear reactions especially those
with a high positive Q-values offer a means of distin-
guishing some of the more common dopants /39 -43/.
Characteristic X-ray may also be used /44/ although
the depth resolution obtained is usually poor.
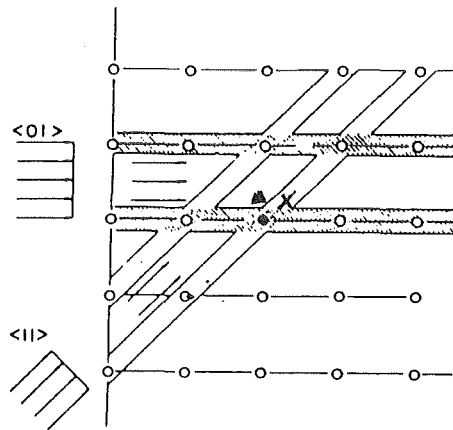
	$\chi^i_{min}/\chi^h_{min}$		lattice position
	< 01 >	< 11 >	
●	1	1	substitutional
X	> 1	1	interstitial
Δ	> 1	> 1	random position

Fig.4 Two dimensional model illustrating how
the channeling effect can be used to
locate foreign atoms in crystals. χ^i_{min}
and χ^h_{min} are the minimum yield for
impurity and host respectively.

2.3   Ion Implantation

Ion implantation is a process by which nearly
all elements can be introduced into near surface regions
of materials without any metallurgical constraints. The
concentration and the depth distribution can be well
controlled, leading to a high degree of reproducibility
in altering chemical and physical properties. Ion ranges,
range distributions and disorder profiles will be gover-
ned by collisions with the target atoms in the slowing-
down process.

2.3.1   Atomic Collisions and Energy Loss

The interaction of the incident ion with the tar-
get atoms which leads to energy loss can be divided in
two separate processes. The interaction with screened
target nuclei (elastic energy loss) and the interaction
with the electrons (inelastic energy loss). Then the total
energy loss can be written as

$$(- \frac{dE}{dx}) = (- dE/dx)_n + (- dE/dx)_e \qquad (29)$$

where the subscripts n and e refers to nuclear and
electronic, respectively.

The atomic stopping cross section S can be expres-
sed by $dE/(N \cdot dx)$ in $eV \cdot cm^2$. Considering the slowing down
process as a series of binary collisions S can be described
by

$$S = \sum_i T_i P_i = \int_{T_{min}}^{T_{max}} T \, d\sigma \qquad (30)$$

where T_i is the kinetic energy transferred to the i-th
target atom in elastic nuclear collision ($S \equiv S_n$) or to
the i-th electron in the inelastic electronic collisions

$(S \equiv S_e)$ with a probability P_i for an energy transfer between T and T + dT. The integral extends over all possible energy losses in the individual collisions and $d\sigma$ is the cross section for the energy transfer. The range of the projectile is obtained as

$$R(E) = \int_0^{E_O} dE/(S \cdot N) \qquad (31)$$

In order to evaluate eqs. (29) and (30) one has to consider separately elastic and inelastic collision processes.

2.3.1.1 Elastic Collisions

The general solution of the equations of motion of two point masses in a central force field is the well-known sacttering integral which provides the connection between the angle of deflection ϕ in the center of mass system and the impact parameter P

$$\phi = \pi - 2p \int_0^{r_{min}} dr/(r^2 \cdot \{1-V(r)/E_R-p^2/r^2\}^{1/2} \qquad (32)$$

where r is the distance between the masses M_1 and M_2, r_{min} is the minimum distance of approach, E_R is the relative energy of collision, $E_R = M_2 \cdot E_c/(M_1+M_2)$, V(r) is the interatomic potential. Since the system is conservative, the energy transfer for a given scattering angle ϕ is independent on the form of the interaction potential. Thus the final asymptotic values of velocities and energies can be calculated by just considering energy and momentum conservation in the center of mass system. The energy transferred to a target atom is $T = E_O - E_1$ with E_O and E_1 being the energies of the incident particle before and after the collision, respectively, is then given by

$$T = E_O \cdot \{[4 \, M_1 M_2/(M_1+M_2)^2] \cdot \sin^2 \phi/2\} \qquad (33)$$

The maximum transferred energy in a head-on collision is

$$T_M = [4 \, M_1 M_2 / (M_1 + M_2)^2] \cdot E_o$$

The differential scattering cross section $d\sigma$ for the scattering process with impact parameters between p and p+dp and scattering angle ϕ and $\phi + d\phi$ is given by

$$d\sigma = 2\pi \, p \, pd \qquad \text{and} \qquad d\sigma/d\Omega = p \, dp/(\sin \phi \, d\phi) \qquad (34)$$

Equation (34) provides the dependence between ϕ and p. Thus, in order to calculate energy transfers and differential cross sections for a given energy transfer, eq. (34) has to be solved completely. This can be done numerically for all potentials, analytically however only for interaction potentials with the form $V(r) = C/r^S$. These inverse power potentials represent the Coulomb potential for S = 1, the Nilson potential for S = 2 and the hard core potential for S = 0. The total collision cross section σ_{tot} is infinite for real potentials
$$\sigma_{tot} = \int_{p=0}^{\infty} d\sigma$$
and finite for the hard sphere case (from p = 0 to p = r_{min}). The case S = 1 was first treated by Rutherford and resulted in the famous Rutherford differential scattering law for α-particles penetrating thin films (see eq. 3) The differential cross section can conveniently be evaluated in the so-called momentum approximation when P is large or E_o is large and ϕ is small and in the hard sphere approximation for nearly head-on collisions where p is small and the deflection angle is large. Lindhard /45/ has provided the inverse power potential as a good approximation to the scattering integral for all values of S. Besides the power law potential, screened potentials are used, especially the Thomas-Fermi-Potential eq. (16).

Universal curves are obtained for both the stopping power and the range energy relation by introducing dimensionless parameters ρ and ε for the range and energy,

respectively

$$\rho = R.N.4 \cdot \pi a^2 \frac{M_1 M_2}{(M_1 + M_2)^2} \tag{35a}$$

$$\varepsilon = E \frac{a M_2}{Z_1 Z_2 e^2 (M_1 + M_2)^2} \tag{35b}$$

With these parameters the differetnial scattering cross section can be given by a one-parameter equation /45/

$$d\sigma = \pi a^2 f(t^{1/2}) \cdot dt/(2 \cdot t^{3/2}) \tag{36}$$

where $t = \varepsilon^2 \sin^2 \phi/2$. Evaluation of eq. (30) leads to an universal expression for S_n

$$S_n = - 4 \pi a^2 \frac{M_1}{M_1 + M_2} \frac{Z_1 Z_2 e^2}{a} \left(\frac{d\varepsilon}{d\rho}\right)_n \tag{37a}$$

where $\left(\frac{d\varepsilon}{d\rho}\right)_n = \frac{\ln \varepsilon}{2 \varepsilon (1 - \varepsilon^{-3/2})}$ \tag{37b}

The universal curve for S_n is shown in Fig. 5 /46/ page 29 revealing a maximum for $\varepsilon \leq 1$.

2.3.1.2 Inelastic Collisions

The treatment of electronic stopping is more complex. For the high energy region S_e reveals a maximum for a projectile velocity $V_1 = Z_1^{2/3} V_0$ with Bohr's velocity $v_0 = e^2/h$ (see Fig. 5). For velocities larger than V_1, S_e decreases with $1/E$. In this energy region which is called the Bethe-Bloch region, energy is transferred to single electrons. S_e is given by /47/:

$$S_e = \frac{4\pi \, z_1^2 z_2 e^4}{m_e v^2} \, [\log \frac{2m_e v^2}{I} + \ldots] \tag{38}$$

This energy region is important for materials analysis with light ions in the MeV region. In the low energy region, which is important for slow moving heavy ions as in the case of ion implantation, it is seen in Fig. 5 that no longer a universal curve exists for S_e. There S_e is seen to increase linearly with $\varepsilon^{1/2}$ and the proportionality factor k is 0.14 ± 0.03 as long as $z_1 \gtrsim z_2$. In this low energy region all electrons are excited collectively and the plasma frenquency (ω_p) of the host lattice electrons becomes important, Firsov /48/ considered a simple geometrical model of momentum exchange between projectile and target atom during interpenetration of electron clouds. The often used proportionality factor k as given by Lindhard /45/ is

$$k = \frac{0.0793 \, z_1^{2/3} \, z_2^{2/3} \, (M_1+M_2)^{3/2}}{z^{1/2} \, M_1^{3/2} \, M_2^{1/2}} \tag{39}$$

2.3.2 Range and Range Distribution

The reduced range $\rho(\varepsilon)$ can now be determined by evaluating eq. (31) in reduced parameters ρ and ε. This equation gives the average total path length for an ion slowing down from an energy E_0 as the total path is composed of many small pieces in the different directions caused by large angle deflections. The total average path length projected on the original direction of the incident ion is defined as the projected range R_p. Clearly, for individual projectiles the number of collisions, the transferred energy and thus the total path length will vary and the variation can be described by

a Gaussian distribution curve to express the distribution curve of implanted ions, $N(x)$

$$N(x) = N_p \exp(-0.5 \ [\frac{x-R_p}{\Delta R_p}]^2) \qquad (40)$$

The peak concentration is $N_p = N_s / (\sqrt{2\pi} \cdot \Delta R_p)$ $\cong 0.4 \ N_s/\Delta R_p$ where N_s is the number of implanted ions/m^2, and ΔR_p is the standard deviation. At $x = R_p \pm \Delta R_p$, $N(x) = n_p/\sqrt{e}$.

Values for the average projected range R_p and the average standard deviation of the projected range ΔR_p are presented in tabular or graphical form /49-52/ mostly based on the LSS-theory /53/.
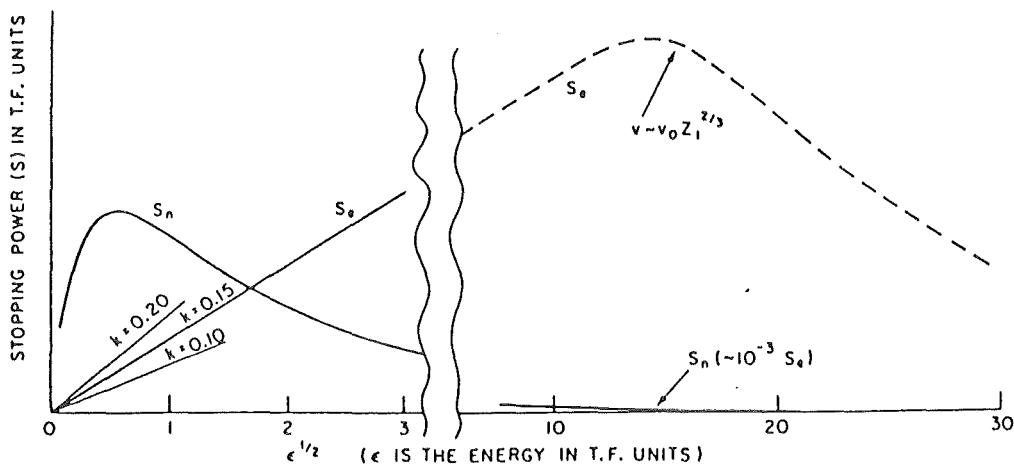

Fig. 5   Energy dependence of the nuclear (S_n) and electronic (S_e) stopping powers in dimensionless units. in modified version from /46/

2.3.3 Radiation Damage and Collisional Cascade

There are many kinds of interactions between
energetic particles and solids. Interesting is the
atomic displacements and transmutations caused by heavy
ions (Z>1) with different atomic masses. Particle ener-
gies are typically in the MeV range, in comparison to
about 25 eV needed for an energetic atom to displace
a lattice atom of comparable mass. The threshold energy
for displacement E_d, depends on the metal or alloy, the
crystal structure, and the direction of displacement.
A value of about 25 eV, independent of material and ave-
raged over the varous possible directions for displace-
ment is sometimes taken as a reasonable estimate for E_d.
This 25 eV is far more than the typically 5 eV energy
needed for thermal formation of self-interstitials because
of the highly irreversible nature of the displacement event,
which must require more energy than the equilibrium ther-
mal creation process.

An atom which has been displaced by a bombarding
particle is known as a "primary knock-on atom "(PKA) which
may have an energy from the eV to the keV range. PKAs
with energies below E_d cannot displace further atoms and
will loose their energy due to various inelastic inter-
actions which cause only very localized heating of the
lattice. The more energetic PKAs may create one or a num-
ber of secondary knock-ons, which in turn may displace
other atoms. Thus we obtain an avalanche-like process of
moving atoms which distribute the energy in successive
collisions until the energy is below about E_d. A good de-
monstration of such an avalanche-like cascade production
is given in Fig. 6 where computer calculations are shown
simulating the slowing down process for 100 keV Ar-ions
in Cu /54/. Individual cascades, called subcascades can
be seen to be formed along the track of the primary ion.

The number of the subcascades formed and their distribution has to be taken into account in order to estimate the deposited energy density in a special ion-target combination. Under certain conditions, for example for low energy heavy ions implanted into a heavy mass target the probability for subcascade formation is less pronounced and the damage is uniformly distributed through the volume of a single cascade. Volume correction factors as a function of the mass ratio (M_2/M_1) have been evaluated /55/.

The number of displaced atoms N_d within a cascade can be evaluated. starting with eq. (37) which give the nuclear stopping S_n via primary collisions during the slowing down process of the primary incident ion.

In addition the slowing down process of secondary energetic recoils has to be considered and it has to be noted that the energy loss is again due to both electronic excitations and nuclear collisions, ν (E). Therefore $\nu(E)$ is about 20 to 30% smaller than the integrated nuclear stopping power value of the primary ion. Assuming that only those recoiled atoms become displaced which received an energy $E > E_d$, the total number of displaced atoms is obtained by dividing $\nu(E)$ by $2 E_d$ /56/

$$N_d = \frac{0.8 \ \nu(E)}{2 \ E_d}$$

The number of displaced atoms N_d observed experimentally in metals, although irradiated at 4 K, is usually about a factor of 10 smaller than predicted and saturates with increasing dose, suggesting that a large amount of spontaneous recombinations occurs during cascade production.
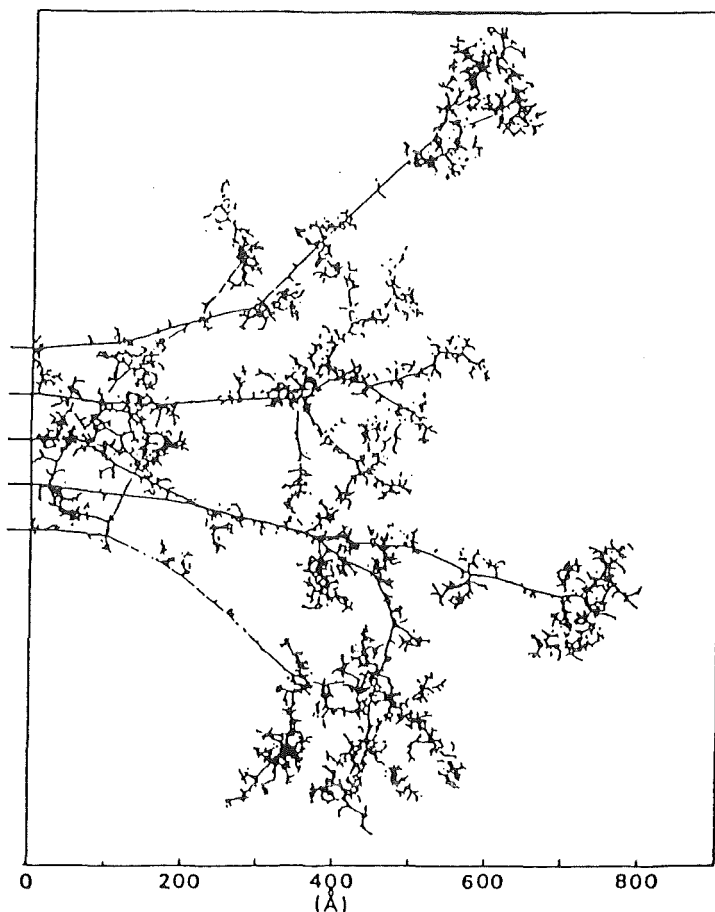
Fig. 6
Two dimensional individual
cascades as simulated in
computer calculations (100 KeV
Ar → Cu) /54/

The time development of the collisional cascade
as determined from molecular dynamic calclulation
/58/ is shown in Fig. 7. In the first stage $(10^{-13}$ sec)
the number of displaced atoms (N_d) increase and reach a
maximum value, then the spontaneous recombinations of
the closest unstable pairs $(5 \times 10^{-13}$ sec) starts
(cascade collapse). At the end of the cascade life-
time $(1-5 \times 10^{-12}$ sec), the cascade region reaches local
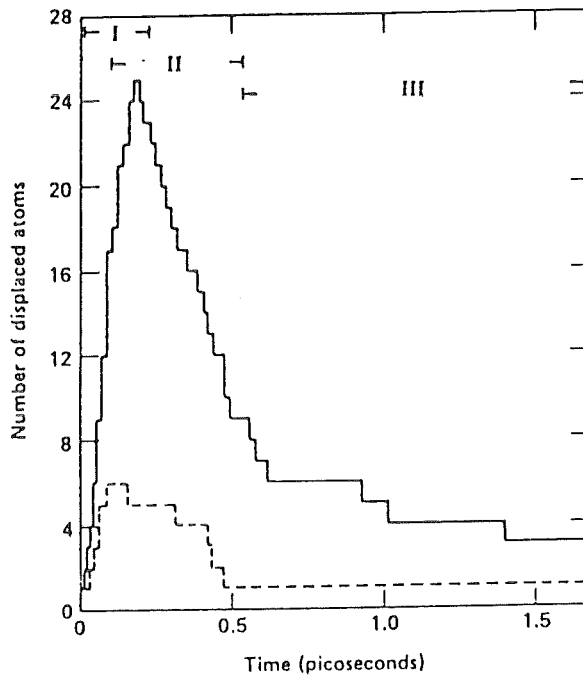thermal equilibrium with its surroundings.

Fig. 7   Time development of two collision cascades.
The number of displaced atoms is given as a
function of time for a 600 eV (---) and
2.5 keV (——) collision cascade /57/

2.4   Replacement Collision Theory

Energetic heavy charged particles penetrate in-
to a crystal target and interact with the lattice atoms
resulting in so-called collisional cascade. Besides the
quantities under investigation in this field at present,
such as the number of defects produced in a cascade and
their spatial distribution, it is of interest to know the
final fate of the incident ion. Does it come to rest as
an interstitial atom or does it end up on a substitutional
lattice site? At low enough temperatures where no diffu-
sion takes place, the latter case may occur during the
slowing down process if the ion displaces a lattice atom
but retains so little energy itself that it becomes trap-
ped in the vacancy just created. The probability of such
processes is called the replacement collision probability.

In principle the result of a replacement collision can not be separated from the recombination process of neighbored impurity vacancy pair.

The calculation of the replacement collision probability assumes binary collisions between the incident ions and the target atoms. A struck target atom is considered to be displaced if it receives a kinetic energy T, greater than E_d the displacement threshold energy. The scattered ion is assumed to be captured by the resultant vacancy if its remaining kinetic energy, E-T, is less than E_c, the capture threshold energy. The value of E_c has been taken to be equal to E_d which is equal to 25 eV for most metals and semiconductors. Consequently, the incident ion makes a replacement collision, whenever both the following eqs. are fulfilled:

$$\varepsilon = E - T \leq E_d$$

and

$$T \geq E_d \qquad (42)$$

For the sake of simplicity the inelastic energy losses which are likely to happen at higher energies and the regular arrangement of the lattice atoms are neglected /15/. The importance of replacement collisions in radiation damage processes was apparently first recognized by Kinchin and Pease /56/. Subsequently, Dederichs et.al. /15/ constructed the following integral equation to calculate the probaility P(E) for primary recoil atom, that is, for ion mass (M_1) equal to target atom mass (M_2), as a function of the incident ion energy E:

$$P(E) = \int_o^{E_1} g(\varepsilon,E)d\varepsilon + \int_{E_d}^{E} P(\varepsilon)g(\varepsilon,E)d\varepsilon \qquad (43)$$

Where

$$E_1 = \begin{cases} (E - E_d) & \text{for } E < 2 E_d \\ E_d & \text{for } E \geq 2 E_d \end{cases}$$

and $g(\varepsilon,E)$ is the probaility that an ion with energy E interacts with a target atom and its remaining kinetic energy, is ε. The first term in eq. (43) represents the probility that the ion makes a replacement in the very first collision. The second term represents the probaility that it makes a replacement collision later on.

Dederich et.al. analytically solved the exact integral eg. (43) for the hard-sphere as well as for other interaction potentials. The exact result is

$$
P(E) = \begin{cases}
\ln(E/E_d) & \text{for } E_d \le E \le 2\,E_d \\
\\
\ln 2 \cong 0.693 & \text{for } E \ge 2\,E_d
\end{cases} \tag{44}
$$

Anderson /58/ proposed that replacement collisions might play an important role in the substitutional doping of semiconductors by ion implantation and evaluated the probability for $M_1 \ne M_2$ using the continuous slowing-down approximation. He calculated the high energy value of P(E) for the hard-sphere case and also for a $(1/r^2)$ interaction potential. His basic expressions for the probality function neglects "beam attenuation" due to elastic collision, and therefore the result over-estimates P(E).

Brice /14/ solved numerically the exact integral equation governing P(E) which are obtained utilizing the Thomas-Fermi elastic sacttering cross section. The replacement probaility is determined through two parameters ρ and γ defined as

$$\gamma = 4M_1 M_2 / (M_1 + M_2)^2$$

$$\rho = c_m / (\pi b^2 \cdot E_d^{2\ m})$$

where

$$c_m = (\pi/2)\ a^2\ \lambda (M_1/M_2)^{1/2} (2\ z_1 z_2 e^2/a)^{2/3}$$

b is half the distance between the nearest neighbours in the crystal. λ and m are fitting parameters depending on the screening function $\phi(x)$ and have been taken as m = 0.33 and λ = 1.3091.

The result of the numerical solution is that, for larger values of ρ the probability P(E) has a strong oscillatory dependence on E/E_d in the low-energy region, but this behaviour dies out and the function approaches constant values at higher energies. The high energy limit, P_∞, is a monotonic function of γ. The curves for the lower values of ρ also approach a high-energy limit, but do not exhibit the oscillatory behaviour at low energies. The high-energy limit, P_∞ is normally reached at energies below E $\sim$ 1 -5 keV, which is the energy range of interest in most ion-implantation experiments.

Brice constructed a group of curves (see Fig. 8) containing P_∞ as a function of ρ at different values of γ. All the curves are quite similar in shape being monotonically increasing functions of ρ with relatively constant values at low and high ρ.

The information presented in Fig. 8 systematizes the determination of P_∞ for any ion and elemental target combination.
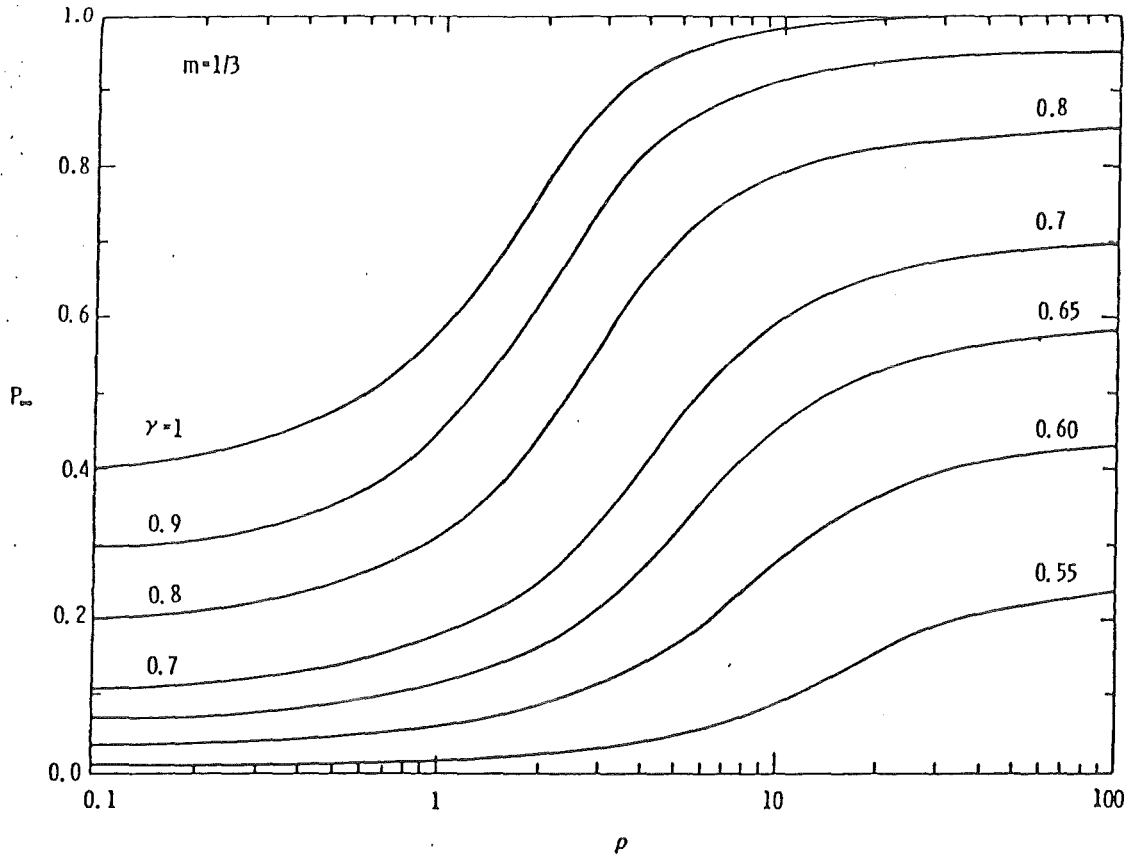
Fig. 8   The dependence of the high-energy limit of the
          replacement collision probability, P_∞, on the
          parameter ρ for several values of γ /14/

3. EXPERIMENTAL METHOD AND ANALYSIS

3.1 Sample preparation

Vanadium single crystals (0.9999 pure) in the form
of rods 6 or 10 mm diameter, with <111> or <110>
orientation respectively are cut about 10 degrees
off the surface normal in the form of 3 mm thick
disks using an diamond wheel. The disks surfaces are
lapped with 26 μ and 15 μ diamond paste using a disk
of 20 cm diameter, which could rotate at speed of
125 rpm, to remove the contaminations that have been
formed during the cutting. After lapping each crystal
is washed in methanol. The crystals are polished elec-
trolytically using a stirred mixture of 14% H_2SO_4 in
methanol /59/. The cathode is an platin foil and the
anode is the crystal itself. The current used for po-
lishing is about 2 to 5 amp. The optimum polishing
time is about 2 min. The crystals are quenched in me-
thanol and are dried in nitrogen gas.

3.2 Experimental set up

The block diagram of the accelerators, beam lines
and scattering chambers used in the experiments is
shown in Fig. 9. Two van de Graaff accelerators with
maximum energies of 3.5 and 2.5 MeV, respectively, are
used for the backscattering and channeling measurements.
The ion beam from the 2.5 MeV van de Graaff could be
deflected by an analysing magnet in 35 degrees, to be
used in the scattering chamber No. 1 for the low tem-
perature experiments, or in scattering chamber No. 2
for the room temperature experiments. The ion beam
from the 3.5 MeV van de Graaff can also be used for
the room temperature experiments in chamber No. 2.
The 350 keV ion implanter, described by K.G. Langguth
/60/ and P. Ziemann /61/, is used for the implanta-
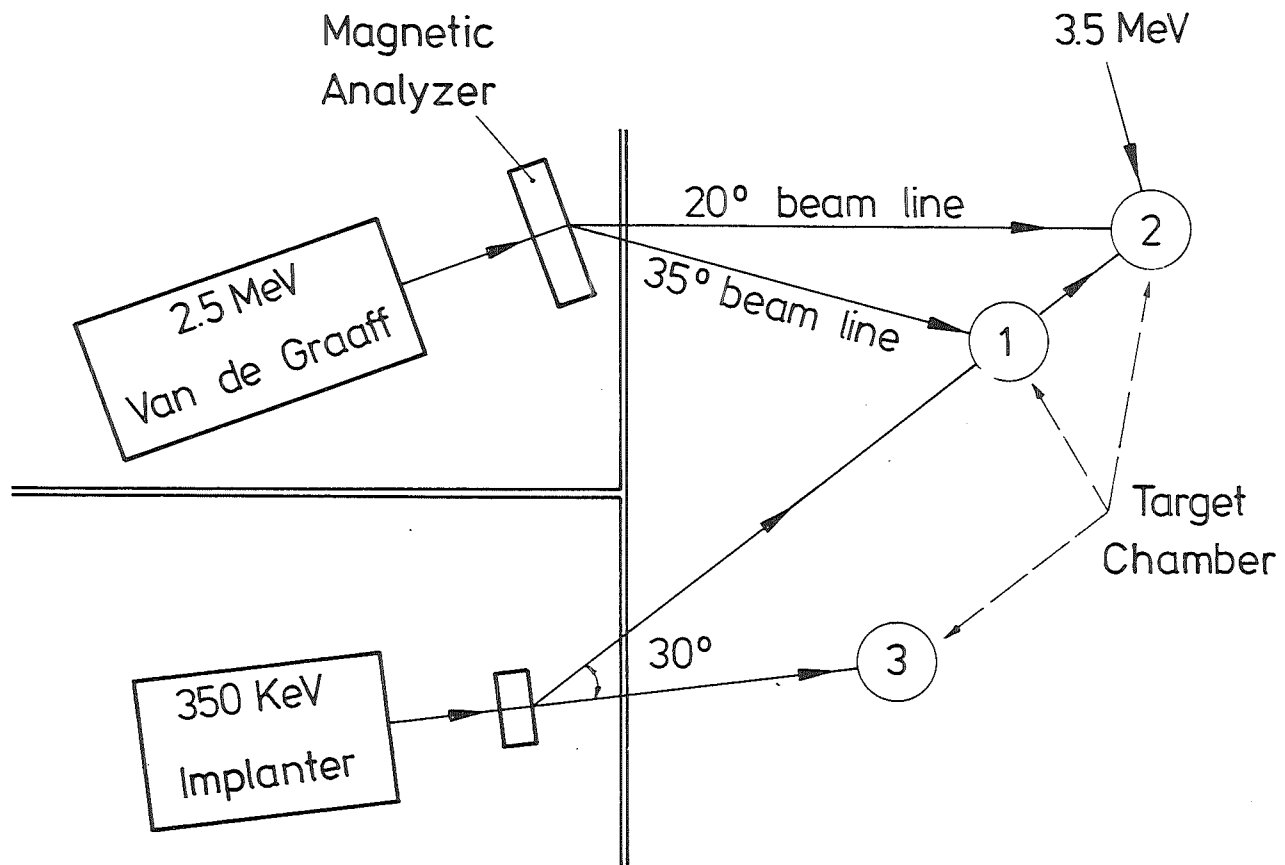tions. The ion beam from the implanter could be used

Fig. 9   Schematic diagram, illustrating the experimental arrangement used in the implantation, backscattering and channeling experiments.

either directly without deflection to perform the im-
plantations in chamber No. 3 at room temperature, or
deflected to be used for the low temperature implanta-
tions in chambers No. 1 and No. 2. The two axis cryo-
stat goniometer and the three axis goniometer, de-
scribed below are used in chamber No. 1 and No. 2,
respectively, for low and room temperature experiments.

3.3 Room temperature goniometer

For room temperature backscattering and channeling
measurements, an computer controlled three axis high
vacuum goniometer is used. The movements of the target
are carried out using four-phase step motors, which
are controlled with a NOVA-3 minicomputer (128 kByte
memory) through a CAMAC system. The precision of the
horizontal or vertical tilt angle is $\pm$ 0.02 degrees
while the precision of the rotation is $\pm$ 0.2 degrees.
The ion beam current is measured directly on the sample
holder, which is electrically isolated. The secondary
electrons are supressed with a negatively biased (-300 V)
Faraday screen supported in front of the target. The va-
cuum in the chamber is about 5 x 10^{-7} Torr during the
measurements.

3.4 Low temperature cryostat goniometer

For the low temperature implantation and in situ
analysis, a liquid helium cooled two-axis cryostat
goniometer is used /62/. The implantation and in situ
analysis have been carried out at 5 K, 77 K or 300 K.
The target can be rotated about the vertical axis of
a rotable He-vessel. The rotation about the target sur-
face normal is possible by a sample holder, which is
pressed against the He-vessel and driven via a warm
gear. The precision of the vertical rotation is

± 0.02 degree. The precision of the horizontal
rotation is ± 0.2 degree. The most important techni-
cal details of the low temperature goniometer are
shown in Fig. 10. The cryostat insert consists of
several parts: a flange (1), a liquide He-storage
vessel (2) and a sample holder (5) which is in
thermal contact with the He-filled chamber (3).
The He-filled chamber (3) consists of a Cu-block
with a cavity milled through the flange (4) into
the block. The slip of the sample holder (5) and
the thermal conduction to the He-chamber is im-
proved by inserting an In-foil.

The rotary motions of the goniometer are carried
out by four phase step motors, which are controlled
by a NOVA-3 minicomputer through a CAMAC system. The tem-
perature is measured by a Ge-resistor which is moun-
ted at the side of the He-chamber (3). The actual sample
temperature during irradiation is measured sometimes
by a Ge-resistor which is mounted at the sample posi-
tion. For an ion current of 20 nA of 2 MeV He ions,
a sample temperature of 5.5 K is measured. The sample
is electrically isolated by a piece of mica, at both
sides of the mica a thin In-foil is fixed to achieve
good thermal contact. The ion beam current is measured
directly on the sample by an ion integrator. The secon-
dary electrons are suppressed using an electrically
isolated and negatively biased (-300 V) aperture mounted
at the Cu-cooled shield (7).

The outer part of the cryostat is cooled by liquid
nitrogen before cooling down the liquid He-storage ves-
sel (2), to condense most of the restgas at the gonio-
meter wall. Proper shielding of radiation heat is
achieved by using two cooled shields (6) and (7). The
vacuum in the measuring chamber is mantained by a
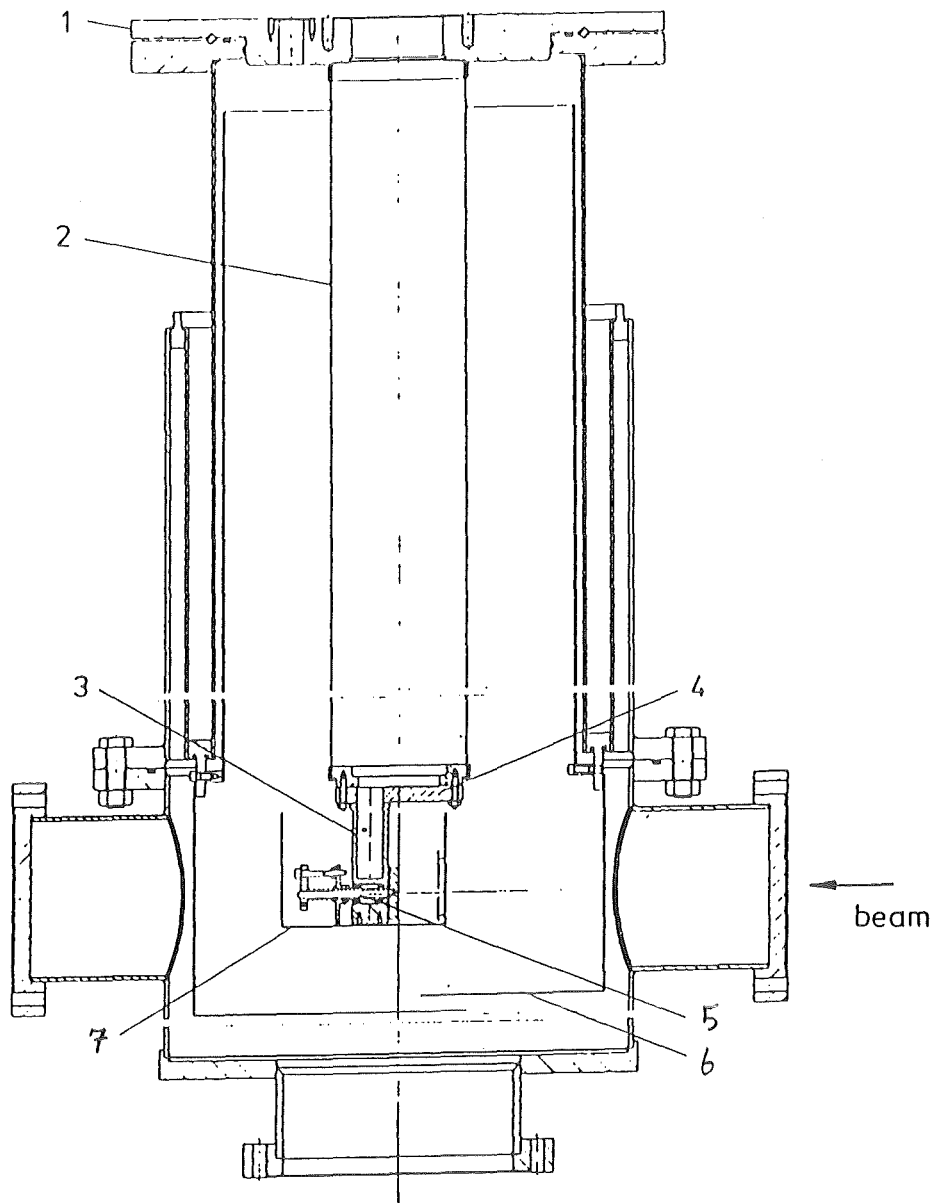turbomolecular pump. At room temperature a pressure

Fig. 10   Liquid He cooled two-axis goniometer
1.   Flange
2.   Liquid He storage vessel
3.   He-filled chamber
4.   Flange
5.   Sample holder
6.   Liquid N_2 cryoshield
7.   Liquid He cryoshield

value of about $5 \cdot 10^{-7}$ Torr and after filling the
cryostat with liquid He pressure a value of about
$1 \cdot 10^{-8}$ Torr is typical.

3.5 Data recording analysis

The backscattering He ions are detected (at
165 degrees to the incident direction) using a silicon surface barrier detector having a resolution of
16 KeV (FWHM). A commercial pulse pile-up rejector
is used with the electronic system /60/ to amplify and
restore the pulse from the detector in a NOVA-3
minicomputer (128 K Byte memory) serving as a multichannel analyzer.

It is noticed that the rate dependent background
due to pulse pile-up is an important factor limiting
the sensitivity of the backscattering and channeling
method to determine the lattice site occupied by the
implanted impurity atom at low impurity concentrations.
Therefore, beside using a pulse pile-up rejector, low
beam current (2 to 5 nA) is used for the measurements.
Also background corrections are performed for the energy spectra as well as for the angular scans of the impurities. Another important factor is the production
of defects by the incident beam used in the channeling
analysis. For low impurity concentration large beam
fluences are necessary to obtain adequate statistics.
This is followed by production of high concentrations
of beam-induced defects, which modify both the flux
distribution and the dechanneling rate in a manner
difficult to assess. If the lattice temperature is
high enough that the beam induced defects are mobile,
they can interact with the impurity atoms changing
there lattice positions. Therefore, the aligned spectrum

has to be measured first befor a high concentration
of defects is achieved. Angular scans and radnom spec-
tra can be measured later.

For accurate determinations of the lattice sites
occupied by the implanted impurity, random and alig-
ned energy spectra as well as angular yield curves in
different crystal directions, for the implanted atoms
and for the host atoms in the implanted region are
measured. The implanted impurity concentration is
determined from the random spectrum, using Eq. (12).
The impurity peak areas in the random and aligned
spectra have been corrected by subtracting the back-
ground, due to pulse pile-up, which is taken to be
linear and is estimated by taking the mean value for
the number of counts in 10 channels below and above
the impurity peak. In order to perform reliable cor-
rections in the angular scan measurements, 4 energy win-
dows are used: in the implanted region, at the impurity
peak, above and below the impurity peak. The mean va-
lues for the number of counts in the energy windows
above and below the impurity are used for the cor-
rections.

For a substitutional impurity, the ratio of aligned
to random yields for the impurity signal (χ^i_{min}) mat-
ches that of the host lattice (χ^h_{min}). The critical
angle, i.e. the half width at $(1+\chi_{min})/2$, of the an-
gular yield curves for the impurity ($\psi^i_{1/2}$) and for the
host lattice atoms ($\psi^h_{1/2}$) also match. The substitutional
fraction (f_s) of the impurity atoms in individual specific
crystal direction is given /20/ by:

$$f_s = (1 - \chi^i_{min}) / (1 - \chi^h_{min})$$

where the term $(1 - \chi^h_{min})$ is the fraction of the chan-
nelled beam. The critical angle of the impurity and

host atoms in the angular scans have to be compared. Smaller critical angle of the impurity atoms than that of the host atoms is an indication that the impuritiy atoms are displaced somewhat, for example 0.1 to o.2 $\overset{\text{o}}{\text{A}}$, from the well defined crystallographic lattice sites.

For impurity atoms on well defined interstitial lattice site, the aligned yield can be increased above the random value and a narrow peak in the angular yield profile can be observed. Such effects give evidence for both an enhanced flux concentration and a preferred site location in the center of the channel.

To determine the exact interstitial sites, one has to perform angular scans about various axial and planar directions. As a first step, one generally considers what are the possible preferred interstitial positions, and next determines what angular scans are required to distinguish between the different possible locations. It is noticed that, since there are often a number of possible sites, these may not be simple channeling directions where pronounced dips or peaks will be observed.

4. RESULTS

In order to draw conclusions on the basic processes which determine the lattice occupancy of implanted ions in single crystals a series of experiments have been performed which will be shortly outlined in the following. The influence of the chemical processes on the lattice site occupancy is studied by measuring the substitutional fraction, f_s, (using the Rutherford backscattering and channeling technique) for ions with different atomic mass and chemical properties implanted into vanadium single crystals. In order to avoid the influence of interactions between the implanted ions, the starting concentration is taken to be as low as possible (between 0.05 and 0.1 at.%) where the mean distance between two implanted ions is about 30 Å. The implanted ions concentration is then increased in steps to study possible precipitation effects.

The interaction between the mobile point defects and the implanted ions is studied by correlating the lattice temperature during implantation and in-situ channeling analysis (5 , 77 and 300 K) with the annealing stage of point defects in vanadium. The main annealing stage for self-interstitial atoms, SIA, is at 47 K /16/ although small annealing effects (2%) have been observed, already after irradiation at 3.8 K and subsequent annealing up to 4.7 K /17/. Stage III for vacancy migration lies between 200 and 300 K /18,19/. Thus, while impurity-point defects interaction is not probable during implantation at 5 K, interaction with SIA and with both SIA and vacancies are quite probable at 77 and 300 K, respectively.

Well separated single point defects have been further produced by postirradiation with light ions. These point defects may interact with the foreign atoms and may therefore affect simultaneously or after annealing their lattice locations.

The implanted elements are selected to be soluble (Cu, Sn, Au) or non-soluble (As, Se, Kr, Te, I, Xe, Ba, Cs, La, Ce, Pb and Bi) in the thermal equilibrium. The heat of solutions of

the studied systems varies between negative values (e.q.
-200 kJ/mol for Se) and large positive values (690 kJ/mol
for Cs) see Fig. 45 page 98. Only Bi from the elements,
which are substitutional after implantation at 300 K is
studied, as an example, after implantation at 5 K. The
other elements which are non-substitutional at 300 K are
studied after implantation at 5 K and 77 K.

Ga, In, Se, Bi and Cs are studied before by other
outhers /59,63/, after implantation, with relatively high
concentrations, into vanadium. They were all substitutional
after implantation at 300 K except Cs was non-substitutional.

4.1 Vanadium Single Crystals

Vanadium single crystals have to be oriented with respect
to the analyzing ion beam direction before the implantation.
Backscattering spectra as well as angular scans are performed
at 5, 77 and 300 K. The energy window for the angular scans
is adjusted in an energy region corresponding to a depth of
200 to 1000 $\overset{o}{A}$ (approximately equal to the projected range of
all the considered implanted ions). Examples of the <111>
aligned spectra measured at T_M = 300 and 5 K together with the
random spectrum are shown in Fig. 11a. The aligned yield at
5 K is significantly lower than that at 300 K because of less
dechanneling due to the reduced thermal vibration amplitude of
the vanadium atoms at 5 K. The same behaviour of the dechan-
neling yield at low temperatures can be seen in Fig. 11b, where
the angular scans for T_M = 300 and 5 K are shown. The minimum
yields and critical angles are indicated in the figure. A
typical value for the minimum yield (χ_{min}) at 300 K is about
0.03.

4.2 Highly Substitutional Implanted Systems

4.2.1 VCu and VAu

VCu: Because of insufficient mass resolution between V
and Cu in the backscattering spectrum, the substitutional frac-
tion (f_s) cannot be studied for Cu concentrations below 4 at.%.

A homogeneous Cu profile over a wide depth range gives better
statistics for the Cu peak at relatively lower concentration.
Three different energies are used to obtain a homogeneous
implantation profile of Cu which is calculated with a computer
program /64/ using R_p and ΔR_p values based on LSS theory /53/.
The calculated energy values and the corresponding fluences
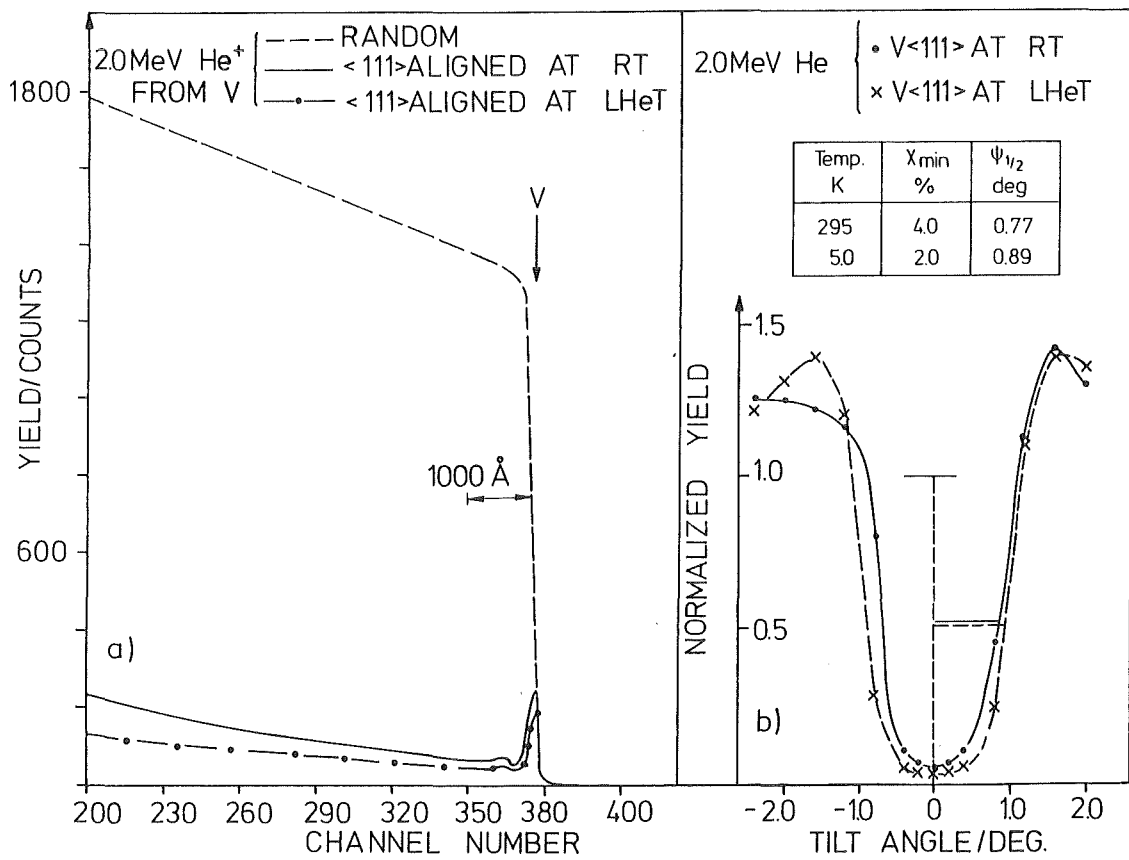used for 1 at.% Cu are shown in Table 1. The calculated Cu pro-
file can be seen in Fig. 12.

Fig. 11a. Random and aligned backscattering spectra from a V single
crystal. The <111> aligned spectra are measured at 300 K (——)
and at 5 K (-.-).

b. Angular yield curves for V single crystal with <111>-axial direc-
tion as measured at 300 K (——) and at 5 K (-x-). The values of
X_{min} and $\psi_{1/2}$ are inserted.

Table 1   Calculated energies and fluences necessary to get a homogeneous implantation profile for Cu-ions in vanadium. The value of projected range R_p and the standard deviation ΔR_p are also presented in the table. The given fluences produce a concentration value of 1 at.%.

E (keV)	R_p (Å)	ΔR_p (Å)	Fluences (ions/cm^2)
70	245	84	1.4×10^{15}
150	485	154	2.7×10^{15}
300	960	275	4.9×10^{15}
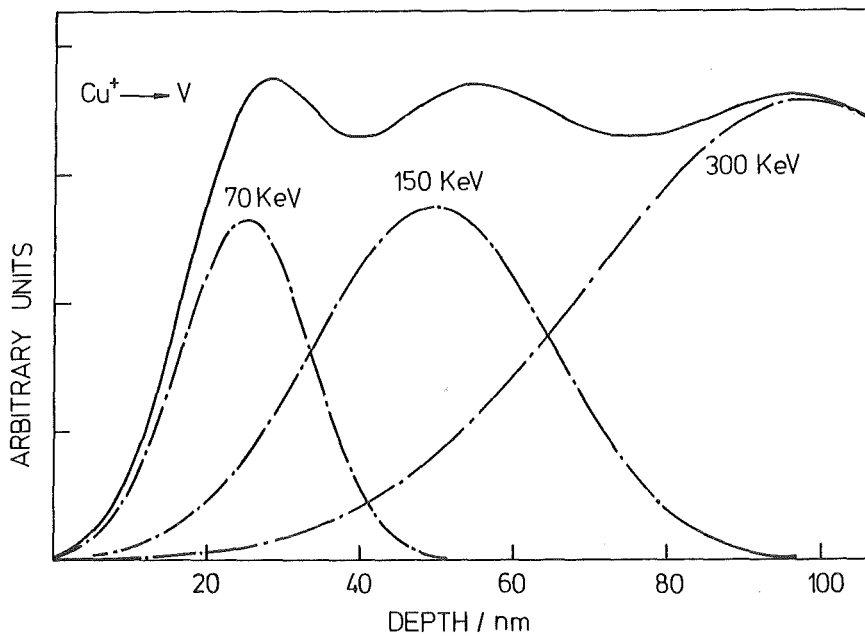
Fig. 12: Calculated implantation profile using three energy values for Cu in V in a depth region of 1000 Å.

For a Cu concentration value of 4 at.% the f_s-value is
about 0.7 ± 0.1. With increasing Cu concentration f_s decreases
as can be seen in Table 2. This can be attributed to precipita-
tion of Cu atoms.The substitutional concentration achieved after
implantation of 20 at.% Cu is 9 at.% (see Table 2) which is
somewhat higher than the equilibrium solid solubility limit
(7 at.%) /65/ .

Table 2 *Substitutional fraction (f_s) for Cu-implanted V single crystals*
as measured at different Cu-concentrations. The implantation
and measurements are carried out at 300 K.

Concentration of Cu at.%	f_s (± 0.1)	Substitutional Concentration at.%
4	0.70	2.8
10	0.55	5.5
15	0.50	7.5
20	0.45	9.0

As an example the angular scan measurements through the <111>
axial direction are presented in Fig. 13 for Cu implanted into
V to a peak concentration of about 10 at.%. The values of
(χ_{min}) and $\psi_{1/2}$ for Cu and V are shown in the figure. A narrowing
of the scan curve for Cu shows that the Cu atoms are not
located on a perfect substitutional lattice sites but are
slightly displaced. This displacement could be attributed to
/63/ coherent precipitation of Cu atoms or formation of some
Cu-vacancy complex.

VAu: Au atoms occupy substitutional lattice sites in vanadium
single crystals after implantation at 300 K with concentrations
between 0.08 and 0.60 at.%. The evaluation of large reduction
in the scattering yield from the Au atoms in the aligned spectrum

relative to that of the random one shows that 100% of the
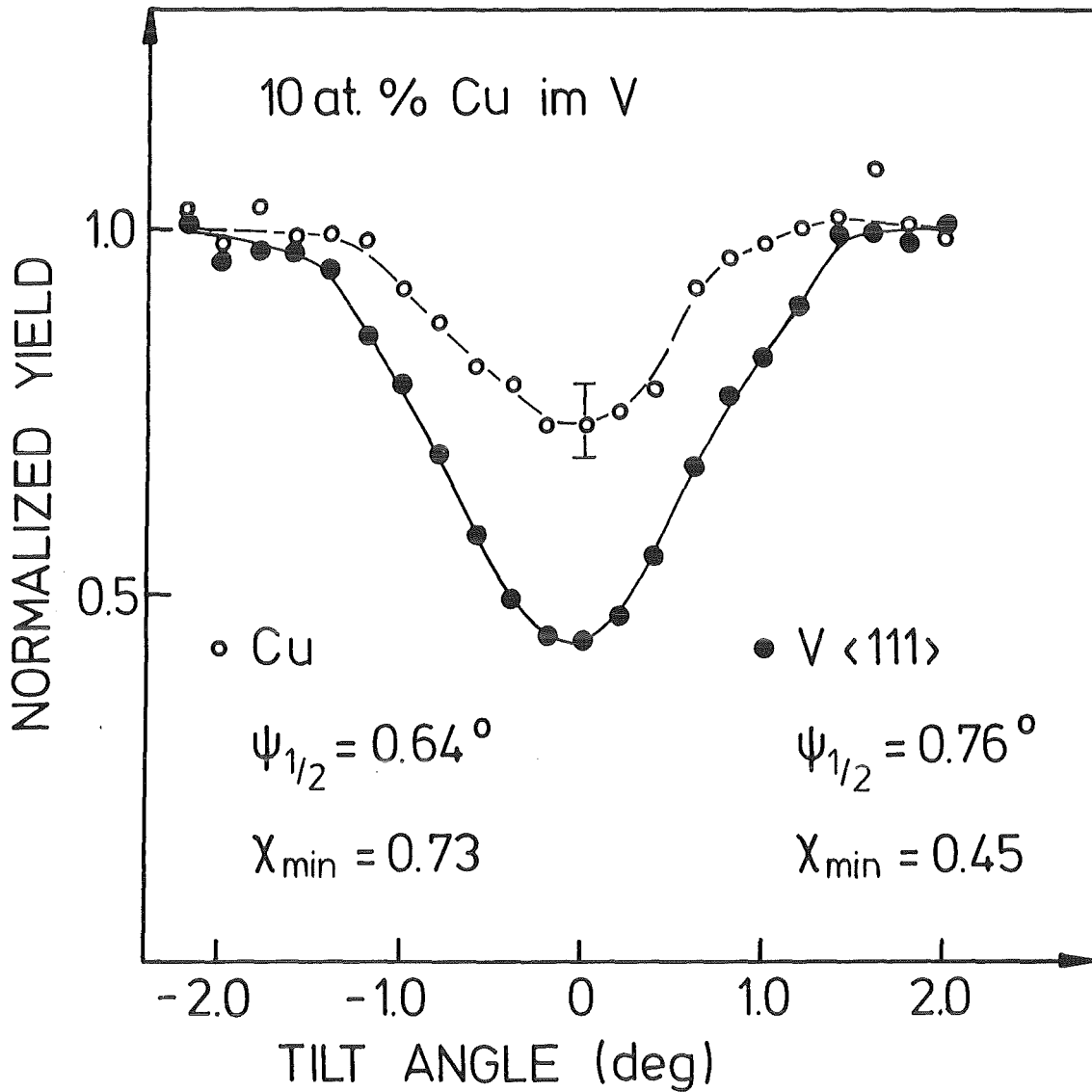implanted Au atoms are located on substitutional lattice
sites.

Fig. 13: Angular yield curves through the <111> axial direction
from a Cu implanted V single crystal. The Cu-concentration
is about 10 at.%.

4.2.2 VSn and VPb

VSn: Sn ions are implanted at 300 K in vanadium single
crystals for a wide concentration range between 0.03 and 21 at.%.
The ion energy used is 300 keV with fluence of 2.2 x 10^{15} ion/cm^2
corresponding to a concentration value of 1 at.%. Random and
<111> aligned backscattering spectra are measured to determine
the substitutional fraction for each concentration. Fig. 14 shows
as an example these spectra for 0.33 at.% Sn implanted vanadium
single crystal. For comparison the <111> aligned spectrum of the
unimplanted sample is included. It is clearly seen by comparing
the Sn peak areas of the random and aligned spectra that the
Sn atoms are highly substitutional in V.

Dechanneling corresponding to the damage produced in the
crystal is seen to be extended to a large depth (2600 Å). This
depth is far larger than the mean projected range of the implan-
ted Sn ions (600 Å). This result can be attributed to accumula-
tion of mobile point defects, which are produced by the implan-
tation. The defect clusters affect the channeled beam trajectory
and produce dechanneling which extend to large depth behind the
projected range. It is also noticed that the implanted ion profile
depends strongly on the orientation of the sample during the
implantation. Nearly channeled ions come more deeper in the cry-
stal than the mean projected range.

A disorder peak in the implanted region is observed for Sn
concentrations higher than 4 at.% (for example see Fig. 15)
at a depth corresponding to the maximum Sn concentration. This
direct backscattering peak is probably due to a higher disorder
or amorphization of a part of the implanted volume. It has been
shown previously that strain fields in ion implanted metals
may cause a crystalline to amorphous phase transition /66/.
Increasing the Sn concentration is followed by an increase of
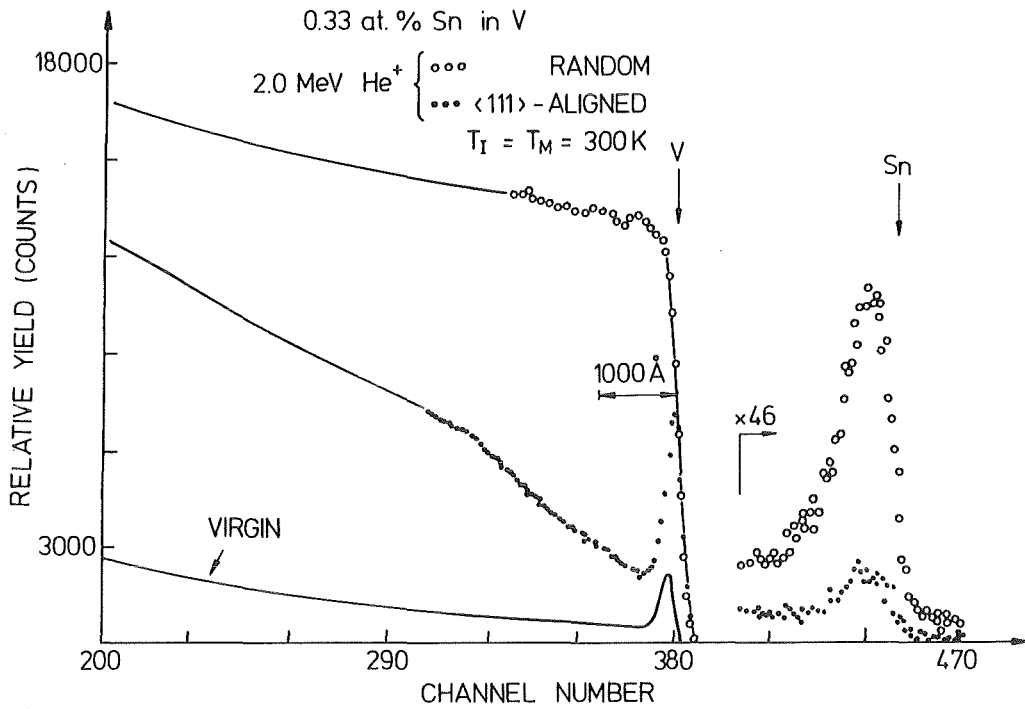the height of this disorder peak reaching the random level at
21 at.%.

Fig. 14 Random and <111> aligned spectra from a 0.33 at.% Sn implanted
V single crystal. The <111>-aligned spectrum before the implan-
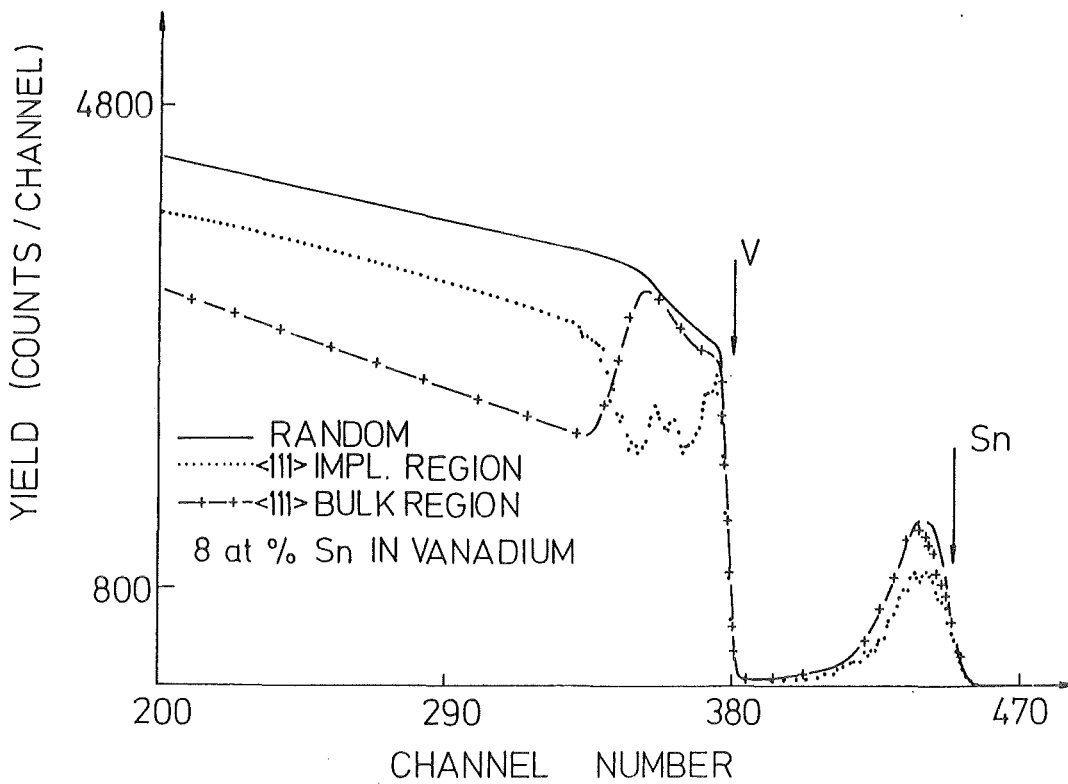tation is also seen in the Figure.

Fig. 15: Random and <111> aligned spectra for 8 at.% Sn implanted V single
crystal. The <111> aligned spectra are measured relative to the
implanted (...)and bulk region (-x-) orientation, respectively.

Plastic deformation of the implanted region (which is first observed for the system $\underline{V}$As /67/) is observed for Sn concentrations higher than 8 at.%, and is demonstrated in Fig. 15 /68/. It should be noted that completely different structures are obtained for the spectra either aligned to the bulk or to the implanted region. The measured angle between the different orientations is about 1.1°.

The substitutional fraction (f_s) as a function of Sn concentration is summarized in table 3. It can be noted that f_s is equal to 1.0 independent of the Sn concentration. In order to determine the lattice site occupied by the Sn atoms more exactly angular yield curves are measured for all concentration values. Fig. 16 shows the angular dependence of the normalized yields from V and Sn atoms as measured through <111> axial direction for a 4 at.% Sn implanted V sample. The scans show identical angular dependence for the implanted Sn and the host V atoms indicating that 100% of Sn atoms occupy substitutional lattice sites without relaxation.

Table 3 *Substitutional fraction (f_s) as a function of the Sn-concentration*

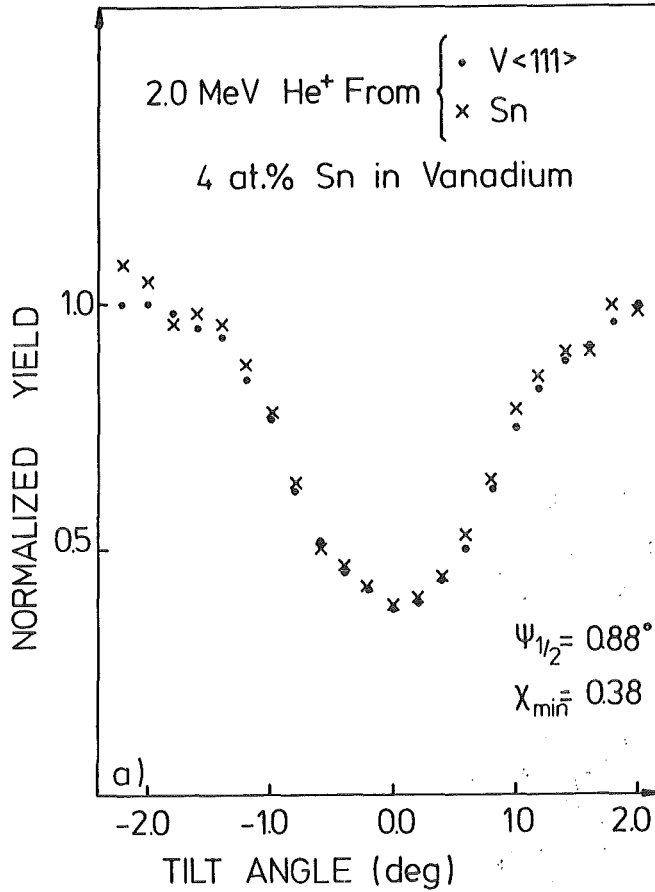| Sn-Concentration at.%	f_s		
0.03	1.0	±	0.08
0.15	1.0		
0.33	1.0		
3.90	1.0		
8.0	1.0	±	0.05
9.0	1.0		
11.0	1.0		
12.0	1.0		

Fig. 16:
Angular yield curves through the <111>-axial direction from Sn-atoms (x) and V atoms (.). The values of χ_{min} and $\psi_{1/2}$ are inserted.

VPb: Pb atoms occupy substitutional lattice sites in vanadium single crystals after implantation at 300 K with concentrations between 0.10 and 0.60 at.%. Fig. 17 shows as an example random and <111> aligned spectra for a vanadium single crystal implanted with Pb ions of 300 keV and a peak concentration of 0.52 at.%. The evaluation of the large reduction in the scattering yield from the Pb atoms in the aligned spectrum relative to that of the random one shows that 100% of the implanted Pb atoms occupy substitutional lattice sites.
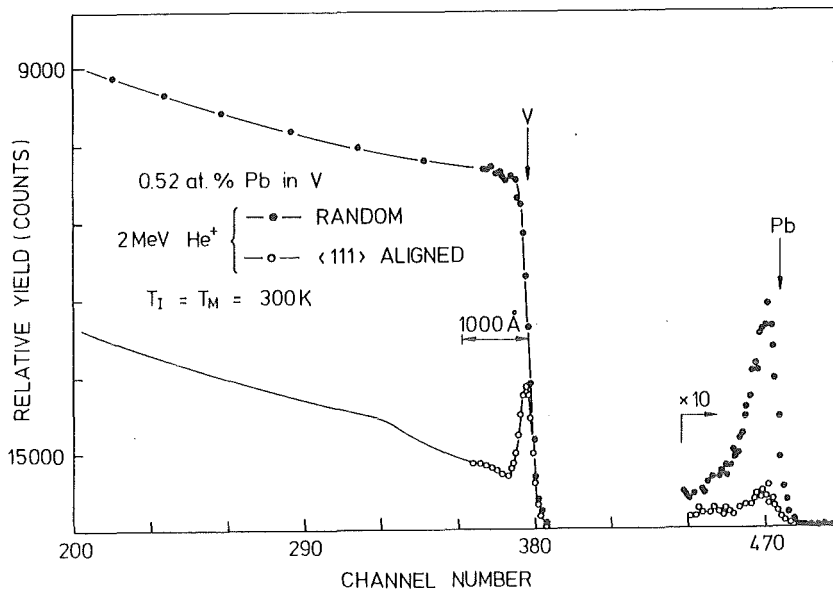
Fig. 17: Random and <111> aligned backscattering spectra from a V crystal implanted with 0.52 at.% Pb. Implantation and measurements are carried out at 300 K.

4.2.3   VAs and VBi

VAs: Vanadium single crystals are homogeneously implanted at 300 K with As ions over a depth of about 1200 Å using four different energy values of 60, 120, 200 and 300 keV with the corresponding fluences of 7.9 x 10^{14}, 1.3 x 10^{15}, 1.3 x 10^{15}, 3.6 x 10^{15} ions/cm^2, respectively for 1 at.% As. The As concentration values are varied over a wide range between 0.5 and 22 at.%. Random and <111> aligned backscattering spectra have been measured as a function of the implanted As concentration. One example of such spectra is presented in Fig. 18 for an As concentration value of 5 at.%. Helium ions backscattered from arsenic atoms are seen to be well separated in energy from those backscattered from vanadium atoms. The reduction of the backscattering yield from As and V in the aligned spectrum, relative to those in the random spectrum, indicates that As atoms are highly substitutional in V. It is noticed that no equilibrium solid solubility has been listed to the system VAs. The relatively low minimum yield for the vanadium crystal in the implanted region
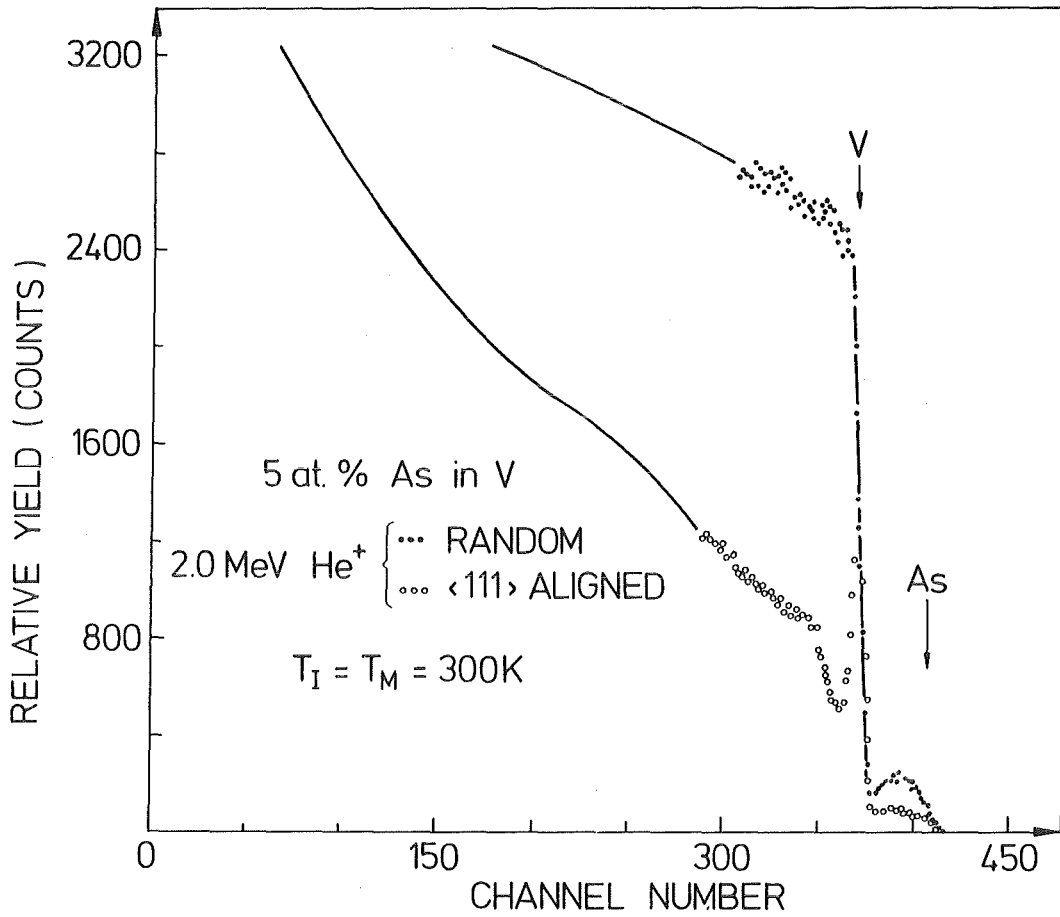
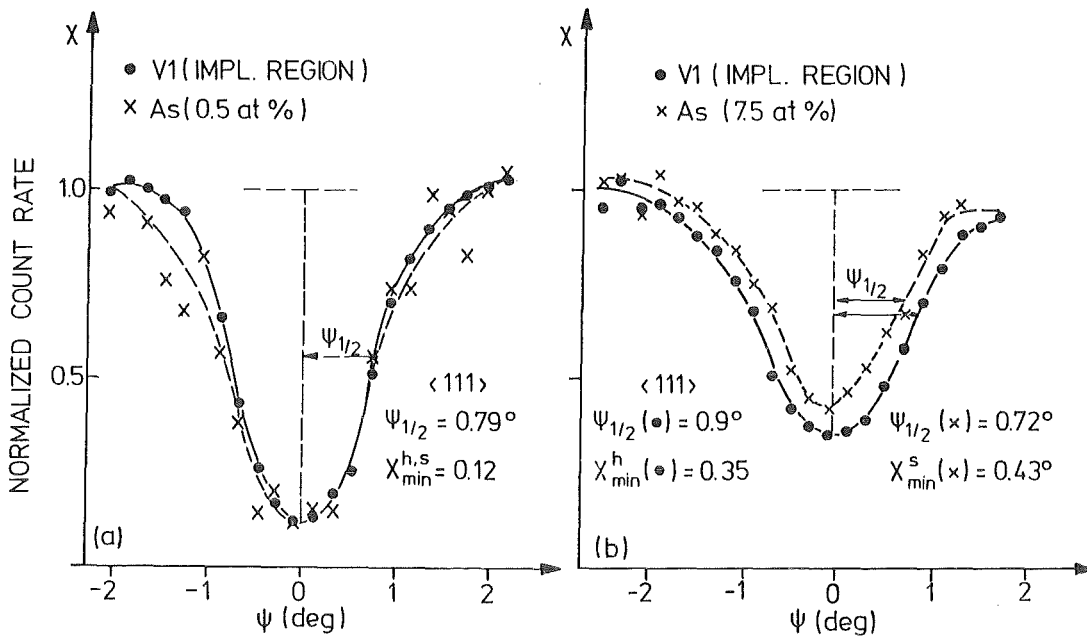Fig. 18: Random and <111> aligned backscattering spectra from a V sample implanted with 5 at.% As (T_I=T_M=300 K).

Fig. 19: Angular yield curves through the <111> axial direction from a V single crystal implanted with As ions at 300 K.

a.   0.5 at.% As;   b. 7.5 at.% As

is attributed to radiation induced damage annealing by recombi-
nation of point defects within the dynamical cascade and by
thermal annealing of point defects at stage I, II and III. The
high dechanneling rate in the aligned spectrum may be attri-
buted to agglomerates formed by mobile point defects at 300 K.
Detailed angular scans are measured for all As-concentrations.
Fig. 19 show examples for these measurements at 0.5 and 7.5 at.%.
For 0.5 at.% As (Fig. 19a) the same minimum yield (χ_{min}) and cri-
tical angle ($\psi_{1/2}$) measured for As and V atoms indicate that
all As atoms occupy substitutional lattice sites without rela-
xation. For 7.5 at.% (Fig.19b) the critical angle is smaller
and the minimum yield is larger for As atoms than the correspon-
ding values for the V host atoms, indicating that As atoms are
no longer located on a perfect substitutional sites but are
somewhat displaced. The substitutional fraction at different As-
concentrations are summarized in Table 4. f_s is 1.0 at low con-
centrations and decreases to 0.7 at higher concentrations. The
angular scans through the <110> axial direction show the same
substitutional fraction (f_s = 0.75) for 17 at.%. As. A maximum
substitutional concentration of about 15 at.% is achieved after
implantation of 21.5 at.% As (see Table 4).

Table 4   _Substitutional fraction (f_s) for As-implanted V single crystals as
measured through the <111>-axial direction at different As-concen-
trations. The implantation and measurements are carried out at 300 K._

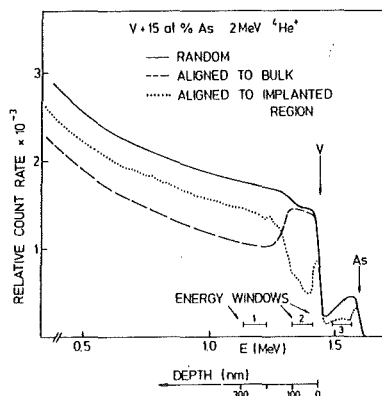| Concentration of As at.%	$f_s \pm 0.05$	Substitutional Con- centration at.%
0.5	1.0	0.5
5.0	0.85	4.3
7.5	0.87	6.5
9.5	0.85	8.1
14.5	0.75	10.9
15.5	0.80	12.4
19.0	0.75	14.3
21.5	0.70	14.7

Fig. 20: Typical channeling and backscattering energy spectra for a high-dose (15 at.%) arsenic implanted in a vanadium single crystals. <111>-aligned spectra are shown for axial alignment within the implanted region (dotted curve) and for axial alignment within the bulk (dashed curve).

At arsenic concentrations higher than 14 at.%, a plastic deformation of the implanted region is observed /67/. There, the crystal planes in the implanted region start to rotate with respect to the original bulk crystal direction. Completely different backscattering spectra are measured at 15 at.% As after axial alignment with the implanted region and the bulk region, respectively (see Fig. 20). The effect is probably caused by misfit strain fields around the As atoms which activate a slip system with a <111> slip direction and with (111) or (211) slip planes.

A further increase of the As concentration leads to polygonization of the implanted layer. A similar effect is observed previously for the system VGa after annealing up to 700°C /68/.

VBi: Bi atoms are observed to occupy substitutional lattice sites if implanted into V single crystals at 300 K up to a concentration of about 4 at.% /59,63/. As an example for the elements which are substitutional after implantation into V at 300 K, Bi is choosen in this work to be studied in situ after
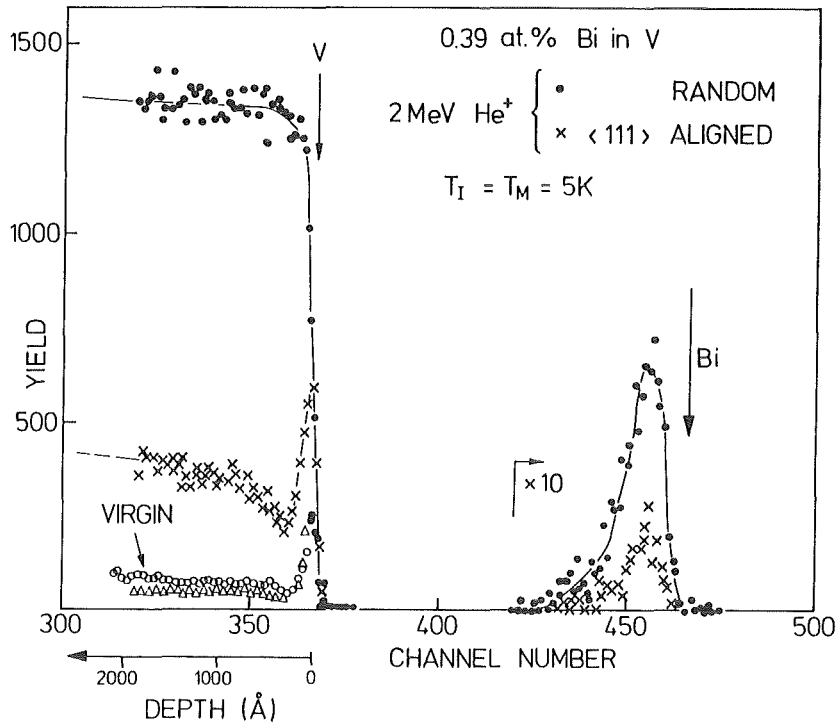
Fig. 21: Random and <111> aligned spectra from a V sample implanted with
0.39 at.% Bi at 5 K. The <111> aligned spectra taken at 300 K
and 5 K prior to implantation are also shown.

implantation at 5 K, where the point defects are not mobile.
As an example Fig. 21 shows random and <111> aligned spectra
from a vanadium sample implanted with 0.39 at.% Bi /72/. The
evaluation of the large reduction in the scattering yield of
the Bi atoms in the aligned spectrum relative to that in the
random one shows that Bi atoms have a rather high substitutio-
nal fraction (f_s = 1). This result is also seen from the angu-
lar yield curved in Fig. 22, where a perfect matching of the
scan curves of Bi and V clearly shows that all Bi atoms occupy
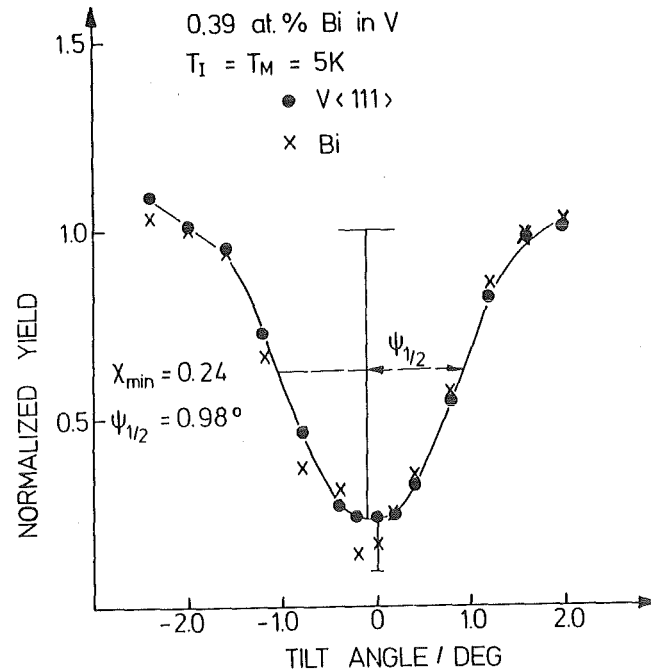substitutional lattice sites without relaxation. Upon warming

Fig. 22: Angular yield curves through <111>-axial direction from a Bi implanted vanadium single crystal.

the sample to 300 K, the substitutional fraction is seen to be constant, where the damage profile in the host lattice slightly changed indicating clustering of point defects. The last result indicates that the mobility of the point defects do not affect the lattice positions of the substitutional Bi atoms.

4.2.4 VSe, VTe and VI

VSe: The VSe system was studied by /63/ at a Se concentration value of 4 at.%. The substitutional fractions (f_s) were 0.76 and 0.70 in the <111> and <110> axial direction, respectively. A narrowing of the scan curves for Se was measured in comparison with the vanadium host lattice. The deviation of the
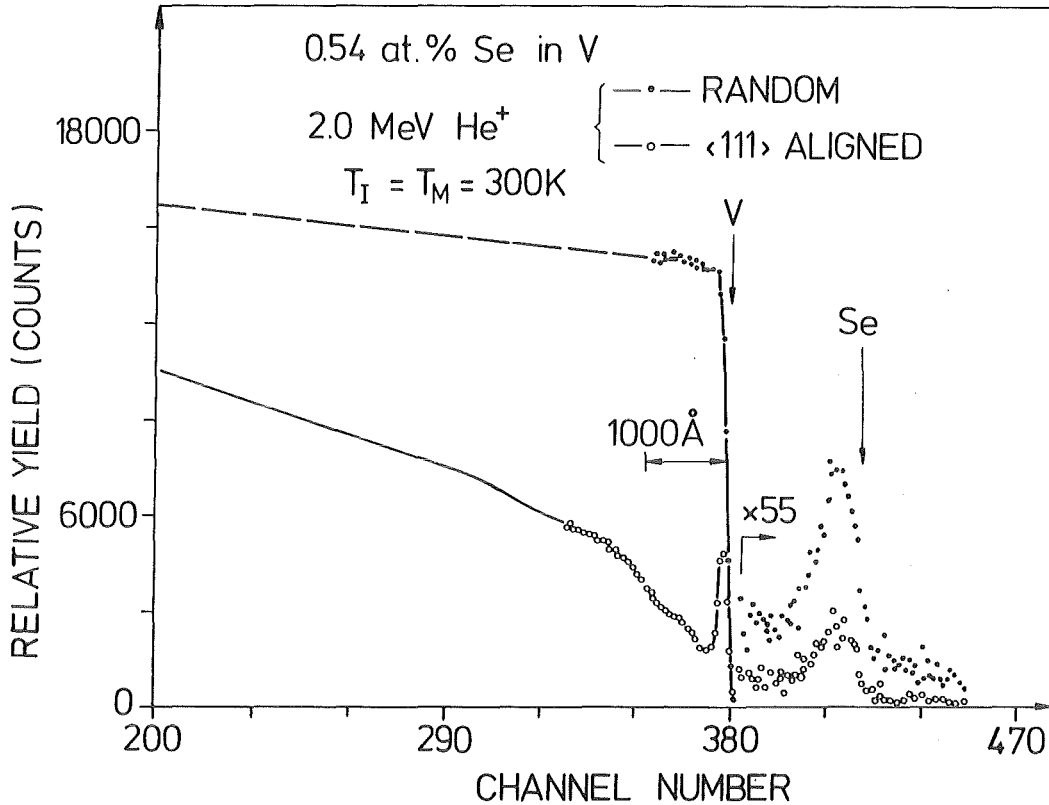
Fig. 23: Random and aligned backscattering spectra from a Se implanted vanadium single crystal. The implantation and analysis are performed at 300 K.

$\psi_{1/2}$ value of Se from those of the host lattice was twice for the <110> axial direction. This indicates that the average displacement amplitude of Se atoms from the perfect lattice position is preferentially oriented parallel to the <110> directions. In the present work, Se ions are implanted at 300 K into vanadium single crystals with concentrations between 0.13 and 24 at.%. The Se ions energy is 300 keV with fluences of 3.7 x 10^{15} ion/cm^2 corresponding to a concentration value of 1 at.%. Random and <111> aligned backscattering spectra are shown for 0.54 at.% Se, in Fig. 23.

The substitutional fraction, f_s, is equal to 1.0 at 0.13 at.% Se and then decreases with increasing Se concentrations

(see Table 5) to the same value measured previously. The criti-
cal angle $\psi_{1/2}$ for Se atoms is difficult to determine at 0.13 at.%
because of   the low backscattering yield. At higher concentra-
tions between 0.54 and 10 at.%, narrowing of the angular scans
has been measured as listed in Table 5 in accordance with that
measured by /53/.   The decrease of f_s-values at concentrations
higher than 10 at.% are accompanied by an increase of the critical
angle $\psi_{1/2}$ for Se atoms in the scan curves. Values greater than
one are measured for the ratio $\psi_{1/2}(Se)/\psi_{1/2}(V)$ (Table 5).
This unusual behaviour can be attributed to coherent precipita-
tion of Se forming rows of atoms which are suitable for channe-
ling. Such an effect has been studied previously for coherent
precipitation in MgO /72/.

Table 5   *Substitutional fraction values (f_s) for Se implanted V single
crystals as measured through <111> axial direction at different Se-
concentrations. The values of critical angle for Se atoms in the
scan curves relative to those of V host lattice are also seen in the
table.*

Concentration of Se	$f_s \pm 0.05$	$\psi_{1/2}(Se)/\psi_{1/2}(V)$
0.13	1.0	–
0.54	0.80	0.81
3.70	0.70	0.80
5.0	0.70	0.76
9.0	0.70	0.76
10.0	0.68	0.80
14.0	0.62	1.20
24.0	0.41	1.20

VTe: The system VTe is studied after implantation of 300 keV
Te ions in vanadium single crystals at 300 K. The substitutio-
nal fraction is equal to 1.0 for different Te concentrations
(Table 6) between 0.04 and 8 at.%. Increasing the Te concentra-
tion to 11 at.%, is accompanied by a decrease of the substitu-
tional fraction to a value of about 0.66.

Table 6 *Dependence of substitutional fraction (f_s) for Te atoms, as measured through <111>-axial directions of vanadium single crystal, on the implanted Te-concentration $(E_o = 300$ keV, $T_I = T_M = 300$ K).*

Te-concentration at.%	f_s
0.04	1.0+0.1
0.37	1.0
1.70	1.0
4.20	1.0
5.70	1.0 $\pm$ 0.05
7.20	1.0
11.0	0.66

The exact position of Te atoms can be determined from the angular scans (Fig. 24). For Te concentrations lower than 8 at.%, the normalized backscattering yield from Te and V atoms reveal an identical angular dependence (Fig. 24 a,b) which shows con- clusively that about 100% of the implanted Te atoms occupy substitutional lattice sites without relaxations. At higher concentrations, the minimum yield and the critical angle (χ_{min}, $\psi_{1/2}$) for Te atoms are larger than the corresponding value for V host atoms (Fig. 24c). The last result could be attributed to coherent Te atom precipitation.

Plastic deformation of the implanted region is also ob- served for the system at Te concentrations higher than 8 at.% /68/.

VI: The lattice location of I atoms, as an example for halogens, in V is studied after implantation of I ions at 300 K to a concentration range between 0.03 and 4.5 at.%. The ions energy used is 300 keV with the corresponding projected range of 555 $\pm$ 124 Å. The angular yield curves for V and I atoms are measured for different concentration values. Results are shown for example in Fig. 25 a,b for 0.13 and 4.5 at.%, respectively.
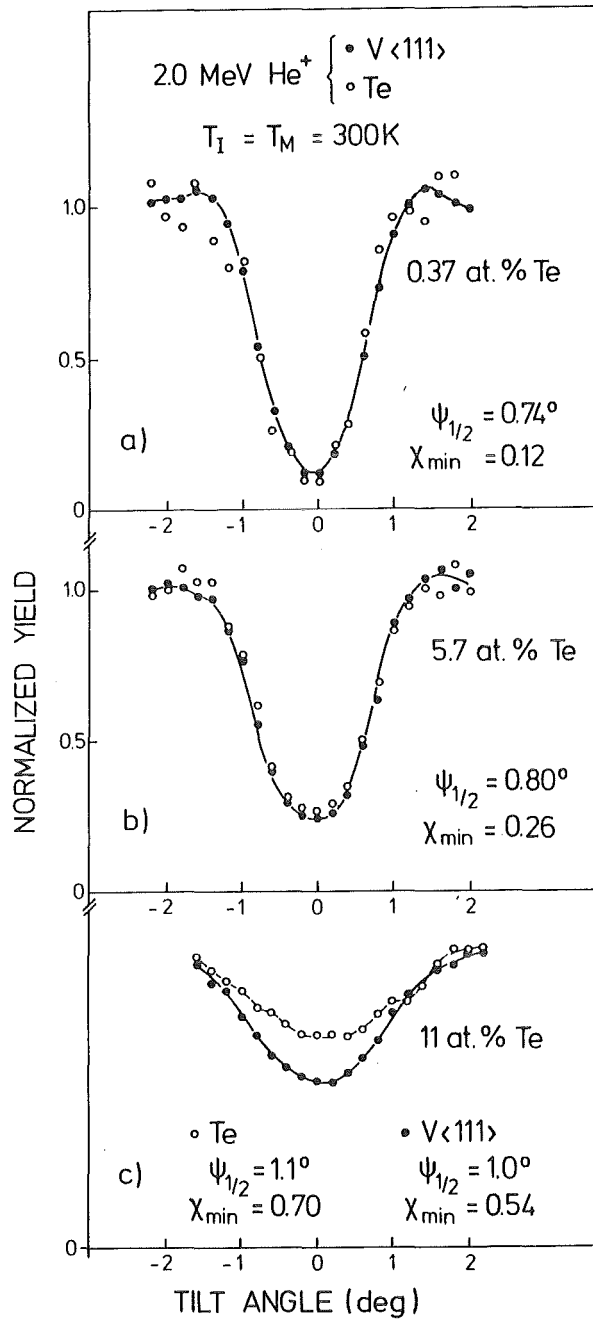
Fig. 24: Angular yield curves through the <111> axial direction of Te implanted V single crystals with different Te concentration values as indicated (E_o = 300 keV, T_I = T_M = 300 K).
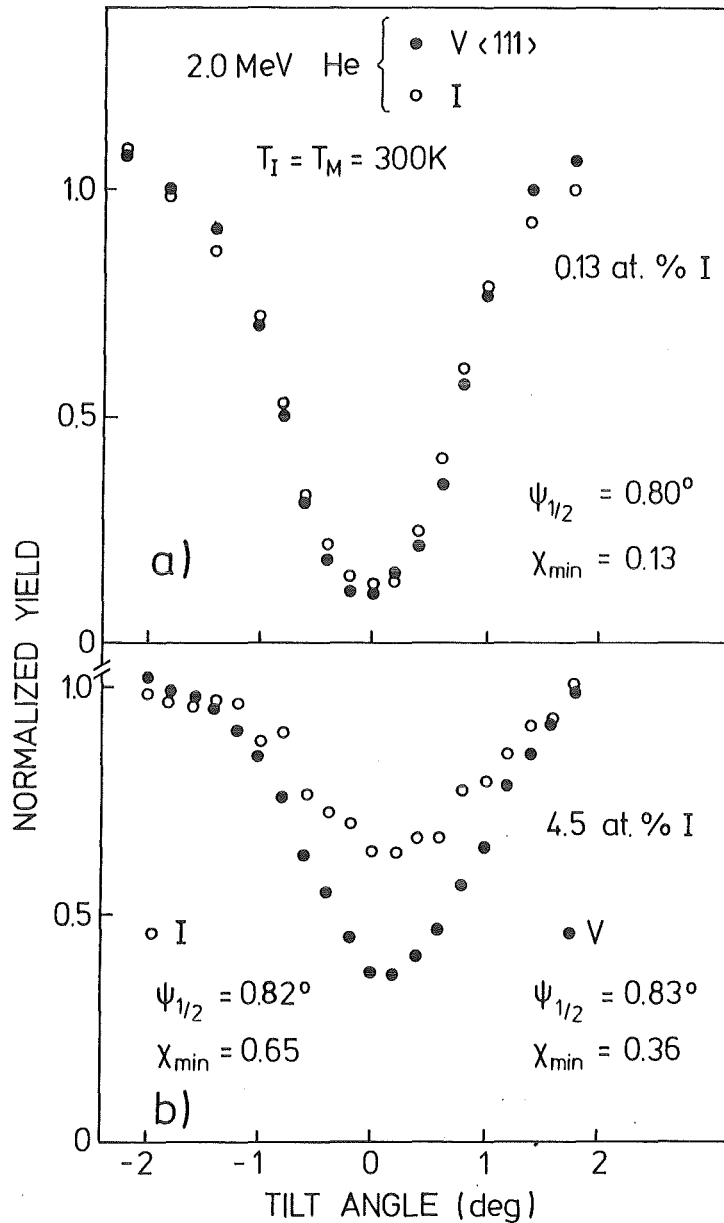
Fig. 25: Angular yield curves through the <111>-axial direction of I
implanted V single crystals.

From angular scans measured at low concentrations, it is con-
cluded that all I atoms occupy regular lattice sites. The sub-
stitutional fraction of I atoms decreases at high concentra-
tions and reaches a value of 0.55 at 4.5 at.% (Fig. 25b). The
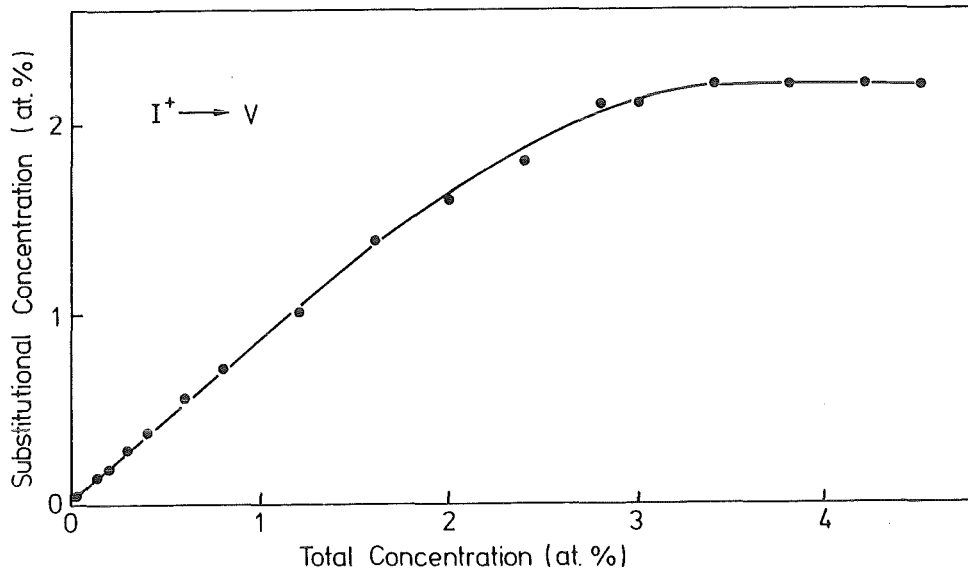critical angle $\psi_{1/2}$ of the I atoms is equal to that of V host

Fig. 26: Substitutional concentration of I atoms as a function of the total implanted concentration, $T_I = T_M = 300$ K.

atoms. The results may be attributed to incoherent precipitation of I atoms.

Fig. 26 shows the substitutional I concentration as a function of the total implanted concentration. While no equilibrium solid solubility is listed for I in V the substitutional concentration is seen to increase linearly up to a maximum value of about 2.2 at.% giving the maximum solid solubility of I in V produced by ion implantation at 300 K. A low solid solubility limit (1.0 at.%) was also measured after implantation of I in Cu at 300 K /71/.

4.3 Partially Substitutional Implanted Systems
4.3.1 VKr and VXe

VKr: 280 keV Kr ions are implanted at 300 K in V single crystals at a rather low concentration value of 0.12 at.%. Random and <111> aligned backscattering spectra are shown in Fig. 27. He-ions with an energy of 3 MeV have been used in order to improve the mass resolution. While the oriented backscatte-
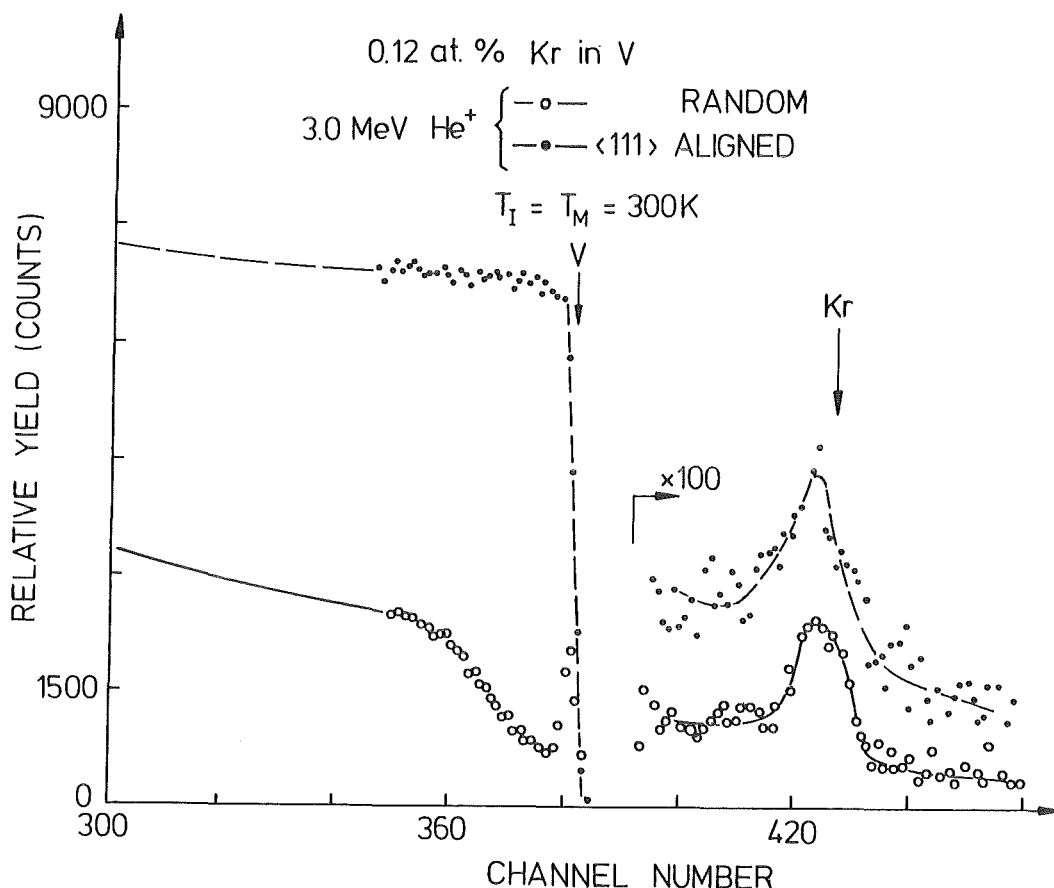
Fig. 27: Random and <111>-aligned backscattering spectra from a Kr implanted vanadium single crystal (0.12 at.% Kr). The implantation and measurements are performed at 300 K.

ring yield from V host atoms in the implanted region is seen to be relatively low, the areas of Kr-peak (after background correction) in the random and aligned spectra are seen to be equal.

The substitutional fraction (f_s) at this rather low concentration is 0.12 ± 0.1, in accordance with earlier measurements at higher concentration, 3.2 at.% /69/. The non-substitutional lattice site occupied by Kr atoms in V could be attributed to formation of Kr-bubles, by thermal diffusion, which is favourable for inert gases. It is thought that, if Kr ions would be implanted at 5 K, where no diffusion takes place, such bubbles could not be formed. Such experiments are performed in this work for the inert gas, Xe, having a higher atomic number and therefore a higher backscattering yield than Kr.

VXe: Xe ions are implanted in V single crystals and analyzed in-situ at 5 K and 300 K. The ions energy is 300 keV with the corresponding projected range of 548±120 Å. A substitutional component (47%) is measured for low Xe concentration value after implantation at 300 K. This component decreased with increasing Xe concentrations as summarized in Table 7. The angular scans for 0.34 at.% Xe is narrower than that of V host atoms (Fig. 28a) which could be attributed to a relatively large displacement of Xe atoms from the exact lattice sites. It is noticed that the displacement amplitude of Xe atom for cancy complex in Fe is equal to 1/4 the next neighbour distance /72/. The substitutional component increases to about 57% for samples implanted and analyzed in situ at 5 K. The ratio of critical angle ($\psi_{1/2}$) for the Xe atoms to that for the V host atoms is smaller than 1.0 but larger than that measured at 300 K (Fig. 28b). The last result indicates that Xe atoms are still displaced from the exact lattice sites even after implantation at 5 K, however, the mean displacement amplitude is smaller than that for a sample implanted at 300 K. Warming up the sample to 300 K, is followed by a decrease of the substitutional component (38%) as well as the critical angle ratio $[\psi_{1/2}(Xe)/\psi_{1/2}(V)]$. It is clearly seen that the lattice position occupied by Xe atoms in V after implantation at 5 K followed by warming up to 300 K (Fig. 28c) are nearly similar to those occupied by direct implantation at 300 K. This effect could be attributed to the interaction between Xe atoms and mobile point defects in the delayed regime of the collisional cascade.

It should be noted that the point defects produced by the analyzing ion beam are immobile at 5 K but they become mobile and may interact with the impurity atoms if the sample is warmed up to 300 K. The concentration of these point defects which depends on the analyzing ion beam fluence is an important factor determining the decrease of both f_s and $\psi_{1/2}$ of the implanted impurities upon worming up a sample from 5 K to 300 K.
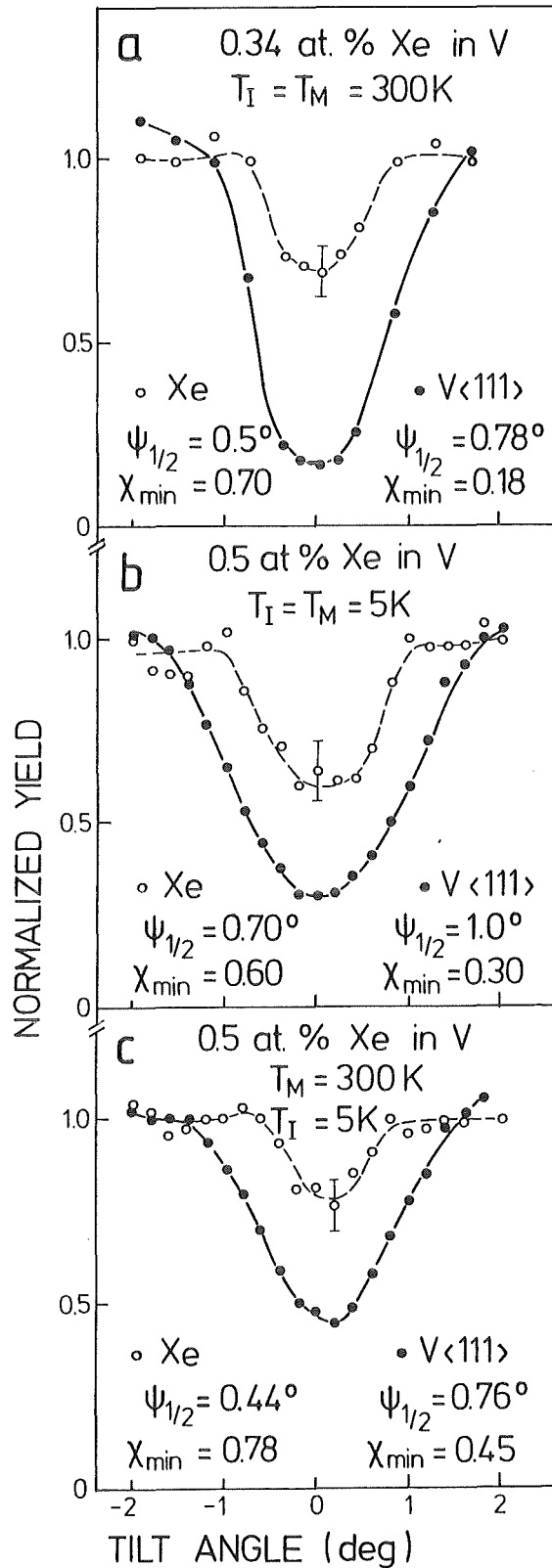
Fig. 28: Angular yield curves through the <111>-axial direction for Xe implanted V single crystals. The samples are implanted and analyzed at 300 K (a), at 5 K (b) and are implanted at 5 K and analyzed at 300 K (c).

Table 7 *Substitutional fraction f_s for Xe implanted into V single crystals as a function of the Xe concentration, the implantation and the analysis temperature (T_I, T_M).*

Xe-concentration	T_I/K	T_M/K	$f_s \pm 0.05$
0,15			0.47
0,34	300	300	0.37
2,2			0.0
0,5	5	5	0.57
0,5	5	300	0.38

4.3.2 $\underline{V}$Cs and $\underline{V}$Ba

$\underline{V}$Cs: Cs ions are implanted in V single crystals at 300, 77 and 5 K to different concentration values. The substitutional fractions are measured in situ through the <111> and <110> crystal directions and after annealing from low temperatures up to 300 K /73/. After implantation at 300 K, the substitutional fraction is independent of the crystal direction and of the Cs concentration between 0.02 and 0.5 at.%. As an example random and <110> aligned spectra of a V single crystal implanted with 0.5 at.% Cs are shown (Fig. 29). The normalized minimum yield for Cs atoms is higher than that of the V host atoms, leading to a substitutional fraction of 0.14 ± 0.08, in agreement with previous measurements /59/.

At 77 K, where vacancies are not mobile, the substitutional fraction is found to be 0.40 ± 0.1 independent of the Cs concentration between 0.09 and 0.5 at.%. At higher concentration values, f_s, decreases and reaches 0.0 at about 3.0 at.% Cs (see Table 8). Warming up to 300 K a sample which is implanted with 0.21 at.% Cs at 77 K , f_s decreases from 0.5± 0.05 to 0.20 ± 0.05. This effect is demonstrated in Figs. 31a and 31b, where the angular scans measured for this sample at 77 K and at 300 K are compared. Also in this case ,and in general , the
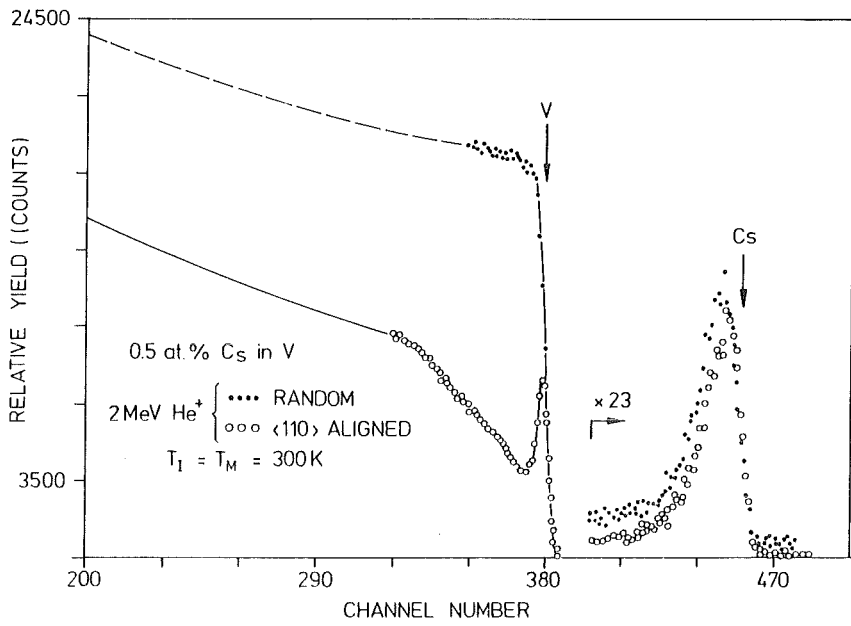
Fig. 29: Random and <111> aligned spectra of a V single crystal implanted with 0.5 at.% Cs. Implantations and measurements are carried out at 300 K . The implanted ion energy is 300 keV.
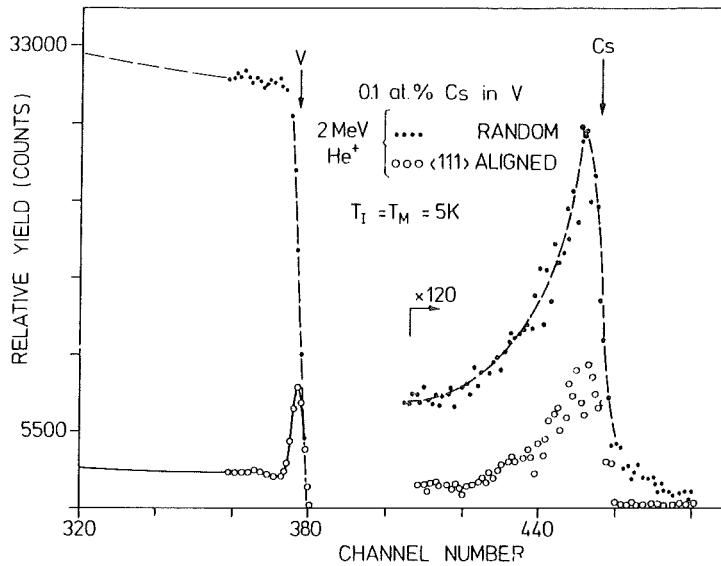

Fig. 30: Random and <111>-aligned spectra of a V single crystal implanted with 0.10 at.% Cs. Implantations and in situ measurements are carried out at 5 K . The implanted ion energy is 300 keV.

Table 8 Dependence of the substitutional fraction, f_s, on the concentration values of Cs atoms implanted into V single crystals. $T_I = T_M = 77$ K.

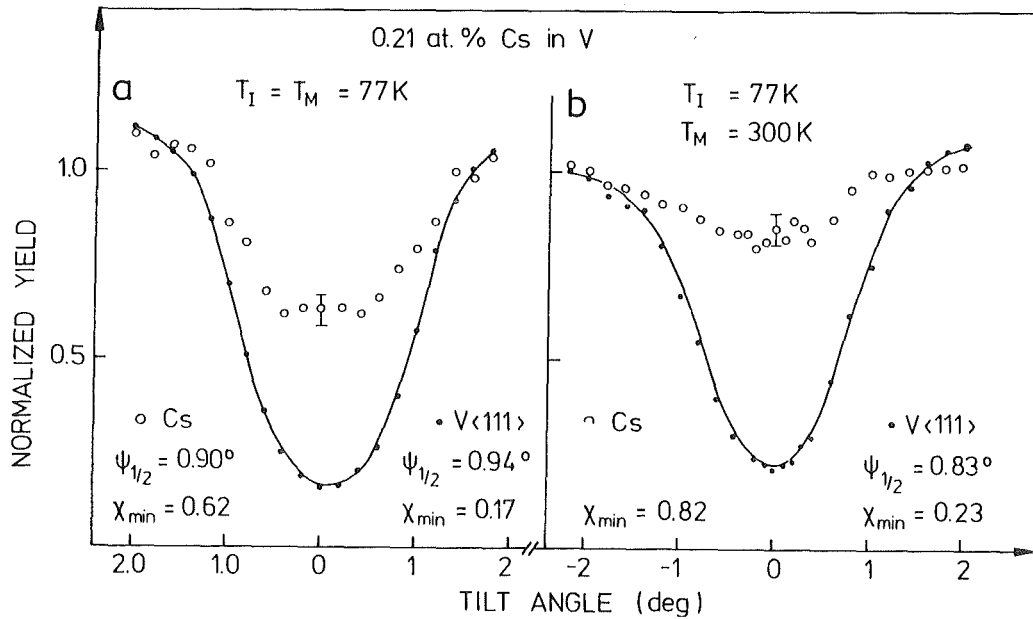| Cs-concentration at.%	f_s <111>
0.09	0.50 ± 0.1
0.094	0.50 ± 0.1
0.11	0.38 ± 0.05
0.12	0.36 ± 0.05
0.15	0.38 ± 0.05
0.16	0.50 ± 0.08
0.21	0.50 ± 0.05
0.49	0.38 ± 0.05
0.85	0.30 ± 0.05
3.0	0.0

Fig. 31: Angular scans from Cs and V-atoms for 0.21 at.% Cs implanted V sample. (a) as-implanted at 77 K (b) after annealing up to 300 K.

value of f_s after annealing to 300 K depends strongly on the concentration of the point defects produced by the analyzing beam as described befor in chapter 4.3.1 . Upon annealing in vacuum up to 100 ^{O}c , f_s decreases to 0.0 for all samples implanted at 77 K.

At 5 K where the point defects are not mobile, the measured substitutional fraction for Cs atoms is about 0.65 at low concentration values. Fig. 32 shows an example of random and <111> aligned spectra for 0.10 at.% Cs. The implantations and in situ measurements are carried out at 5 K (T_I = T_M = 5 K). The substitutional fractions measured through the <111> and the <110> axial directions are summarized in Table 9.

Table 9 *Dependence of substitutional fraction, f_s, on the concentration of Cs implanted in V (T_I = T_M = 5 K).*

Cs-concentration	f_s	
	<111>	<110>
0.10	0.65 + 0.08	
0.22	0.65 + 0.08	
0.29	0.52 + 0.05	
0.20		0.57 + 0.08
0.90		0.34 + 0.05
7.0		0.0

Similar critical angles $\psi_{1/2}$ for Cs and V atoms in the angular yield curves (example Fig. 32) indicate that Cs atoms occupy substitutional lattice sites without relaxation.

The non-substitutional components of Cs atoms can be attributed to Cs-vacancy associations formed within the dynamic cascade or by trapping mobile vacancies in the delayed regime. Mobile interstitials are thought to annihilate impurity-vacancy complexes /74/ during irradiation with light ions at temperatures below the
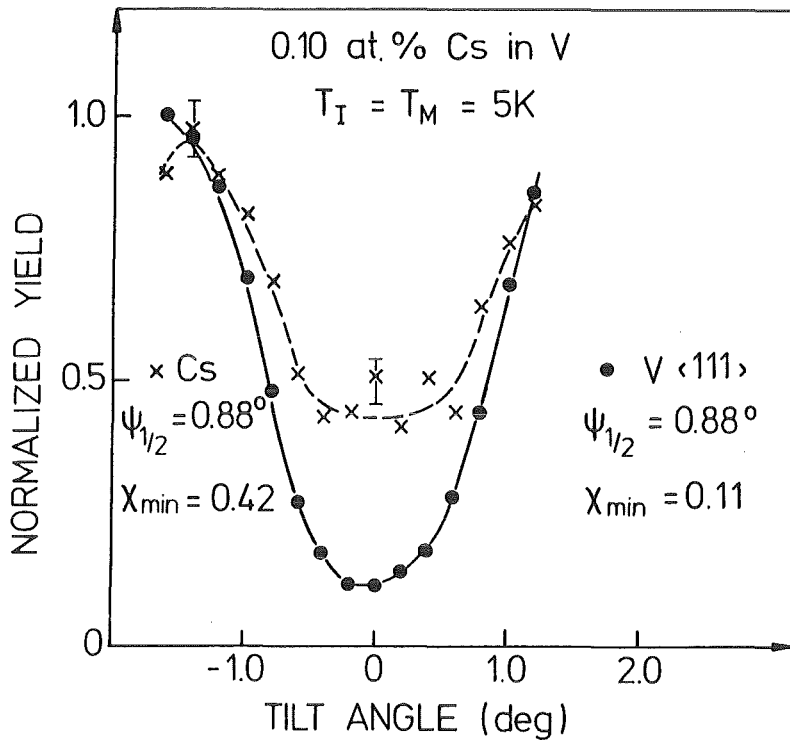
Fig. 32: Angular yield curves from Cs- and V-atoms measured in situ at 5 K.

vacancy annealing temperature. Therefore postirradiation experiments using 300 keV He ions at 77 K are performed for samples implanted at 5, 77 and 300 K, respectively. No change of the substitutional fraction is observed upon irradiation up to He ion fluences of 2×10^{16} ion/cm^2. Warming up these samples to 300 K, the substitutional fraction decrease to 0.3 and 0.2 for samples implanted at 5 and 77 K, respectively. This last result can be attributed to trapping of mobile vacancies at stage III forming Cs-vacancy complexes.

Plastic deformation of the implanted region is observed upon implantation of 3 at.% Cs in V at 77 K /68/.

VBa: Ba ions do not occupy substitutional lattice sites even at rather low concentrations if implanted in V single crystals at 300 K. The substitutional fraction, f_s, measured in situ after Ba implantation at 5 and 77 K is 0.40 $\pm$ 0.08 /73/. The results are summarized in Table 10. It is noted that f_s is independent of the crystal direction and of the Ba concentration below 0.30 at.% and is constant for temperatures below 100 K. Fig. 33a shows as an example the angular yield curves from Ba and V atoms measured through the <111> axial direction. A narrowing of the scan curves for Ba indicates that the Ba atoms are not located on perfect substitutional lattice sites but are somewhat displaced. The displacement can be attributed to the formation of Ba-vacancy complexes with one vacancy per Ba atom. In this complex configuration, the Ba atom can relax towards the vacancy.

Table 10   *Dependence of the substitutional fraction (f_s) measured through the <111> and the <110> axial directions on the sample temperature during implantation T_I and measurements T_M with the Ba concentration as parameter.*

Ba-concentration at.%	T_I/K	T_M/K	f_s <111>	f_s <110>
0.05	} 300	} 300	0.0	0.0
0.20			0.0	
0.11	77	77	0.46+0.05	
	77	300	0.35∓0.05	
0.02			0.43+0.01	
0.12			0.38∓0.08	
0.60			0.09∓0.05	
0.08	} 5	} 5		0.42+0.1
0.21				0.40∓0.06
0.21		300		0.35∓0.06
0.24		5		0.45∓0.05

Warming up to 300 K a sample implanted at 77 K is followed by reduction of f_s from 0.46 to 0.35 (see Fig. 33a). Postirradiation with He ions of energy 300 keV and fluences of 2 x 10^{16} ion/cm² at 77 K do not affect the non-substitutional component of samples implanted at 5 and 77 K, respectively. Warming up these samples to 300 K is followed by reduction of f_s from 0.46 to 0.11
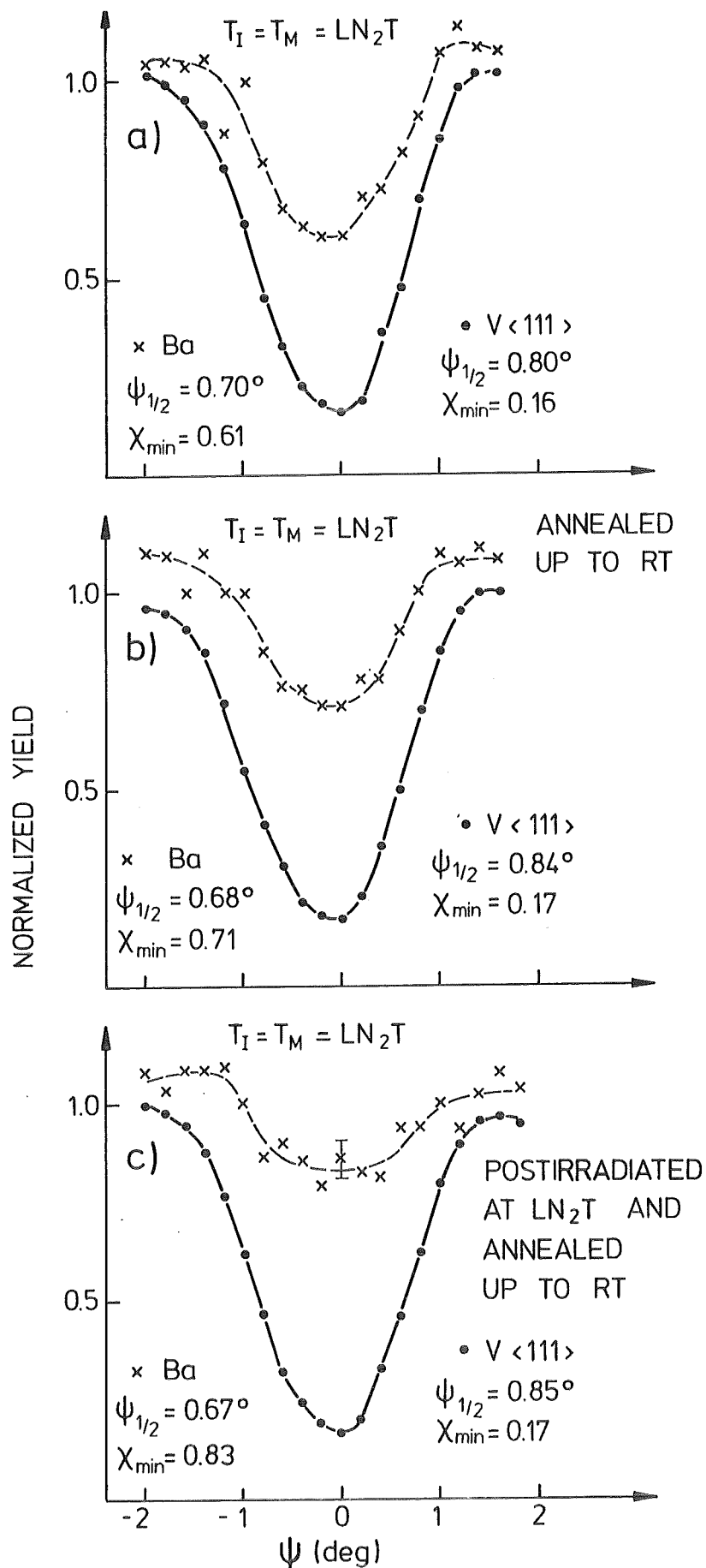
Fig. 33: Angular yield curves through the <111>axial direction from a Ba implanted V single crystals (a): $T_I=T_M=$ 77 K; (b) T_I = 77 K, annealed up to 300 K and measured at 77 K; (c) implanted and postirradiated with 1×10^{16} He$^+$/cm^2 (300 keV) at 77 K and annealed up to 300 K.

(see Fig. 33c). This result can be attributed to the stability
of Ba-vacancy complexes against annihilation with mobile inter-
stitials (at temperature below annealing stage III) and to the
trapping of mobile vacancies (at stage III) followed by forma-
tion of additional Ba-vacancy complexes.

4.3.3 VLa and VCe

VLa: La atoms occupy non-substitutional lattice sites if
implanted into V single crystals at 300 K, even at rather low
concentrations (for example 0.07 at.%). However, about 60% of
the implanted La atoms occupy substitutional lattice sites if
implanted at 5 or 77 K /73/. Fig. 34 shows an example of random
and <111> aligned backscattering spectra for 0.23 at.% La. The
measurements are performed in situ after implantation at 5 K.
The difference in the peak areas of La atoms in the <111> aligned
and random spectra is clearly visible. The non-substitutional
component (40%) can be attributed to the formation of La-vacancy
complexes within the dynamical cascade. In order to get more
informations on the lattice site occupation, angular scans are
measured and the results are shown in Fig. 35. A narrowing
in the La atoms angular scan relative to that of the V host
atoms is measured indicating that La atoms are slightly dis-
placed from their substitutional lattice sites. This result in-
dicates that point defects, probably vacancies, have been
trapped within the dynamical cascade on neighbouring lattice
sites. The substitutional fraction measured for different La
concentrations at different temperatures are summarized in
Table 11. It is noted that f_s is equal to 0.6 $\pm$ 0.05 indepen-
dent of the lattice temperature during implantation at temperatures
below 100 K. At rather high La concentrations, the substitutio-
nal fraction decreases to 0.37 at about 2.3 at.% La, probably
due to formation of additional La-vacancy complexes or due
to La precipitation. Warming from 5 K to 300 K a sample implan-
ted at 5 K is followed by reduction of f_s from 0.58 to 0.46 in-
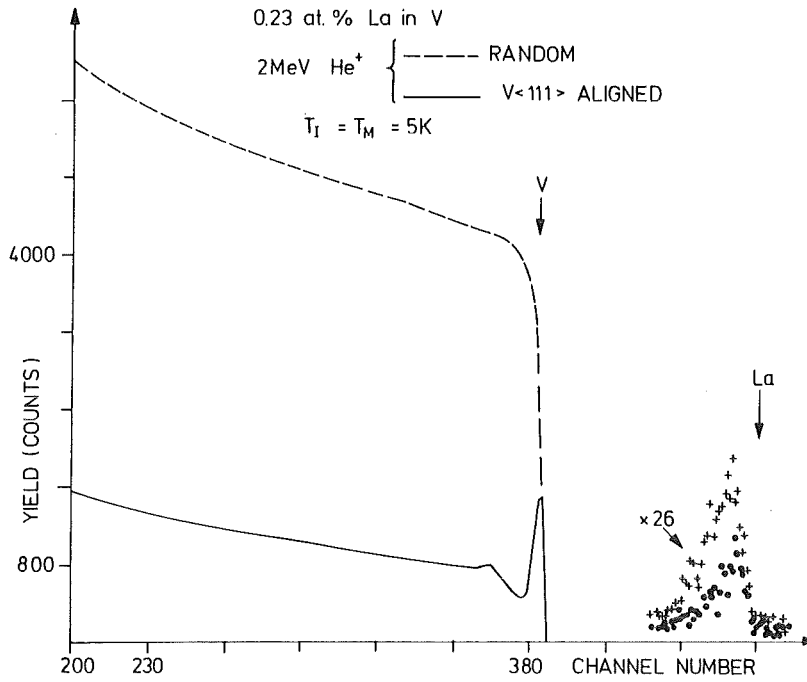dicating trapping of mobile vacancies.

Fig. 34: Random and <111>-aligned backscattering spectra from a V single crystal implanted with 0.23 at.%. The implantation and in situ-measurements are performed at 5 K.
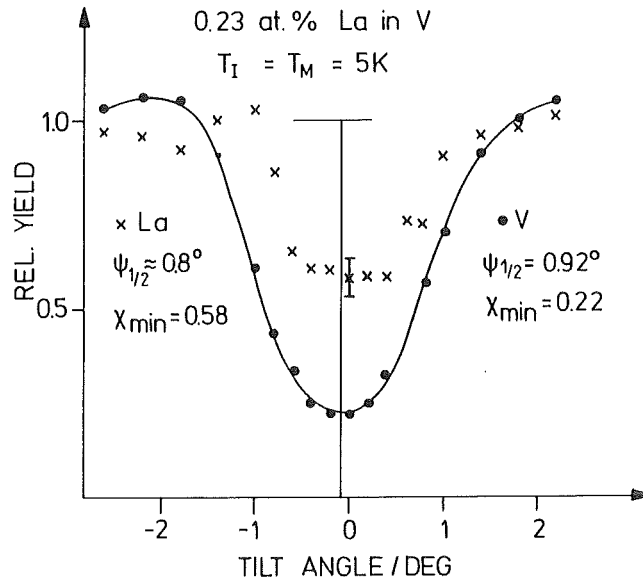

Fig. 35: Angular yield curves for La and V. $(T_I = T_M = 5 K)$.

Table 11 Dependence of the substitutional fraction (f_s) on the La concentration and the implantation and measuring temperatures (T_I, T_M)

La-concentration (at.%)	T_I/K	T_M/K	f_s
0.07	300	300	0.08 ± 0.08
0.25			0.08 ± 0.05
0.21	77	77	0.56 ± 0.05
0.28			0.65 ± 0.08
0.37			0.54 ± 0.05
2.30			0.37 ± 0.05
0.23	5	5	0.58 ± 0.08
0.23		300	0.46 ± 0.08

<u>VCe</u>: Ce ions implanted in V single crystals with rather low concentrations, show a temperature dependent substitutional fraction independent of the crystal direction. A summary of the f_s values as measured for samples implanted at 5 or 77 K and after annealing to 300 K is given in Table 12. For samples implanted at 5 and 77 K, f_s is equal to 0.70 ± 0.05 independent of the lattice temperature. As in this temperature region the self-interstitial atoms (SIA's) become mobile, the results indicate that possible interaction with mobile SIA's do not affect the lattice site occupation of the implanted Ce atoms. Detailed angular yield curves through the <111> axial direction for a V single crystal implanted at 5 K (Fig. 36a) reveal similar critical angle for Ce and V atoms indicating that about 70% of the Ce atoms are located in substitutional sites without relaxations.

Table 12 Dependence of the substitutional fraction (f_s) of Ce atoms implanted into V, on the temperature during implantation and measurement (T_I, T_M).

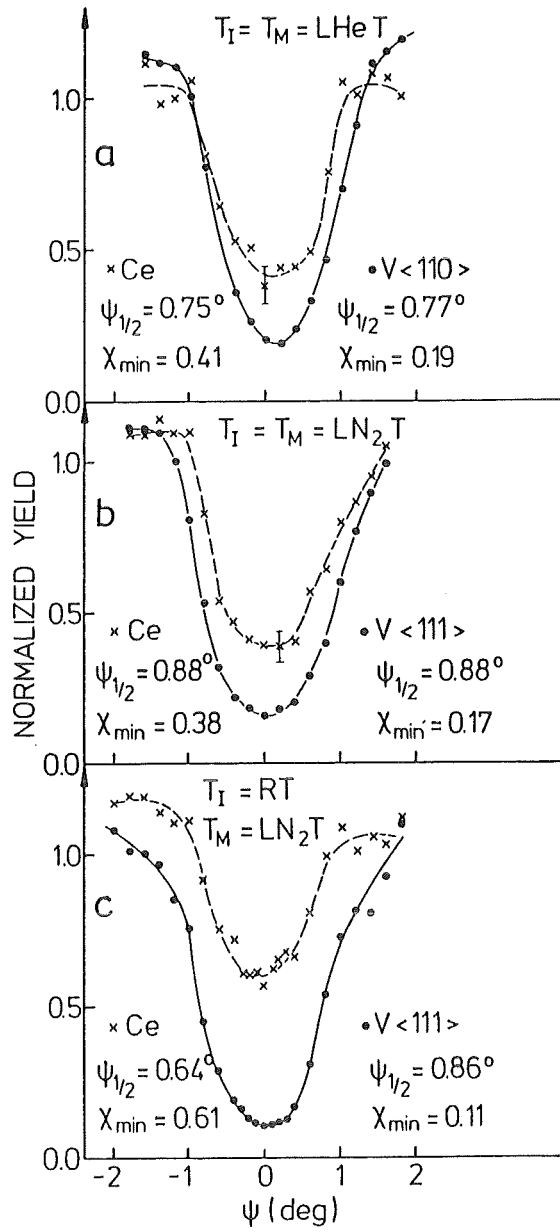| Ce-concentration at.%	T_I/K	T_M/K	f_s
0.04	300	300	0.13 ± 0.08
0.20			0.35 ± 0.05
0.08	5	5	0.73 ± 0.05
		300	0.62 ± 0.05
0.04	77	77	0.71 ± 0.05
0.12			0.73 ± 0.05

Fig. 36: Angular yield curves of the Ce and the V atoms through high symmetry directions of Ce implanted vanadium single crystals. The Ce-concentrations are between 0.08 and 0.2 at.%. a. As-implanted at 5 K; b. As-implanted at 77 K; c. Implanted at 300 K and measured at 77 K.

Similar results are noted for samples implanted and analyzed in situ at 77 K. The corresponding angular yield curves through the <111> axial direction are shown in Fig. 36b. A small narrowing of the Ce angular scan relative to that of the V host atoms indicates that the Ce-atoms are slightly displaced from the substitutional lattice sites, probably due to formation of Ce-vacancy complexes. After warming up a sample implanted at 5 K to 300 K, f_s decreases slightly from 0.73 to 0.62. The non-substitutional component (30%) could be attributed to the formation of Ce-vacancy complexes within the dynamic cascade. Postirradiation with He ions up to fluence of 2 x 10^{16} He^+/cm² at 77 K do not affect the non-substitutional component indicating the stability of these Ce-vacancy complexes against annealing by mobile SIA's.

Implantation at 300 K reveal a quite different behaviour in comparison with the implantation at low temperatures. Firstly, the angular yield curves through the <111> axial direction of a V single crystal implanted with 0.17 at.% Ce show that the critical angle of the Ce atoms is smaller than that of the host atoms (Fig. 36c). This result indicates that Ce atoms are slightly displaced from the substitutional sites. Secondly, the substitutional fraction of Ce at low concentrations is found to be smaller than that reached at low temperatures at the same Ce concentration. With increasing Ce concentration f_s increases and reaches a maximum value of about 0.66 at 3.3 at.% Ce (Fig. 37). It is noted that the maximum value of f_s (0.66) is approximately equal to the value (0.70) reached for samples implanted with low Ce concentrations at 5 or 77 K. The critical angle of Ce atoms increases also with increasing Ce concentration and is equal to that of the V host atoms at about 0.45 at.% Ce indicating the occupation of regular lattice sites. This effect is demonstrated by the angular yield curves through the <111> axial direction shown in Figs. 38a to c. It should be noted that the angular yield curves for 0.35 at.% Ce (Fig. 38b) seems to be composed of two components. The first component reveals a smaller critical angle than that of the V atoms (as in Fig. 38a) indicating slight displacements of the impurity atoms from the substitutional sites. The second component shows a perfect occupation of the lattice positions. The first component decreases with increasing
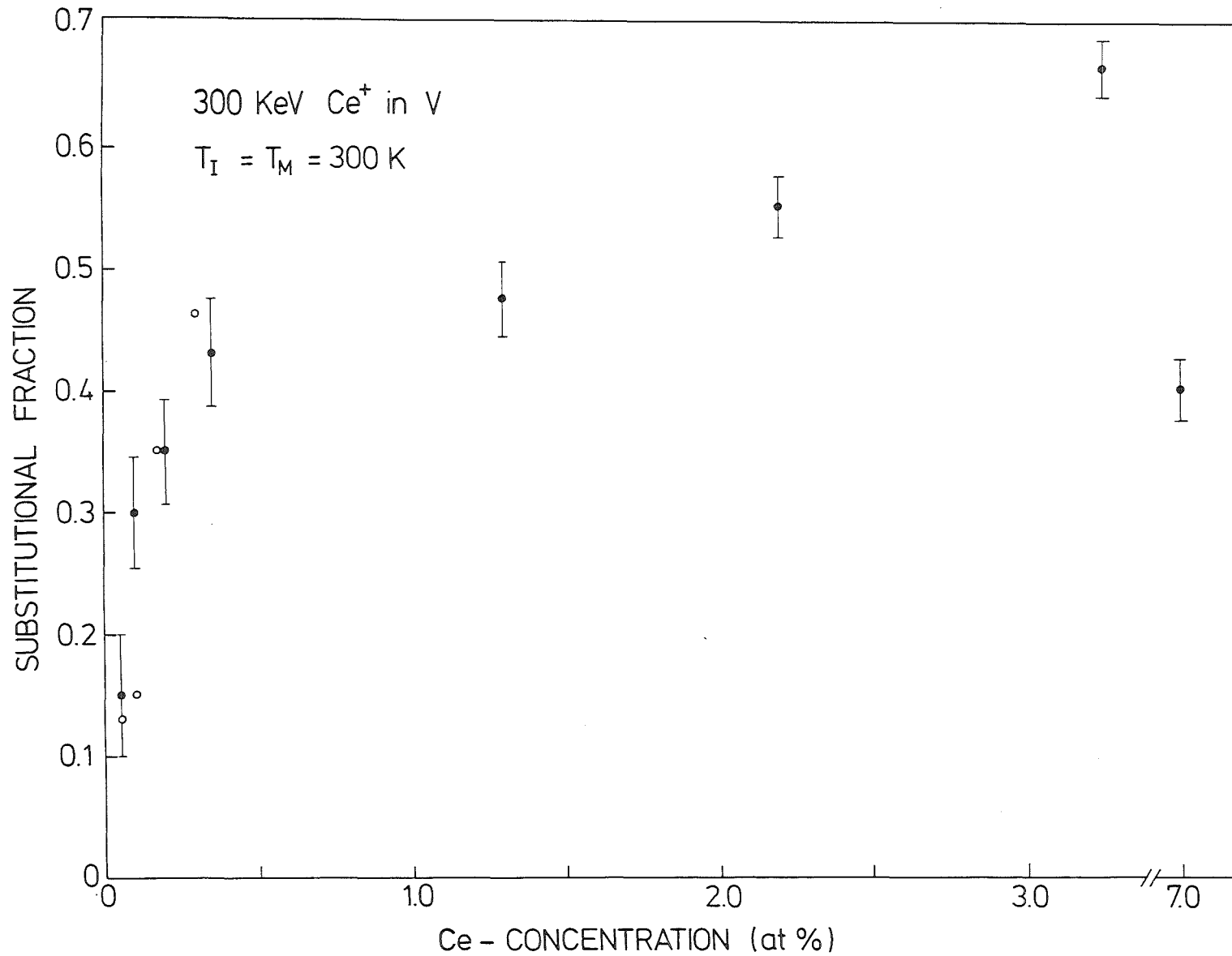
Fig. 37:   The substitutional fraction of Ce ions implanted into vanadium at 300 K, as a function of Ce-concentration. Inclosed are the results from two different samples.
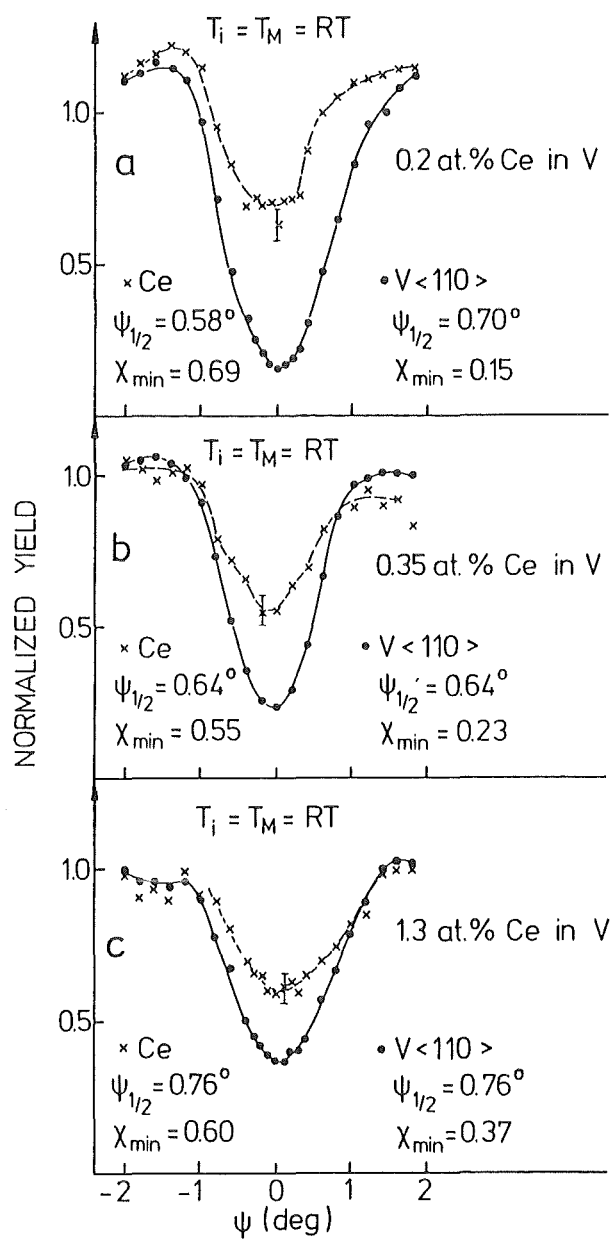
Fig. 38: Angular yield curves for Ce and V through the <111>-axial direction from a vanadium single crystal implanted with Ce at 300 K. a. 0.2 at.% Ce; b. 0.35 at.% Ce; c. 1.3 at.% Ce.
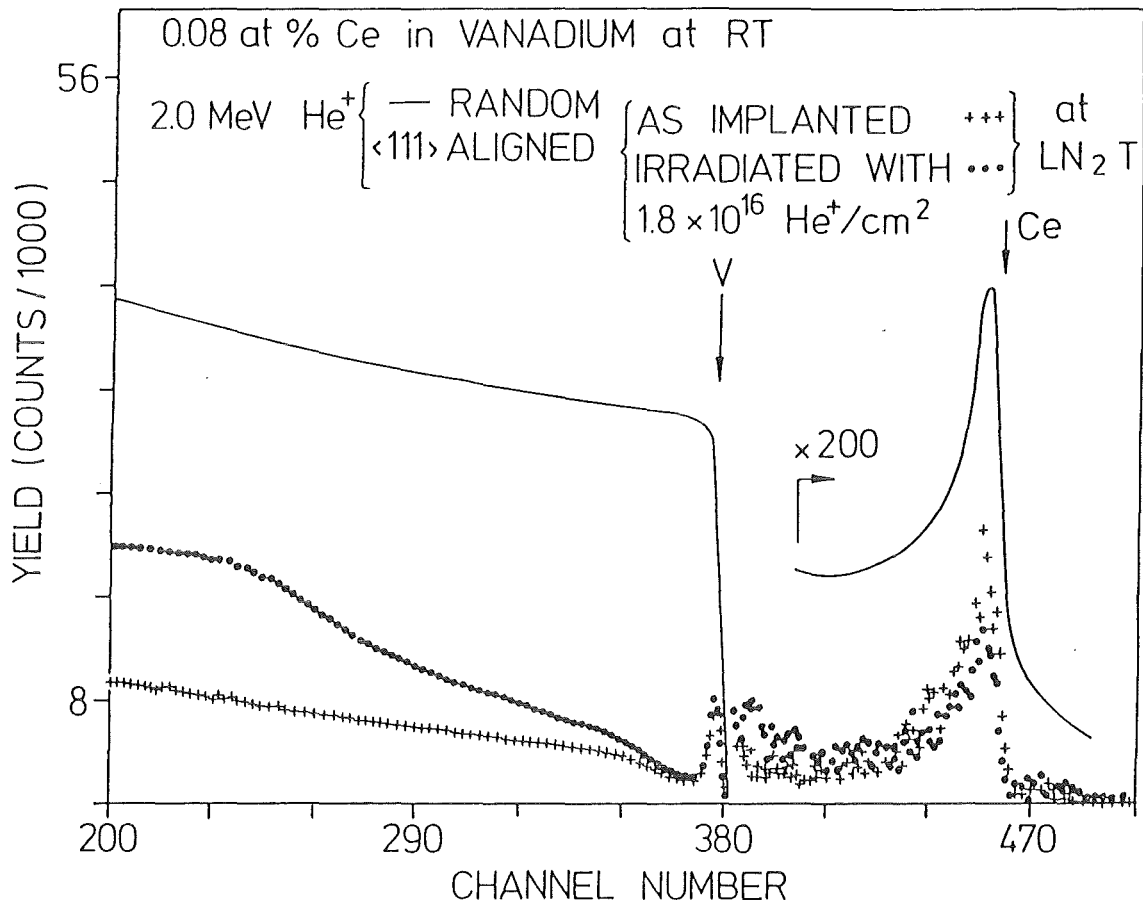
Fig. 39: Random and <111> aligned backscattering spectra from a vanadium single crystal implanted with 0.08 at.% Ce at 300 K. The <111> aligned spectra are shown before and after postirradiation with 1.8 x 10^{16} He^+/cm², 200 keV at 77 K.

Ce concentration and vanishes at about 0.45 at.%.

The most simple explanation of this behaviour, i.e., the rather low substitutional fraction and the narrowing of the angular scan for Ce after low dose implantation at 300 K, would be the assumption that Ce-multivacancy complexes have been formed by trapping mobile vacancies. To prove this hypothesis samples implanted at 300 K are cooled to 77 K and are post-irradiated with He ions. In Fig. 39 aligned and random back-scattering spectra performed at 77 K are shown for a V sample implanted at 300 K with 0.08 at.% Ce. After postirradiation with 1.8 x 10^{16} He^+/cm² (200 keV) the area of the Ce peak is found to decrease. The dechanneling in the host lattice in-

creases due to disorder produced by the He ions. The results of
these postirradiation experiments are summarized in Table 13.
With increasing He ions fluence, f_s is seen to increase. For
a sample implanted with 0.08 at.% Ce a maximum value for f_s
of 0.75 is reached. This value is in agreement with the highest
value obtained after implantation at 77 K. More informations
can be obtained by comparing the angular yield curves before
(Fig. 36c) and after postirradiation (Fig. 40). It is noted
that f_s and the critical angle of the Ce atoms increase after
postirradiation although $\psi_{1/2}$ for Ce is still smaller than that
of V atoms.

Table 13 *Influence of postirradiation with He ions at 77 K on the
substitutional fraction of $\underline{V}Ce$ systems produced by implantation
at 300 K.*

Ce-concentration (at.%)	Fluence (He$^+$/cm^2)	f_s ($\pm$ 0.05)
0.08	0	0.15
	2×10^{15}	0.64
	5×10^{15}	0.71
	1.8×10^{16}	0.75
0.17	0	0.36
	2×10^{16}	0.56
0.3	0	0.46
	2×10^{16}	0.58

The last results show the possibility of annealing Ce-vacancy
complexes which are formed at 300 K. If the postirradiated
samples are warmed up to 300 K, f_s decrease to 0.2 indicating
that vacancies become mobile and get trapped by the Ce atoms.
Postirradiation of $\underline{V}Ce$ sample produced at 77 K with 2×10^{16}
He$^+$/cm^2 at 300 K is followed by a decrease of f_s from 0.67
to 0.38 probably due to trapping of mobile vacancies.

It is noted that only in the case of the system $\underline{V}Ce$ a small
f_s values reached after implantation at 300 K are increased by
postirradiation at 77 K. This and also the unusual increase of
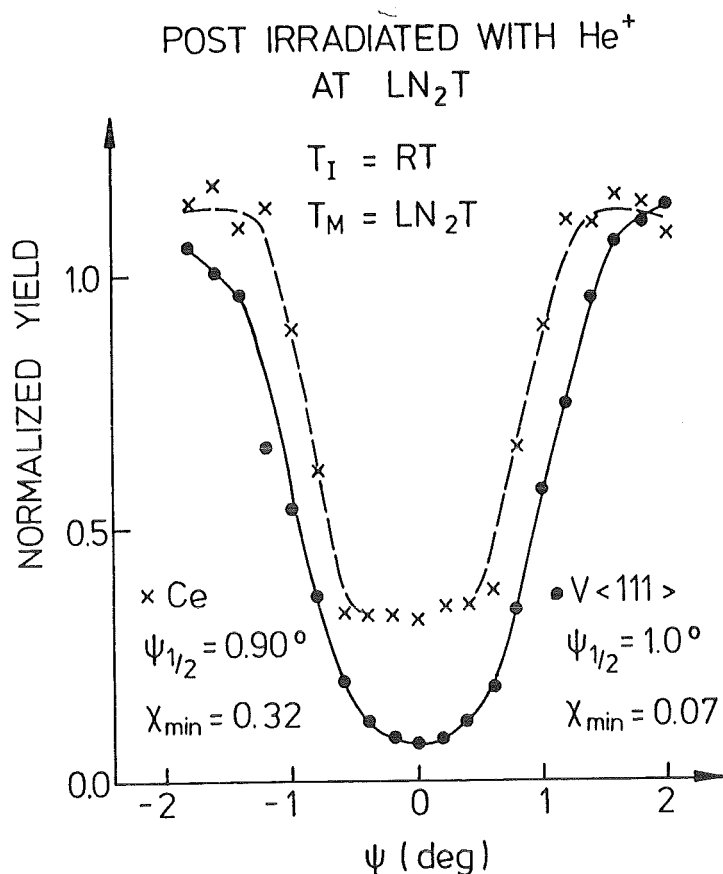f_s with increasing Ce concentration ,discussed in the following,

Fig. 40: Angular yield curves for Ce and V atoms through the <111>-axial
direction of a vanadium single crystal after Ce implantation
at 300 K followed by postirradiation with $2 \times 10^{16} He^+/cm^2$ at 77 K.

are due to the intermediate value of the heat of solution
for this system (120 kJ/mol) which lie between the cor-
responding values for the highly substitutional systems
and the partially substitutional ones as will be discus-
sed in chapter 5.1.4 and chapter 5.2.

The increase of both f_s and the critical angle for Ce
with increasing Ce-concentration can be attributed to the
annealing of the existing Ce-vacancy complexes and the ge-
neration of additional sinks for vacancies during further
implantation. New Ce-vacancy complexes will be also formed,
however, the equilibrium state between complex formation and
annealing is shifted because vacancies generate their own
sinks. In this way the concentration of mobile vacancies

and thus the formation probability of Ce-vacancy com-
plexes is reduced. In order to prove the assumption
discussed above, the following pre- and postimplantation
experiments with Au ions are performed. Au ions are implan-
ted into vanadium single crystals at 300 K to a peak con-
centration of 0.1 at.%. The substitutional fraction for Au
atoms is equal to one. Therefore the Au atoms itself are
not expected to influence the situation of the Ce atoms
which are postimplanted within the same projected range
to a peak concentration of 0.15 at.%. The measured substitu-
tional fraction for the Ce-atoms is 0.64, which is larger
than the value of 0.3 obtained without preimplantation
(see Fig. 37). This result indicates that mobile vacan-
cies which are produced during implantation of the Ce ions
are mainly trapped by competing vacancy trapping centers formed
during the preceding Au ion implantation. In this way the proba-
bility of Ce-vacancy complex formation is reduced. On the other
hand, implantation of 0.46 at.% Ce in vanadium at 300 K followed
by postimplanting Au ions to a peak concentration of about
0.37 at.%, results in an increase of the substitutional frac-
tion of Ce from about 0.45 to 0.73. This result shows that
Ce-vacancy complexes are dissolved during the postbombardment,
accompanied by the formation of competing vacancy trapping centers.

Annealing experiments at temperatures above RT have been
performed on some $\underline{V}$Ce samples to study the influence of vacancy
cluster annihilation on the lattice site occupation of Ce atoms.
Figs. 41a and b show the angular yield curves for the Ce and
the V atoms before and after annealing to 525 K, respectively.
By comparing the angular yield curves of the Ce atoms it is
concluded that Ce-trivacancy complexes are formed leading to
a flux peak in the <111>-axial direction (Fig. 41b). The Ce-posi-
tion between 3 vacancies in the (110) plane lies within an
isoscales triangle which after projection into the (111) plane,
results in a position 10% displaced from the center. Thus a
broadening of the flux peak is expected in agreement with the re-
sult. At 575 K the angular scan indicates a random position
for the Ce atoms. As small vacancy clusters dissociate at
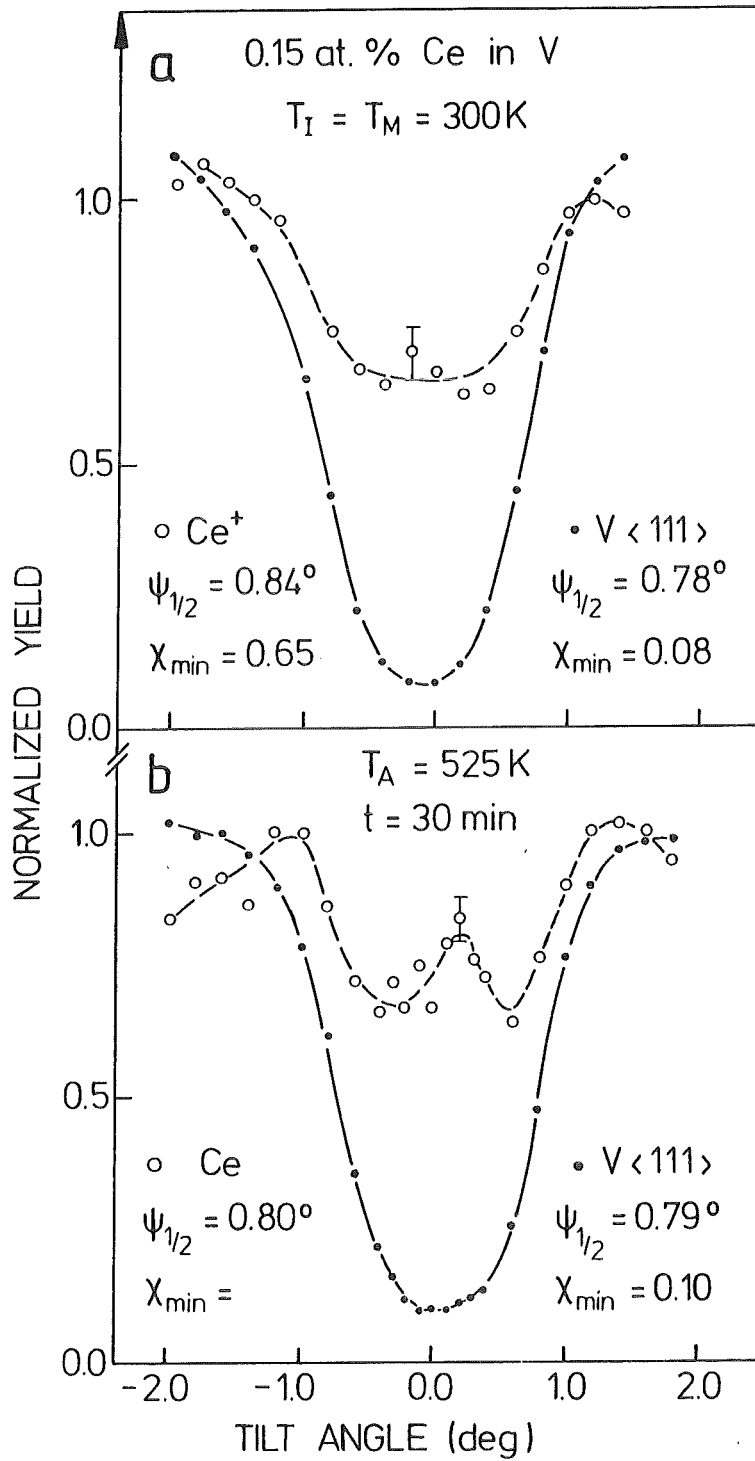
Fig. 41: Angular yield curves for Ce and V through a <111>-axial direction of a vanadium single crystal implanted with 0.15 at.% Ce. a. As-implanted at 300 K, b. annealed up 525 K and measured at 300 K.
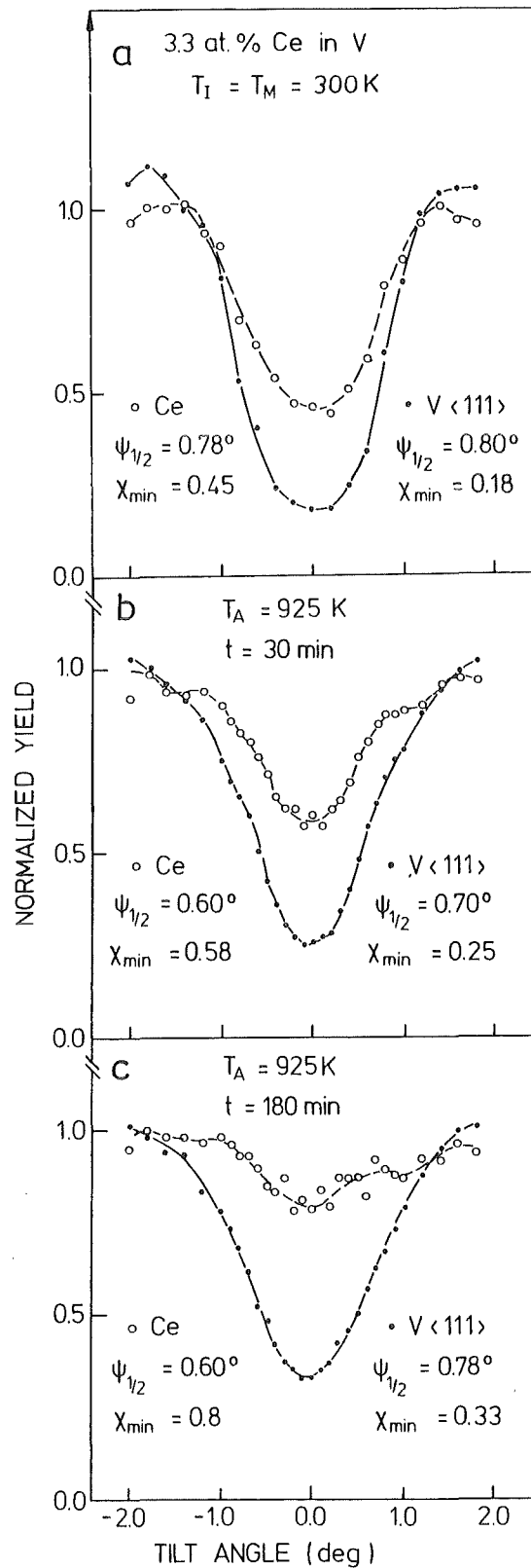
Fig. 42: Angular yield curves for Ce and V atoms through the <111> axial direction of a V single crystal implanted with 3.3 at.% Ce.
a. implanted at 300 K; b. annealed at 925 K for 30 min;
c. annealed at 925 K for 180 min.

this temperature range /17/, the result is attributed to the interaction of Ce atoms with the resultant free migrating vacancies.

The annealing behaviour of a high dose Ce-implanted V-sample (3.3 at.% Ce) is quite different. For annealing temperatures up to 800 K the angular yield curves for the Ce atoms have the same critical angle as the V host atoms (shown in Fig. 42a for the as-implanted sample). Upon annealing up to 925 K, a narrowing in the Ce angular yield curve is observed (Fig. 42b) followed by a reduction of the f_s-value from 0.66 to 0.47. After prolonged annealing at 925 K, f_s decreased to 0.14.

In the córse of high temperature annealing a direct backscattering peak is formed in the implanted region of the aligned host spectrum indicating the displacement of V atoms. The displacement of Ce and V atoms after high temperature annealing may be attributed to the formation of a V-Ce compound. Such an effect has been observed previously for the VGa system /69/. During the process of compound formation the Ce atoms first precipitate coherently (Fig. 42b) and then occupy several distinct interstitial lattice sites as indicated by the complex structure of the angular yield curve shown in Fig. 42c. A detailed structure analysis of the compound by X-ray diffraction has not yet been performed and was not the purpose of this study.

5. DISCUSSION AND CONCLUSIONS

5.1 Ion Implanted Diluted Alloys

Lattice location studies for implanted ions of different masses and chemical properties into vanadium single crystals at different lattice temperatures are performed over a wide range of impurity concentration. The results of implantation with low doses will be first discussed and compared with empirical and theoretical criteria to get an idea about the most important parameters which influence the lattice site occupation of the implanted ions in metals. For implanted ion concentration of 0.1 at.% (used here) the mean distance between the implanted impurities is about 3 nm so that an interaction between impurities is not expected.

5.1.1 Comparison with Empirical Criterion

The equilibrium solid solubility limits proposed by Hume-Rothery are: The difference in the atomic size between the solute and the solvent must be less than ±15% of the solvent's atomic size. The electronegativity difference must be less than 0.4 /5/. The modified rules for solid solubility limits of metastable systems which are produced by ion implantation are: The size difference between the implanted impurity and the host atoms must be in the range between -15% and +40% of the host atomic size. The electronegativity difference must be less than 0.7 /7/. The Darken-Gurry plots based on the equilibrium solid solubility limits and the modified limits for metastable implanted systems are usually used to separate the substitutional implanted species from the non-substitutional ones in a metallic host /75 a,b/. It was concluded that the modified rules may be used to predict the substitutionality when any atomic species is implanted in any metal with success of about 91% /7/.

Fig. 43 shows the Darken-Gurry plot for all considered atoms implanted into vanadium at 300 K. The black circles indicate implanted species which are substitutional with $f_s \geq 0.50$ and the
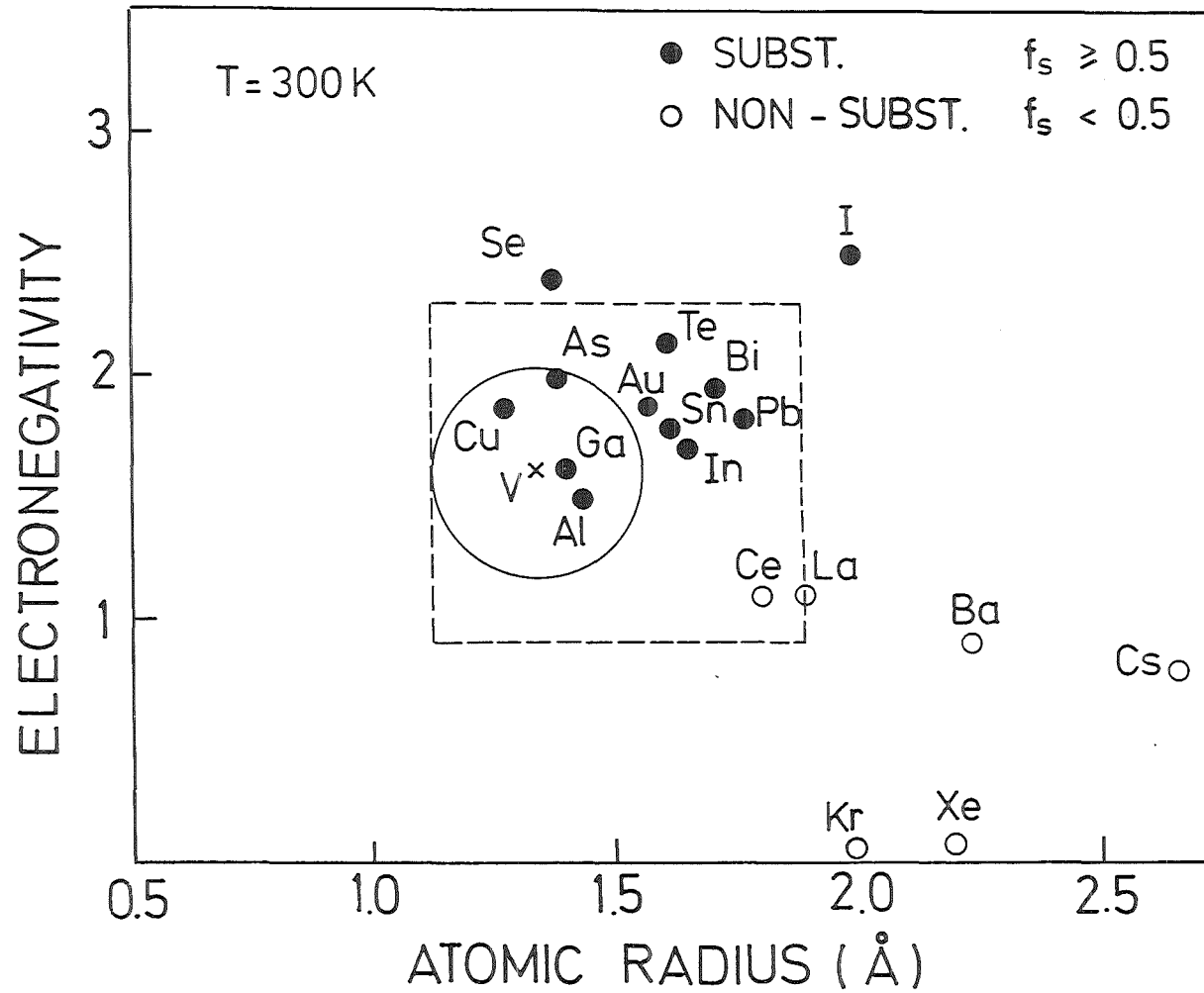
Fig. 43: *Darken-Gurry plot for implanted vanadium based diluted alloys. The implantations and measurements are performed at 300 K.*

open symbols represent species which are non-substitutional with $f_s < 0.50$. The rectangle (dashed line) represents the solid solubility limits of the modified rules and the circle (full line) shows the equilibrium solid solubility limits. It is noted that all soluble elements inside the full circle are also substitutional as expected. The elements Ce, La, Se and I do not obey the modified rules. While Ce and La lie inside but are not substitutional Se and I lie outside but are substitutional. Ba, Kr, Xe and Cs occupy, as expected, non-substitutional sites. It is noted that the electronegativity values are taken from Ref./4/. Howevere no values are listed for inert gases. For Kr and Xe a value of O.O is assumed to be reasonable and is used in this work. The values of the atomic radius are those of the neutral atoms and are taken form Ref./76/.

It can be concluded that the present results (after implantation at room temperature) are predicted with high degree of success by applying the modified rules as was reached previously for other implanted systems /7/. However, the large substitutional fractions for Xe, Cs and Ba observed after implantation at low temperatures are clearly in contradiction with the predictions of all the empirical rules. Therefore it is concluded that the apparent agreement of the results observed for room temperature implants with the predictions of the empirical rules is due to the mobility of lattice vacancies and therefore to the impurity-vacancy interaction in the delayed regime of the dynamic cascade as will be discussed in detail in chapter 5.1.3.

5.1.2 Comparison with the Replacement Collision Theory

In order to study the collisional effects on the lattice site occupation of implanted impurity without the influence of mobile point defects implantation and in situ-analysis are carried out at 5 K. A comparison of the substitutional fractions with the replacement collision probability can be seen in Fig. 44. The solid curve shows the calculated replacement collision probability as a function of the atomic number of ions implanted in vanadium. The full symbols show the measured substitutional fractions after implantation at 5 K.
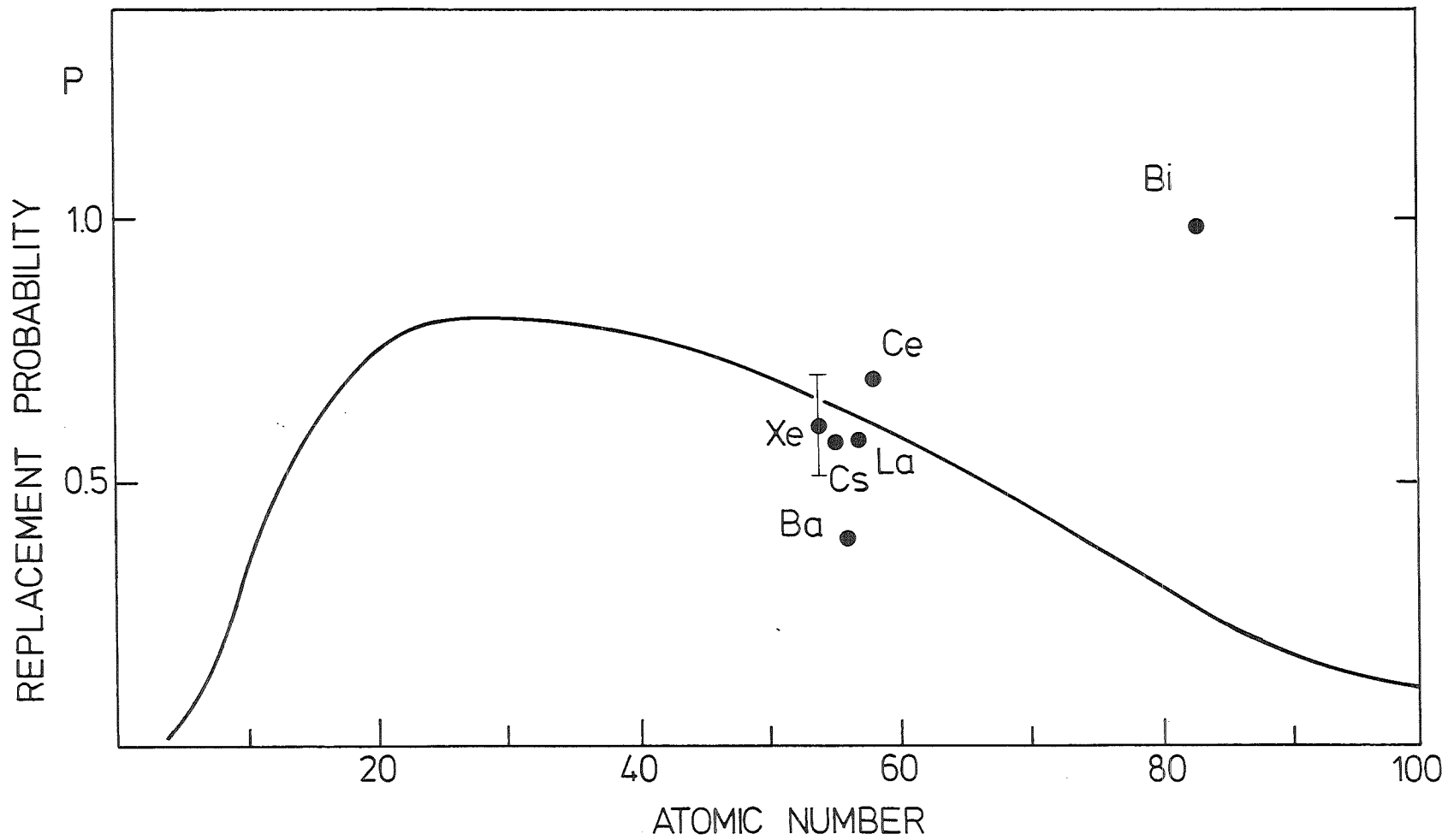
Fig. 44: Comparison of the substitutional fraction of different impurity atoms, implanted in vanadium at 5 K, with the replacement collision probability /14/ (full line curve).

It is noted that the substitutional fractions for Xe, Cs, Ba, La and Ce vary between 0.4 and 0.73 while nearly the same replacement collision probability (0.60) is calculated for all these elements. Further a complete disagreement between the experiment and theory can be noted for Bi. A similar discrepancy has been noted previously for the system CuAu where Au is 100% substitutional in Cu when implanted and analyzed below 15 K /77/. The last results indicate that soluble and nearly soluble impurity atoms recombine with the lattice vacancies, within the dynamic cascade. In this respect the impurities behave similar as displaced host atoms where it is known that about 70% of the displaced atoms recombine athermally with neighboured vacancies /57/. Non-soluble atoms interact with further vacancies. Therefore it is concluded that the replacement collisions are not an important process for the lattice site occupation of the implanted impurities. The recombination of soluble and nearly soluble impurities with vacancies and the interaction of highly non-soluble impurities with several vacancies within the lifetime of the cascade (10^{-11} sec) seem to be the most important mechanisms as will be outlined in the next chapter.

5.1.3 Impurity-Point Defect Interactions

It is noted that for irradiated vanadium samples, annealing effects (2%) have been observed already after warming up to 4.7 K /16/, although the main annealing stage for self-interstitials lie at about 47 K /18,19/. The temperature stage for vacancy motion lies between 200 and 300 K /17/, indicating that point defect-impurity interactions are quite probably during implantation at 300 K.

It is further well known that point defects can interact with impurity atoms under irradiation. Mixed dumbbells and foreign atom-vacancy complexes may be formed for example by irradiating Al-based alloys /78/. For CuMo it is shown that by increasing the substrate temperature during implantation to 350°C above stage III in Cu (300 K), the f_s value decreased from 1.0 to 0.30 /7/. Xe-vacancy complexes are also an example

which have been studied by Mössbauer spectroscopy after implantation of radioactive [133]Cs in Mo, W and Ta at 300 K /79/.

The substitutional fraction values for the systems $\underline{V}$Ba, $\underline{V}$La and $\underline{V}$Cs (Fig. 45) are shown to be independent of the lattice temperature for temperatures below 100 K. As the main recovery stage for self-interstitial atoms lies at 47 K, it is concluded that mobile self interstitials do not affect the lattice site occupied by these oversized atom. As stage III of vacancy motion lies between 200 and 300 K the formation of impurity-vacancy complexes by trapping mobile vacancies is quite probable and could explane the rather low substitutional fraction obtained for Kr, Xe, Cs, Ba, La and Ce in vanadium after implantation at 300 K (Fig. 45). The decrease of the f_s values for the systems $\underline{V}$Cs, $\underline{V}$Ba, $\underline{V}$La and $\underline{V}$Ce produced at 5 K, with and without post-irradiation with He ions at 77 K after annealing to 300 K can be attributed also to trapping of mobile vacancies. On the other hand, the increase of the substitutional fraction for $\underline{V}$Ce which is produced at 300 K after postirradiation with He^{+} at 77 K shows the possibility of annealing such complexes probably by absorbing mobile self interstitial atoms. It should be noted that $\underline{V}$Ce is the only system where low f_s values obtained after implantation at 300 K can be increased after postirradiation at 77 K. Ba and Cs-vacancy associations cannot be annealed by absorbing mobile self interstitials indicating that the binding energy of such associations plays a large role for radiation induced annealing. The influence of the binding energy on radiation induced annealing is discussed in the next chapter.

5.1.4 Correlation with the Heat of Solution

It is assumed in a previous theoretical discussions that elements with positive heat of solution H_{sol} would have a rather high trapping probability for vacancies in order to reduce (H_{sol}) /80/. The relation between H_{sol} and the impurity-vacancy binding energy (B_{iv}) is further discussed by M. Doyama /81,82/. It is assumed that the binding energy (B_{iv}) is directly
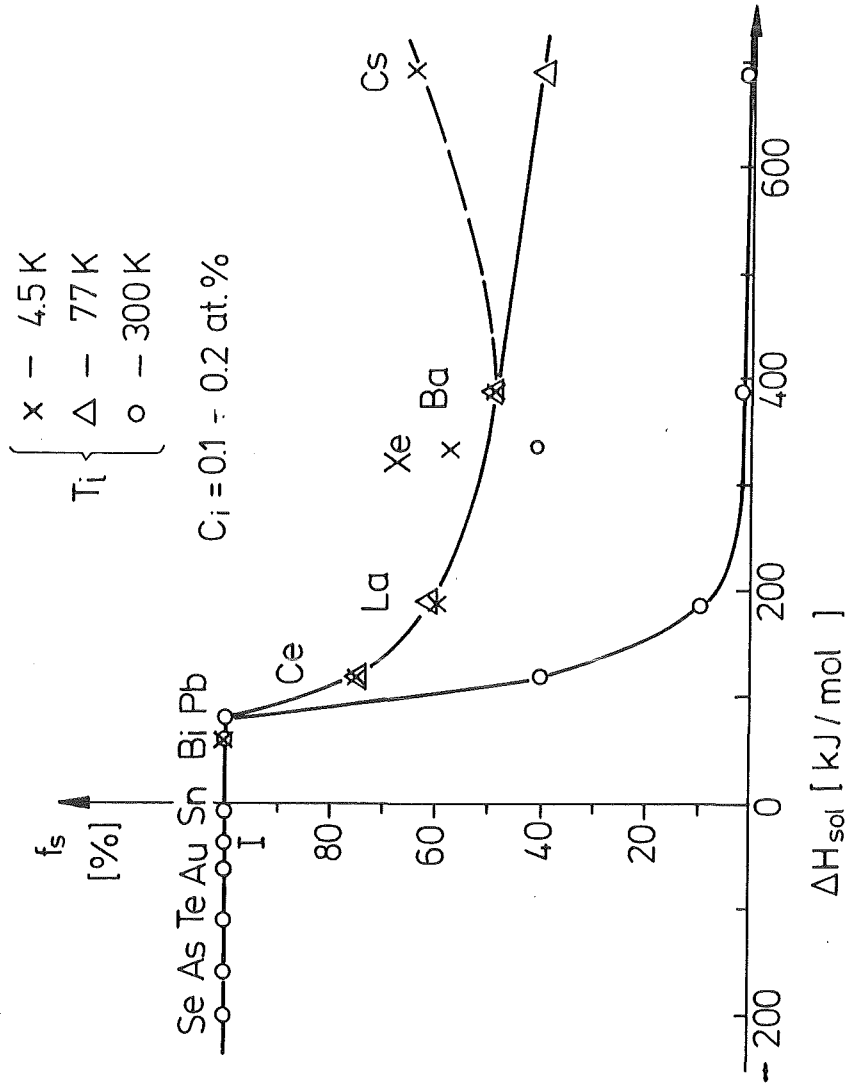
Fig. 45: *Substitutional fraction (f_s) of impurity atoms in vanadium single crystals as a function of the calculated heat of solution.*

proportional to the heat of solution. As the distortions of the lattice and of the electronic structure near the impurity atom increases with increasing heat of solution, this distortion will relax when a vacancy is trapped by the impurity. The relaxation energy which is the binding energy (B_{iv}) increases with increasing the distortion.

The correlation between f_s values for the considered systems and the corresponding heat of solution (H_{sol}) as estimated from Miedema's theory /83/ is shown in Fig. 45. It is noted that elements having a negative heat of solution in V are 100% substitutional at 300 K. Other elements with small positive heat of solution (for example Bi) are 100% substitutional independent of the lattice temperature. Elements like Ce, La, Xe, Ba and Cs, which have a rather high heat of solution (between 120 and 690 kJ/mol) reveal a temperature dependent substitutional fraction. As it can be seen from the Fig. 45, Ce, La, Ba and Cs have only a small or no substitutional component when implanted at 300 K. As discussed in chapter 5.1.3 these results are attributed to the trapping of mobile vacancies leading to the formation of impurity-vacancy associations accompanied by the displacement of the impurity atoms from the substitutional lattice sites. The stability of the impurity-vacancy complexes for the system VCs, VBa and VLa having a very high heat of solution against annealing by postirradiation indicates that the B_{iv}-values for these systems are rather high. On the other hand, annealing of Ce-vacancy complexes with an intermediate heat of solution by postirradiation indicates that the B_{iv} value is low. These results therefore support the assumption /81,82/ that the binding energy of the impurity-vacancy complexes is directly proportional to the heat of solution.

At temperatures below 100 K, where vacancies are not mobile the elements Ce, La, Xe, Ba and Cs still have non-substitutional components, which cannot be attributed to trapping of mobile vacancies in the delayed regime of the cascade. These components can also not be attributed to impurity precipitate formation, as firstly the average distance between the

impurities is about 30 Å and diffusion is negligible at low
temperatures. Further the fraction of non-substitutional atoms
does not depend on the concentration of the impurities in the
range between 0.03 and 0.3 at.% which would otherwise be ex-
pected for precipitate formation. Thus the only explanation
for these non-substitutional components is that the impurity
atoms could have a certain probability to come to rest, during
the slowing down process, in a vacancy rich region of the dis-
placement spike.

Some elements with a very high heat of solution like Ba
and Cs could also trap vacancies athermally during the cooling
time of the cascade (10^{-11} sec) as the vacancies still have
jump frequency of about 0.3×10^{13} jump/sec /57/.

As an exception, the substitutional fraction of Cs measured
after implantation at 5 K is larger than that measured after
implantation at 77 K. The result could be explained as follows:
because Cs has the largest heat of solution (690 kJ/mole) of
all elements in V the athermal trapping probability for vacan-
cies during the cooling time of the cascade (10^{-11} sec) could
be sensitive to the lattice temperature.

In general, it is concluded that the empirical methods which
are based on thermodynamical equilibrium is not successful to
predict the substitutionality of atomic species implanted in a
host metal. This holds particularly when the implantation is per-
formed at low temperature where the point defects are not mobile.
The ion implantation is seen to be able to produce metastable
systems which are far from the thermodynamic equilibrium.

On the other hand, replacement collisions are not respon-
sible to a high degree for the lattice site occupation of im-
planted ions. The main basic mechanisms for lattice site occu-
pation in metals is the recombination of the impurities with the
lattice vacancies in the cascade and additional trapping of
vacancies either in the cascade regime or in the delayed

regime, a process which is governed by thermodynamic driving forces.

5.2 Ion Implanted Concentrated Alloys

Increasing the implanted ion concentration leads to the following processes:
The increase of the impurity atoms concentrations is accompanied by a decrease of the mean distance between the impurities. If the binding energy between two impurity atoms is larger than that between host and impurity atoms coherent or incoherent precipitation may occur. Coherent precipitation is observed for example for the systems $\underline{V}Se$ and $\underline{V}Te$ where f_s decrease and the angular width of the impurity angular scan becomes greater than that of the host. Incoherent precipitation is observed for example for the system $\underline{V}I$ where f_s decreases while the width of the impurity angular scan is still equal to that of the host atoms (see chapter 4.4.4).

Increasing the implanted ion concentration however may lead to an increase of the substitutional component. This unusual behaviour is observed only for the system $\underline{V}Ce$ (see chapter 4.3.3) and is explained as follows: At low concentrations, Ce-vacancy complexes are formed by trapping mobile vacancies. These complexes will be dissolved by further implantation. The equilibrium between complexes formation and dissociation will be disturbed if additional sinks for vacancies are generated.
In this way the concentration of mobile vacancies and thus the formation probability of Ce-vacancy complexes is reduced. The results from postimplantation experiments with Au ions at 300 K proved the last assumption. As Au atoms are 100% substitutional in V they produced only energetic cascade regions which dissolve the Ce-vacancy complexes and at the same time produce additional competing sinks for vacancies trapping.

Thermal annealing of the $\underline{V}Ce$ system with a relatively high Ce concentration (3.3 at.%) at 975 K leads to formation of coherent Ce precipitations followed by the formation of $\underline{V}Ce$ compounds. As a result of this compound formation both Ce

and V atoms are displaced from the substitutional lattice
sites.

Plastic deformation of the implanted layer is observed
as a result of high dose ion implantation. This effect is
measured for the first time for the system VAs /67/ and then
for other systems VSn, VTe, VCs and NbCs /68/. The higher the
size mismatch energy around the impurity atoms the smaller
is the critical concentration at which the deformation
process occurs. The effect is explained as follows: The misfit
strain fields around the impurity atoms activate a dis-
location slip system. As the implanted region is embedded in
the single crystal the slip direction will rotate towards
the tensile force vector which is parallel to the surface
normal /67/.

6. SUMMARY

Implantation of various soluble and nearly soluble species from groups III_a to VII_a of the periodic table (e.g. Ga, As, Se, In, Te, I, Pb and Bi) as well as simple metals (Cu and Au) in vanadium single crystals at 300 K result in a high substitutional component. The substitutional fraction of Bi (as an example) is equal to 1.0 independent of the implantation temperature between 5 and 300 K. The influence of mobile point defects on the lattice sites occupation of soluble or nearly soluble elements during ion implantation can be excluded. This statement does not hold for ion irradiation of diluted solid solutions and has not been checked for implanted undersized impurities with a large negative heat of solution.

The replacement collision theory predicts a substitutional fraction of about 30% for heavy ions in vanadium and only a maximum value of about 70% for elements having an atomic number similar to that of the host. The rather high substitutionality (100%) for all soluble and nearly soluble elements in V as well as the discrepancy in the substitutional fraction for Xe, Cs, Ba, La and Ce in comparison with the replacement probability indicate that the replacement collisions is neither the only nor an important mechanism for the lattice sites occupation of the implanted ions.

While non soluble species from groups I_a, II_a, III_b and some rare earth elements show a substitutionality between 40% and 70% upon implantation at 5 or 77 K they are non-substitutional after implantation at 300 K. These indicate that the mobility of vacancies between 200 and 300 K, reduce the substitutional fraction for these elements, probably due to the formation of impurity-vacancy complexes. Post irradiation and annealing experiments support this assumption.

Correlating the substitutional fraction for all the implanted species in vanadium to the heat of solution indicate that elements having a small negative or small positive heat

of solution reveal a high substitutional fraction independent
of the lattice temperature. In contrast those elements with
large positive heat of solution and therefore a high trapping
radius for vacancies are non-substitutional at 300 K.

With regard to all the results it is concluded that re-
placement collisions are not an important mechanism for the lat-
tice sites occupation of the implanted ions in metals. The main
mechanism is the recombination of foreign atoms with lattice
vacancies during the cooling period of the collisional cas-
cade (10^{-11} sec) and additional trapping of vacancies either
in the cascade regime or in the delayed regime, a process
which is governed by thermodynamical driving forces.

Plastic deformation of the implanted region, coherent or
incoherent precipitation of the implanted impurities as well
as formation of additional sinks for vacancy trapping which
disturb the equilibrium of impurity-vacancy complexes forma-
tion and dissociation ($\underline{V}Ce$), are observed at high implanted
ion concentrations.

REFERENCES

/1/ G. Dearnaley, Mater. Eng. Appl. 1, 28 (1978).

/2/ J.M. Poate, J. Vac. Sci. Techn. 15, 1636 (1978).

/3/ L.S. Darken and R.W. Gurry, Physical Chemistry
     of Metals (McGraw Hill, New York, 1955).

/4/ L. Pauling, The Nature of the Chemical Bond (Cornell
     University Press, Ithaca, 1960).

/5/   W. Hume-Rothery, R.E. Smallman, C. Haworth, The Struc-
     ture of Metals and Alloys (Institute of Metals, London,
     1969).

/6/ G. Gschneider, Jr., Theory of Alloy Phase Formation,
     edited by L.H. Bennett (The Metallurgical Society
     of AIME, New York, 1980) 1.

/7/ D.K. Sood and G. Dearnaley, in Applications of Ion Beams
     to Materials, edited by G. Carter, J.S. Colligon, and
     W.A. Grant, Inst. Phys. Conf. Ser. No. 28 (IOP London,
     1976) p. 196; D.K. Sood, Phys.Lett. A 68, 469 (1978).

/8/ A.R. Miedema, F.R. de Boer, and P.F. de Chatel, J. Phys.
     F3, 1558 (1973).

/9/ A.R. Miedema, Philips Tech. Rev. 36 (1976).

/10/ A.R. Miedema, F.R. de Boer, and R. Boom, CALPHAD 1,
     341 (1977).

/11/ J.R. Chelikowsky, Phys. Rev. B19, 686 (1979).

/12/ J.A. Alonso and S. Simozar, Phys. Rev. B 22, 5583 (1980).

/13/ J.A. Alonso and J.M. Lopez, Philisophical Magazine
     A45, 713-722 (1982).

/14/ D.K. Brice, Institute Phys. Conf. Ser. No. 28 c (1976).

/15/ P.H. Dederichs, Chr. Lehmann and H. Wegner, Phys. Stat.
     Sol. 8, 213 (1965).

/16/ R.R. Coltman, C.E. Klabunde, J.K. Redman and J.M. Williams,
     Rad. Eff. 24, 69 (1975).

/17/ H. Schulz, in:Point Defects and Defects Interactions in
     Metals, eds., Jin-Ichi Takamuta et al. (North Holland,
     Amsterdam (1982) 183); S. Tanigawa, I. Shinta and H. Iriyama,
     736.

/18/ C.E. Klabunde, J.K. Redman, A.L. Southern, and R.R. Coltman,
     jr.; Physica Stat. Sol. A 21, (1974) 303.

/19/ C.E. Klabunde, R.R. Coltman, Jr., and J.M. Williams, Fundamental Aspects of Radiation Damage in Metals, eds. M.T. Robinson, F.M. Young, Jr., ERDA Report Conf-751006 Oak Ridge, Tenn. (1976).

/20/ W.K. Chu, J.W. Mayer, and M.-A. Nicolet, Backscattering Spectrometry, 1978, Academic Press, New York.

/21/ J.F. Ziegler and W.K. Chu, Atomic Data and Nuclear Data Tables 13 (1974) 463.

/22/ J.A. Davies, J. Friesen and J.D. McIntyre, Can. J. Chem. 38 (1960) 1526.
J.A. Davies, J.D. McIntyre, R.L. Cushing, and M. Lounsbury, Can. J. Chem. 38 (1960) 1535.

/23/ M.T. Robinson and O.S. Oen, Appl. Phys. Lett. 2, (1963) 30.

/24/ G.R. Piercy, F. Brown, J.A. Davies and M. McCargo, Phys. Rev. Lett. 10 (1963) 399.

/25/ H. Lutz and R. Sizmann, Phys. Lett. 5, 113 (1963).

/26/ R.S. Nelson and M.W. Thompson, Phil. Mag. 8, 1677 (1963).

/27/ Channeling, Theory, Observation and Applications, ed. D.V. Morgan, J. Wiley + Sons (1973).

/28/ D.S. Gemmell, Rev. Mod. Phys. 26, 129 (1974).

/29/ J. Lindhard, K. Dan. Vidensk. Selsk. Mat. Fys. Medd. 34, 14 (1965).

/30/ C. Lehmann and G. Leibfried, J. Appl. Phys. 34, 2821 (1963).

/31/ J. Lindherd, Phys. Lett. 12, 126 (1964).

/32/ C. Erginsoy, Phys. Rev. Lett. 13, 360 (1963).

/33/ P. Gombas, in Handbuch der Physik, ed. Springer Verlag, Berlin (1956).

/34/ G.Z. Moliere, Naturforsch. A2, 133 (1947).

/35/ B.R. Appleton, C. Erginsoy and W.M. Gibson, Phys. Rev. 161, 330 (1967).

/36/ J.H. Barrett, Phys. Rev. B3, 1527 (1971).

/37/ M. Blackman, in Encyclopedia of Physics, ed. S. Flügge (Springer, Berlin, 1955) Part 1, 7, 377.

/38/ E. Bonderup, H. Esbensen, J.U. Anderson and H.E. Schiott, Rad. Eff. 12 (1972) 261.

/39/ W.M. Gibson, F.W. Martin, R. Stensgaard, F.P. Jensen,
      N.I. Meyer, G. Galaster, A. Johanssen and J.S. Olsen,
      Can. J. Phys. 46, 675 (1968).

/40/ H. Fischer, R. Sizmann, and F. Bell, Z. Phys. 22,
      135 (1969).

/41/ J.C. North, W.M. Gibson, Appl. Phys. Lett. 16, 126 (1970).

/42/ G. Fladda, K. Bjorkquist, L. Eriksson and D. Sigurd,
      Appl. Phys. Lett. 16, 313 (1970).

/43/ J.U. Andersen, E. Laegsgaard, and L.C. Feldman,
      Rad. Eff. 12, 219 (1972).

/44/ J.A. Cairns, R.S. Nelson, Phys. Lett. A 27, 14 (1968).

/45/ J. Lindhard, V. Nielson and M. Scharff, Mat. Fys. Medd.,
      36, 10 (1968).

/46/ J.A. Davies, in: Surface Modification and Alloying,
      eds. J.M. Poate, G. Foti, Plenum Publishing Corp. (1983).

/47/ H. Bethe, Ann. Physik 5, 235 (1930);
      H. Bethe, Handbuch der Physik, Springer Berlin 1933, 241.

/48/ O.B. Firsov, Sov. Phys. JETP 5, 1133 (1957).

/49/ W.S. Johnson and J.E. Gibbons, Projected Range Statistics
      in Semiconductors (Stanford Univ. Bookstore (1969)).

/50/ D.K. Brice, Ion Implantation Range and Energy Deposition,
      Sandia Labs., Albuquerque, N.M., SAND 75-0622 Report
      (1977).

/51/ K.B. Winterbon, Ion Implantation Range and Energy
      Deposition, Vol. 2, Plenum Press, New York (1975).

/52/ J.P. Biersack, L.G. Haggmark, Nucl. Instr. and Meth. 174
      (1980) 257.

/53/ J. Lindhard, M. Scharff, H.E. Schiott, Mat. Fys. Medd.
      33 (1963) 14.

/54/ Y. Yamamura, Y. Kitazoe, Rad. Eff. 39 (1978) 251.

/55/ R.S. Walker and A.D. Thompson, Rad. Eff. 37 (1978) 113.

/56/ G.H. Kinchin and R.S. Pease, Rep. Progr. Phys. 18
      (1955) 1.

/57/ M.W. Guinam and J.H. Kinney, Journ. of Nucl. Mat. 103,
      104 (1981).

/58/ W.W. Anderson, Solid State Electronics Pergamon Press
      11, 481 (1968).

/59/ G. Linker, M. Gettings and O. Meyer, Ion Implantation in
      Semiconductors and Other Materials, B.L. Crowder (Ed.)

Plenum Publ. Corp. 1973) 465, and Rad. Eff. 21, 51 (1974).

/60/ K.G. Langguth, KfK 2476 (1977).

/61/ P. Ziemann, KfK 2562 (1978).

/62/ R. Kaufmann, J. Geerk and F. Ratzel, Nucl. Instr. Meth.
209 (1983) 293-297.

/63/ H.W. Alberts, O. Meyer, J. Geerk, Rad. Eff., 69 (1983) 61-70.

/64/ G. Linker: Progress Report of Teilinstitut Nukleare
Festkörperphysik, KfK 2357 (1975/76) 86.

/65/ W.G. Moffatt, The Handbook of Binary Phase Diagrams (1978), General
Electric Corp.

/66/ G. Linker, Mat. Sci. and Engineering 69, 105 (1985).

/67/ O. Meyer, A. Azzam, Phys. Rev. Lett. 52, 1629 (1984).

/68/ A. Azzam and O. Meyer, Nucl. Instr. Meth. B12, 369 (1985).

/69/ J.M. Lombaard, G. Linker, O. Meyer, Journal of Less
Common Met. 96, 191 (1984).

/70/ A. Turos, O. Meyer and Hj. Matzke, Appl. Phys. Lett. 38,
910 (1981).

/71/ J.A. Borders and J.M. Poate, Phys. Rev. B. 13 (1976) 969.

/72/ S.A. Drentje and J. Ekster, Journal of Applied Phys.,
45 (1974) 8.

/73/ A. Azzam and O. Meyer, Nucl. Instr. and Meth. B 7/8 (1985)
113-118.

/74/ L.M. Howe, M.L. Swanson and A.F. Quenneritine, Nucl.
Instr. Meth. in Phys. Research 218 (1983) 663-668.

/75a/ R. Vianden, E.N. Kaufmann and J.W. Rodgers, Phys. Rev. B22
(1980) 63.

/75b/ D.K. Sood and G. Dearnaley, Rad. Eff. B9 (1978) 157.

/76/ Physical Metallurgy , Edited by R.W.Cahn and P.Hassen,
(1983), North Holland Physics Publ.

/77/ J.A. Borders and J.M. Poate, Appl. Phys. Lett. 25 (1974).

/78/ L.M. Howe and M.L. Swanson, in Point Defects and Defect
Interaction in Metals, eds., Ichi Takamuta et al.
(North Holland, Amsterdam) p. 53 + 364 (1982).

/79/ S.R. Reimtsema, E. Verbiest, J. Odeurs and H. Pattyn,
J. Phys. F. Metal. Phys. 9 (1979) 1511.

/80/ A.R. Miedema, Metallkunde 70 (1979) 345.

/81/ M. Doyama, Phys. Rev. 148 (1960) 681.

/82/   M. Doyama, Journal of Nucl. Mat. 69 + 70 (1978) 350-361.

/83/   A.R. Miedema, P.F. de Chatel and F.R. de Boer,
       Physica 100B (1980) 1-28.